

Populärvetenskaplig sammanfattning

Den centrala delen av detta examensarbetet har varit att undersöka möjligheten att detektera gas inuti lungorna hos för tidigt födda barn, prematurer, med hjälp av den laserbaserade och icke-inversiva tekniken GASMAS (GAs in Scattering Media Absorption Spectroscopy) .

Till prematurer räknas barn som är födda före 37:de graviditetsveckan. Då lungorna är det sista vitala organet som utvecklas under graviditeten kan en för tidig födsel leda till problem för funktionen av dessa. Detta examensarbete gick ut på att undersöka ifall GASMAS tekniken kan användas för att monitorera lungfunktionen för prematurer. De stora fördelarna med GASMAS är att icke-joniserande strålning används, att den är icke-inversiv och modiliteten av instrumentet. En korrekt behandling av de eventuella problemen kan vara skillnaden mellan liv och död och för det krävs en bra diagnos.

GASMAS är en teknik som mäter gas i spridande material, så som vävnad, med hjälp av laserljus i den nära infraröda regimen. Synligt ljus har våglängder på c:a 400 till 700 nm och det nära infraröda på 700 till 1000 nm. Vävnad sprider ljus mycket bra, vilket innebär att riktningarna hos de inkommande fotonerna ändras ofta och gör därmed ljuset diffust.

I application med att mäta gas i lungorna sänds ljuset in i vävnaden och där kommer det att studsa omkring tills det når gasen i lungan. Där kommer några fotoner att absorberas av gasen. Absorptionen sker p.g.a. att de inkommande fotonerna har en energi som korrelerar med den som behövs för att ändra strukturen hos den typ av molekyl som man önskar detektera. Alla olika molekyler har en unik uppbyggnad som gör att man kan välja vilken molekyl som ska undersökas bara genom att välja energi på det utsända ljuset. Energin eller våglängden hos ljuset, alltså färgen, är egentligen samma sak då våglängden beror på energin av ljuset. Högre energier ger kortare våglängder. Absorption sker även i vävnaden vilken är mycket tätare än gasen. I det nära infraröda området blir ljus som går igenom ett par cm vävnad förtunnat c:a tusen gånger medan absorptionen från syrgas genom en meter endast ger en förtunning på ett par procent. Detta innebär att absorptionen från gasen endast kommer vara en liten dipp i absorptionen från vävnaden. Detta ställer stora krav på mätteknikens noggrannhet vilka GASMAS instrumentet uppfyller. I instrumentet, som tidigare har används för att mäta gaser i bl.a. bihålorna, så mäts syrgas vid 760 nm och vattenånga mäts vid 935 nm. Som ljuskällor används två diodlasrar, liknande de som finns i laserpekare och CD/DVD läsare. Anledning till att mäta två gaser är att absorptionen som erhålls från vattenånga kan användas som referens för att beräkna koncentrationen av syrgasen. Detta är väsentligt vid monitoreringen av lungfunktionen. I detta examensarbete har det visats att GASMAS tekniken kan ge indikationer på hur gasfördelningen i lungorna på prematurer är. Det finns tre allvarliga åkommor som ger upphov till en inhomogen gasfördelning i lungorna till vilka GASMAS tekniken kan vara ett kraftfullt diagnostiskt vertyg.

För prematurer, födda runt 23:dje graviditetsveckan, kan det vara så att lungorna och deras arteriella träd inte är färdigtutvecklade. Obehandlat så leder detta till en kronisk minskning i lungkapaciten vilket slutligen kommer vara dödligt för barnet.

En åkomma som kan ställa till problem ända upp till fyra veckor innan normal graviditetstid är en brist på ett ämne kallat surfactant i lungorna. Surfactant ligger som ett lager på insidan av alveolerna, de små luftsäckarna där gasutbytet sker, och de mindre bronkerna, luftrören som transporterar gaserna genom lungorna. Här verkar surfactant som en fjäder som håller alveolerna och de mindre bronkerna utspända även då en utandning sker. En brist av detta ämne leder till att alveolerna och de små bronkerna kan kollapsa och växa ihop. På grund av kollapser och förträngningar kan stora delar av lungorna bli odugliga vilket leder till kronisk minskning i lungkapaciteten.

En annan åkomma som kan uppstå är att andningen hos barnet stannar upp vilket kan vara mycket farligt. Den återställs i många fall av sig själv men då detta inte sker är situationen mycket allvarlig.

Behandlingen för de ovan nämnda åkommorna är att man lägger ett övertryck i barnens lungor vilket håller lungorna uppspända och därefter behandlas de olika problemen. Om ett för högt övertryck är applicerat kan lungorna börja läcka och gassamlingar kan uppstå i lungsäcken vilket hämmar expansionen vid inandning. Även detta genererar en ojämn gaskoncentration som kan detekteras.

I detta arbete har det visats att gas kan mätas i modeller liknande, dels en prematur på ett kilo och dels ett fullt utvecklat barn på tre kilo, gjorda av en vildsvinslungor och gelatinbaserade vävnadsfantomer. Det har även visats att transmissionsmätningar, d.v.s. mätningar där detektorn och ljuskällan är på varsin sida av bålen är kraftigt begränsade p.g.a. bålens tjocklek. Reflektionsmätningar, d.v.s. mätningar där detektor och emittor är på samma sida bålen, har däremot goda potentialer att fungera i mätningar *in vivo*. Då vävnad sprider och absorberar olika vid olika våglängder så kommer vägen ljuset tar vara annorlunda för 760 än för 935 nm. Detta kan komplicera beräkningen av syrgaskoncentrationen. I transmissionsmätningar kommer detta inte ge någon stor effekt då huvuddelen av det detekterade ljuset går rakt igenom provet. I reflektionsmätningarna kommer det dock att påverka mer p.g.a. att 760 nm ljuset kommer nå djupare än 935 nm ljuset och därmed prova större mängder gas. Det har verifierats att de mätta gaserna kommer från inuti lungorna. Potentialen att mäta vattenånga vid 820 nm har också utretts och det har visats att det finns många fördelar med att i framtiden basera instrument på en laser vid denna våglängd.

Contents

1	Introduction	3
1.1	Background and motivation	3
1.2	Scope	5
1.3	Outline	5
1.4	Summarized results	6
2	Tunable diode laser absorption spectroscopy	7
2.1	Molecular structure	7
2.1.1	Electronic states	8
2.1.2	Vibrational states	9
2.1.3	Rotational states	10
2.2	Absorption spectroscopy	10
2.3	Molecular line selection	11
2.4	Diode lasers	13
2.4.1	Diode laser principles	13
2.4.2	Laser types	16
2.5	GASMAS	17
3	Light propagation in human tissue	20
3.1	Light propagation	20
3.2	Optical properties of selected tissue types	22
3.3	Time-resolved measurement	24
3.4	Monte Carlo simulations	26
4	Anatomy of the measurement areas of interest	28
4.1	Respiratory system	28
4.2	Surrounding tissue	30
5	GASMAS instrumentations	33
5.1	760/935 nm instrument	33
5.2	760/820 nm instrument	35
5.3	WMS signal generation and absorption signal extraction	36
5.3.1	WMS signal generation	36
5.3.2	Harmonic selection	37
5.3.3	Intensity normalization	39
5.3.4	WMS extraction	41
5.3.5	Absorption signal evaluation	41
5.4	Evaluation program	46

6	Measurement and simulations	48
6.1	Simulation on the benefits of a 820 nm laser	48
6.1.1	Introduction	48
6.1.2	Simulation of penetration depth	48
6.1.3	Experimental penetration depth	49
6.1.4	Discussion	49
6.2	Initial measurements on boar lung	50
6.2.1	Introduction	50
6.2.2	Transmission measurement	52
6.2.3	Transmission measurements with tissue phantoms	53
6.2.4	Reflection measurements with tissue phantom	56
6.2.5	Time-resolved measurements	58
6.2.6	Discussion	59
6.3	Aftermath of initial measurements on boar lung	60
6.3.1	Tissue phantom	60
6.3.2	Ratio difference in path length in reflection geometry	61
6.4	Measurements on nitrogen flushed boar lung	62
6.4.1	Introduction	62
6.4.2	Breathing simulation	63
6.4.3	Curved or flat geometry?	65
6.4.4	Verification measurements	66
6.4.5	Discussion	66
6.5	The pursuit of zero signal in measurements on boar lung	68
6.5.1	Introduction	68
6.5.2	Zero signal	68
6.5.3	Discussion	70
6.6	Measurement on human lung in vivo	71
7	Discussion	72
8	Summary and outlook	75
8.1	Summary	75
8.2	Outlook	75
9	Acknowledgments	77

Chapter 1

Introduction

1.1 Background and motivation

Much of the medical world changed when x-rays and other forms of novel radiation were discovered. Since then many more discoveries have been added to these. Some of them describe how x-rays and other forms of ionizing radiation may damage the body instead of helping it. This started the research and development of non-ionizing methods to replace the potential dangerous ones. Visible and near infrared light have very weak energy in comparison to x-ray radiation. Still the human eye is designed to detect precisely these energies and may be damaged if exposed excessively of it.

One of these new non-ionization methods is GASMAS (GAs in Scattering Media Absorption Spectroscopy). As the name indicates it is a technique to measure gas within a medium that scatters light. It is the absorption of the gas that is measured but contrary to other absorption spectroscopic methods diffuse light is used and thus the path length of the light is unknown. It is problematic to separate if the absorption comes from a high concentration of the gas or a long path length. However, the GASMAS technique solves the problem with the help of using two different radiation wavelengths.

Diode lasers have very nice modulation features and are powerful tools in spectroscopic applications where GASMAS is one. One might say that GASMAS is a subcategory of TDLAS (Tunable Diode Laser Absorption Spectroscopy). The GASMAS technique was first published in 2001 [1] and has developed over the years both in applications and in system effectiveness. The first clinical measurements were done on the sinuses with the purpose to diagnose sinusitis [2]. These were later extended to the studies on the mastoid bone behind the ear. It is not only cavities in the skull that are filled with gases in the human body but also e.g. the lungs.

The non-ionizing techniques used today to monitor the gases within lungs (often oxygen and carbon dioxide) is based on measuring the inhaled and exhaled gases. Only a summation of the entire lungs without specificity to individual parts is acquired. If one or two lobes are blocked by a tumor the air flow to these lobes is reduced or cut off. Current methods can indicate that something is wrong but cannot say where. The spatial information can, however, be acquired by letting the patient undergo an x-ray based imaging procedure and be exposed

by ionization radiation that might alter the DNA in the cells and cause tumor growth and cancer. X-ray imaging is based on the fact that x-rays interact with substances depending how heavy the atoms within it are. Bone that contains heavy elements such as calcium absorbs much of the x-rays creating a shadow behind it. Tissue that is based on carbon, or more light elements, absorb less and cast a lighter shadow. The concentration of the elements also makes an important difference which allows almost all x-rays to penetrate through gases. Hence, gases casts no shadow from x-ray radiation. X-rays can be a potential tool to study a lung and possible blockages but if one would like to study dynamic processes in the lung, such as oxygenation over time, the amount of x-ray radiation needed would be dangerous. For premature neonates the radiation clearly is even more hazardous. Actually, premature neonatal frequently have severe problems with their lungs and this is the motivation for the present study.

The mortality of premature neonates have during recent years decreased [3] but is still today significant [4]. Much of the mortality is due to problems with the lungs. The lungs are the last organ to fully develop due to the fact that the lung will not be needed until birth. Throughout the pregnancy the oxygen is provided by the mother through her blood. The further the child has developed during the pregnancy the more limited the problems are with the respiratory system. For the very prematurely born children the alveoli (the small gas spheres within the lung where the gas exchange occurs) are not fully developed. For neonates born as early as the 23rd week of pregnancy, both the lung and the pulmonary arterial tree can be underdeveloped, possibly resulting in a chronic decrease in lung capacity.

Another disorder that might cause problems even for children born as little as four weeks before the full time is surfactant deficiency. Surfactant is a substance that works as a spring for the alveoli and the small airways that keeps them distended even during an exhale facilitating gas exchange. A deficiency of the surfactant layer causes the alveoli to collapse resulting in an uneven distribution of gas within the lung. If untreated, this condition will lead to the alveoli and the small airways growing together in a collapsed way resulting in a chronic decrease in lung capacity. Entire lobes can be lost due to alveoli collapse and/or obstruction in a airway.

A third condition that might occur for premature neonates is Apnea, a condition where the breathing just stops. It can be very dangerous but can be observed through uneven gas distribution in the lung.

The primary treatment for these conditions is important for the survival of the children [5]. The treatment involves applying an overpressure to the lungs forcing them to a distended state. If a too high pressure is applied the lung might be overdistended and might even result in pneumothorax, an assembly of gas in the pleura. Uneven gas distribution is very common and is present for almost all premature neonates. By studying the gas distribution the GASMAS technique might be a powerful monitoring and diagnostic tool. A method to monitor the volume of the lung used today is based on measuring the impedance [6]. However, this technique cannot give the information that the GASMAS technique can yield and the electrodes used in measuring the impedance can cause damage on the child's fragile skin.

The attenuation of light in tissue is a the most prominent limitation for the GASMAS technique in clinical applications. Hence, the pursuit of a solution to the attenuation is essential. Today the measurements on water vapour are done

with a laser at 935 nm but at this wavelength water absorbs quite much and thus a lower wavelength might gain additional penetration depth. Some nice water vapour absorption lines have been found at 820 nm but to evaluate if the gain from the change is worth the trouble, measurements and simulations must be done.

1.2 Scope

The scope of this work was primarily to investigate the feasibility to study gas within lungs of neonatal babies. A laboratory model was built allowing preliminary measurements. The possible benefits and disadvantages with an instrument using water vapour detection at 820 nm instead of the current 935 nm was also studied. Initial proof of principle measurements needed to be done and also some that verify that what is measured really is understood. Four different measurements series have been done where the first one was a study of the possible penetration depth for different wavelengths. The second one was the proof of principle measurements where the possibility to measure gases within the lungs of neonates was studied. In the third dynamic processes was studied such as breathing, and in the fourth and final one verification that the measured absorption originate from the gas within the lung. The primary model should represent a premature neonatal because the possibility for the GASMAS technique at its current stage to contribute to the treatment of disorders here have the largest potential. Hence, sizes and optical properties of the different tissue types need to be investigated for a varying selection of neonates.

1.3 Outline

The report is split up into seven chapters, tunable diode laser absorption spectroscopy (TDLAS), light propagation in human tissue, anatomy of the areas of interest, GASMAS instrumentation, measurements and simulations, discussion and summary and outlook. Initially the most essential parts of the underlying theory for TDLAS is presented. Here issues like molecular structures and diode lasers are described. The GASMAS method is also presented. In the "light propagation in human tissue" chapter the light propagation in tissue is described together with optical properties of different tissue types. In the anatomy chapter the respiratory system and information regarding tissues surrounding the lung are described. The instrument and the evaluation method used for this work is presented in the instrumentation chapter where also an overview of a potential new instrument is presented. The performed four different measurements are presented in "Measurements and simulations". A discussion about the whole work in general is then presented and finally the summary and outlook. In the Appendix A an example of an evaluation code is presented. A report from a project where some of the aspects of the geometry of a lung are studied with Monte Carlo simulation, time of flight measurements and GASMAS measurements is also in the Appendix. An alternative way of creating a phantom for the lung is also presented in the report.

1.4 Summarized results

During the work it has been shown that gas absorption signals from oxygen and water vapour can be obtained in laboratory models that are similar to both premature neonates but also fully grown neonates i.e., both to premature children that weigh about 1 kg and to fully developed children of about 3 kg. The task is obviously easier for the premature children because they are smaller in size. Fortunately these are the ones which might need the benefits that GASMAS can provide the most. The measurements have also shown that transmission measurements are probably too hard to do if the child is not very small. Reflection measurements are the way to go in the future. It has also been shown that the gas absorption only comes from within the sample volume and no, or a very small, offset is present for the instrument. The instrument has been tried on adults and a 2.5 years old child and no gas absorption could be observed, as might be expected.

Simulations and measurements have indicated that a new instrument that detects water vapour at 820 nm instead of 935 nm might have a deeper penetration depth and might make it possible to do measurements on bigger children. The oxygen wavelength is however the same but a better fibre solution can be provided and that might increase the output effect.

Chapter 2

Tunable diode laser absorption spectroscopy

In this chapter the foundations of TDLAS (Tunable Diode Laser Absorption Spectroscopy) will be presented. Initially the energy structure of a molecule will be discussed followed by a part on absorption spectroscopy. Then a discussion regarding the selection of which transition in the oxygen and water vapour should be chosen. The optical sources, diode lasers, are then presented. Finally the TDLAS-based method GASMAS, which is an essential part of this project, is described.

2.1 Molecular structure

From basic atomic physics we know that different atoms absorb and emit photons depending on their electron structure. Most materials in nature are not built of just a single atomic species but of a combination of many different atoms i.e. molecules. These are created because the total energy is lower when the atoms are together than separated. In a molecule the atoms interact with each other creating a more complex energy structure than that of a single atom. The atoms can affect electrons of other atoms, and electrons can be shared by many atoms. The motion of the atoms with respect to each other also affects the energy structure. They can either vibrate, i.e., oscillate back and forth and/or rotate. In molecules with only two atoms these motions can really be understood but for molecules with three or more atoms the possible motion patterns get very complex.

To simplify the problem the assumption that the nuclei are fixed is made. The nuclei are much heavier than the electrons and therefore move many times slower. This is the foundation of the *Born-Oppenheimer approximation* which states that the total energy of the molecule is the sum of the electronic energy, the vibrational energy and the rotational energy [7]; see Fig. 2.1. In reality the rotation is affected by the vibration of a molecule due to the changes in moment of inertia [8].

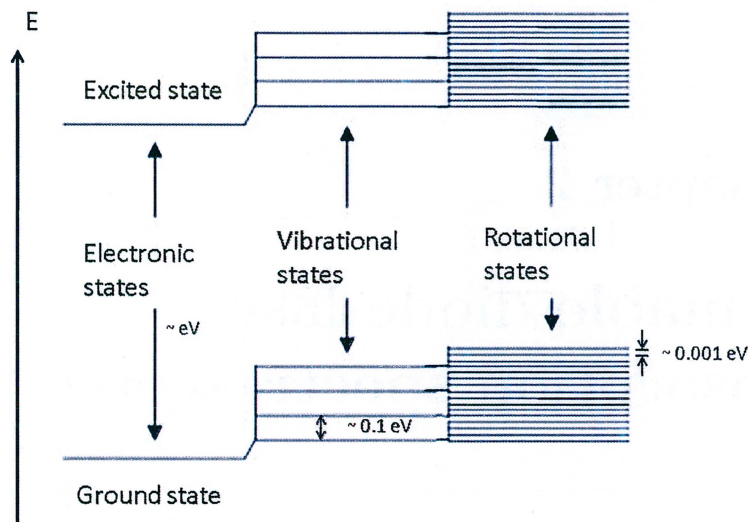


Figure 2.1: *Molecular energy level diagram with electronic, vibrational and rotational states. The energy difference between two electronic states is a few eV, two vibrational states a few 0.1 eV and two rotational states a few 0.001 eV.*

2.1.1 Electronic states

To describe an atom in a mathematical way one uses the fact that the atom has a centre (the nucleus) where the electrons move around. By assuming that each electron moves independently of the others in a field created by the nucleus and the remaining electrons, simplifications can be done. From basic atomic physics we know that the next step in the calculations for atoms is the central field approximation and then many different kinds of perturbations follow. To get the energies of the levels the Schrödinger equation is then solved. Molecules in general do not have a central symmetric structure which makes the description of it more complex. There are a few special cases which have a symmetric structure which makes them easier to describe. Diatomic molecules (molecules with two atoms) have a cylindrical symmetry and homo-nuclear molecules with atoms of the same kind, have a central symmetry. For an electron in motion in an atom the total angular momentum is constant due to the central field symmetry but this is not the case in most molecules, except homonuclear molecules. Therefore the coupling between angular momenta is different in molecules than in atoms. By placing the axis of symmetry through the two nuclei in a diatomic molecule, the projection of the electrons orbital angular momentum will be constant regardless of motion. The total angular momentum will then precess around the symmetry axel and the different projections can be described by quantum numbers. The different possible projection give rise to different energies.

2.1.2 Vibrational states

The binding energy between two nuclei can be described by a potential, called the *Morse potential*. The potential is different for every electronic states. In the potential the other atom can vibrate back and forth and depending on the vibrational energy at different energy levels; see Fig. 2.2. More energy gives a vibration in a higher state, i.e a higher energy level, which corresponds to a larger vibration amplitude. For lower states the harmonic oscillator can be used to describe the placement of the energy level resulting in a set of equidistant states; see Fig. 2.2. The *Morse potential* can be described by an exponential function and if this is Taylor expanded, a series of polynomial terms is acquired. The first term can describe the harmonic oscillator and by adding more terms the expression becomes more and more like reality. This explains a way the harmonic oscillator can be used as a simplification of the true potential. The lowest vibrational state is not situated in the bottom of the potential, since here both the energy and the position are known which is a direct violation of nature in accordance with the *Heisenbergs uncertainty principle*. By exciting the molecule the vibration will be fiercer and if exciting it too much the oscillating atom will be excited out of the potential and the molecule is torn apart.

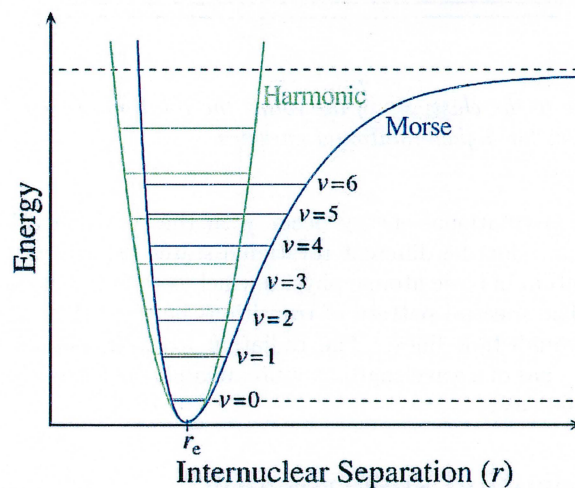


Figure 2.2: *Morse potential with vibrational states in it. For low vibration energies the harmonic oscillator can be used for an approximation.*

Transitions between vibrational states occur with the selection rule $\Delta v = \pm 1$, where $v=0,1,2,3,\dots$ for the different vibrational states. The selection rule is due to the harmonic oscillator structure and when the potential deviates from the harmonic, transitions with $\Delta v = \pm 2$, $\Delta v = \pm 3$ and higher can occur. These transitions are generally weak. Because of the equidistant states in the harmonic oscillator, transitions in the lower states have the same spectral line. The distance between two vibrational state is about 0.1 eV which represent approximately a wavelength of 10 μm . Because of the symmetry in homonuclear molecules, vibrational electric-dipole transitions do not occur but quadrupole and pressure induced transition might give rise to a weak spectral line.

2.1.3 Rotational states

One can describe two atoms rotating around a centre of gravity with classical mechanics. In such a picture the rotational energy is proportional to the angular momentum squared divided by the moment of inertia. According to quantum mechanics the angular momentum is quantized and therefore also the rotational energy. In these expressions we have considered a rigid rotation while in reality rotation is more elastic. The system is affected with increasing moment of inertia for higher rotational energies and thereby decreasing the energy; see Fig. 2.3.

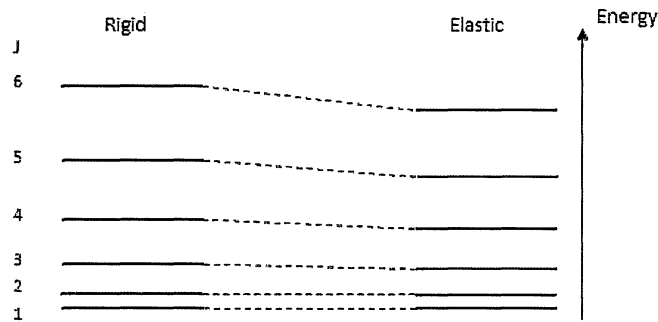


Figure 2.3: *Due to the elasticity of the rotor, the rotation energy decreases in an exceeding fashion for higher rotational energies.*

Alterations in rotational energy occur with the selection rule $\Delta J = \pm 1$, where $J=0,1,2,3,\dots$ for the different rotational states (Should not be confused with the J quantum in basic atomic physics which is the total electronic angular momentum). The spectral pattern of transitions between the rotational states is a series of equidistant lines. The radiation for a transition between two rotational states has a wavelength of approximately $1000 \mu\text{m}$ which represents an energy of 0.001 eV .

2.2 Absorption spectroscopy

The combination of the above described transitions creates a spectral finger print that is unique for each molecule. In absorption spectroscopy the attenuation of light is studied. If the energy of a photon corresponds to the energy of a transition the photon has probability to be absorbed. The strength of the absorption is proportional to how probable the transition is. The absorption can be described by the Beer-Lambert law; see Eq. 2.1.

$$I = I_0 \cdot e^{-\mu l} \quad (2.1)$$

Where I is the transmitted intensity, I_0 is the intensity from the source, μ is the attenuation constant and describes the probability for an attenuation event to occur. l is the propagation length.

The attenuation does not only need to depend on absorption but may also be due to scattering. In tissue, both scattering and absorption are important

even if scattering occurs much more frequently than absorption. A combined attenuation coefficient is defined, called the transport coefficient, μ_{tr} , and it is the sum of the absorption and the scattering coefficient; see Eq. 2.2.

$$\mu_{tr} = \mu_a + \mu_s \quad (2.2)$$

One must remember that scattered light is not "lost" but might be redirected again to contribute to the transmitted light. Absorbed light on the other hand is very rarely reemitted again. Thus when following one photon or looking at the total it is the absorption that matters.

2.3 Molecular line selection

When choosing which spectral line for the interrogated gas to be scanned by the laser, one must take a few things into consideration. First, the surrounding substances should not absorb in the same spectral region. Second, the detected absorption might not come from the interrogated gas or the signal through the spatial area might not be sufficient due to the absorption from the substances within. Because of the wide and dull absorption profile from liquids and solids the absorption from these can be removed; and not interfere with the detected absorption profile of the interrogated gas. However, the absorption from liquids and solids still attenuates the propagated light. The absorption from other gases are also spectrally narrow and cannot be removed in the same way as the absorption from liquids and solids. These do not attenuate the light in the same extent. However, the probability that another gas is sufficiently represented in both the spatial and spectral region as the interrogated gas is fairly small.

Another thing to take into consideration is the strength of the transition in the molecules that is being interrogated. It must be sufficiently strong to generate a detectable absorption in the limited path length the light will propagate within the gas.

The two above mentioned properties must be considered especially for water vapour. Water and water vapour absorb in similar spectral ranges. This is a problem when measuring water vapour in tissue because a great deal of water is bound within tissue. One will have to balance between having a strong absorption from the gas and a strong attenuation of the light from the tissue or having a weaker absorption and having a greater penetration depth.

A third thing to consider is the availability of light source on the market. "Can a laser be constructed at the desired wavelength with sufficient output power?" is a question one must ask oneself.

With the above mentioned properties one spectral region was chosen for molecular oxygen and two for water vapour. The oxygen is monitored at 760 nm and the spectral lines in the selected area comes from the A-band in oxygen; see Fig. 2.4. These lines come from different rotational states in the lowest vibrational states in the transition between two electron states.

The wavelengths chosen for water vapour is at 935 nm and 820 nm, where the first has a stronger absorption both from the surrounding tissue and the water vapour as can be expected when looking at Fig. 3.2 in Sect. 3.1. As discussed in Sect. 2.1 molecules that are not homonuclear or have other symmetries have a complex energy state structure. The water molecule has three vibrational quantum numbers and three rotational quantum numbers that each describe

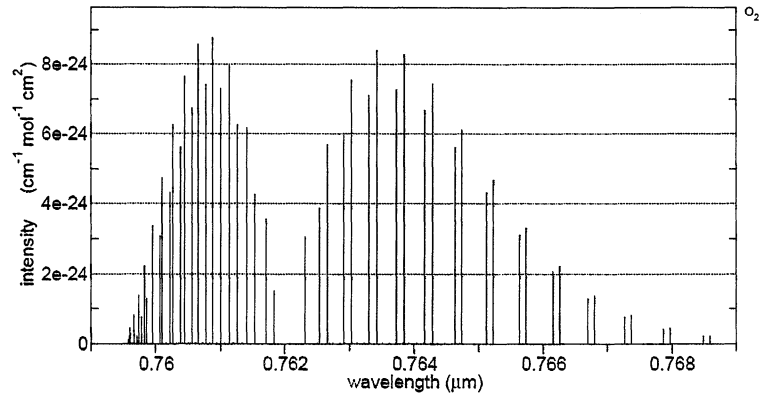


Figure 2.4: *The A-band in the spectrum from oxygen [9].*

a different type of vibration or rotation. The characterization of the water molecule is that it is a non-linear triatomic molecule and an asymmetric rotor. The vibrational and rotational states are described in a certain way due to these properties; the interested reader is referred to articles regarding HITRAN, e.g. [9]. The seemingly chaotic distribution of spectral lines for water vapour makes it hard to describe a set of spectral lines. Hence, only the most interesting and most used line will be presented for the two different spectral areas. In the 820 nm spectral area it is the line at 819.152 nm which correspond to the transition between the first excited electron state to the ground state and from vibrational state $\mathbf{v} = (2, 1, 1)$ to the lowest vibrational state $\mathbf{v} = (0, 0, 0)$ and from rotational state $\mathbf{J} = (3, 1, 3)$ to $\mathbf{J} = (2, 1, 2)$; see Fig. 2.5. The other strong transitions in the spectral area comes from the same electronic and vibrational transition but with a different rotational energy. The chosen line at 935 nm

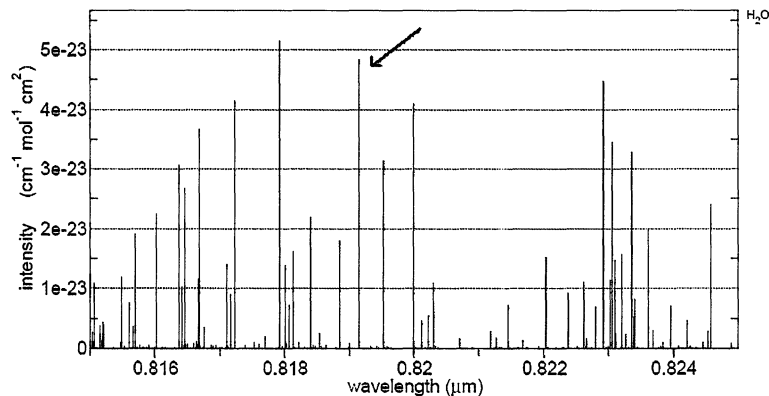


Figure 2.5: *The spectrum from water vapour at 820 nm. The most interesting and for me useful line is marked[9].*

is the one at 935.686 nm. The line correspond to the transition between the first excited electron state and the ground state and from the vibrational state $\mathbf{v} = (2, 0, 1)$ to the lowest vibrational state $\mathbf{v} = (0, 0, 0)$ and from rotational state $\mathbf{J} = (4, 0, 4)$ to $\mathbf{J} = (3, 0, 3)$; see Fig. 2.6. The other strong transitions in the spectral region comes from the same electronic and vibrational transition but with a different rotational.

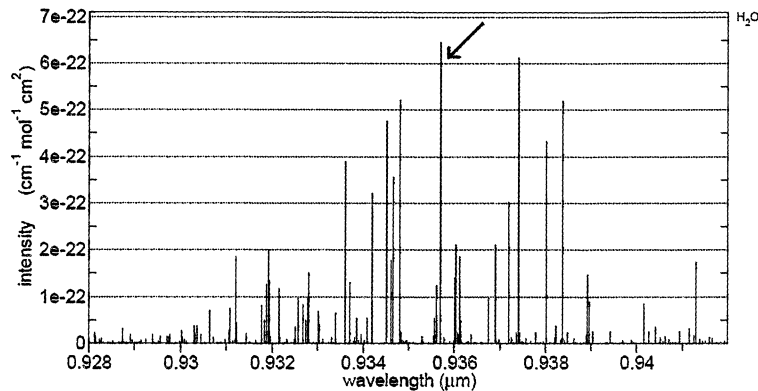


Figure 2.6: The spectrum from water vapour at 935 nm. The most interesting and for me useful line is marked [9].

2.4 Diode lasers

Diode lasers are powerful tools to interrogate and tune over selected absorption lines. A more common name for diode lasers are semiconductor laser. The properties of a diode laser make it very practical in many applications, not only in absorption spectroscopy. The ability to easily tune the lasing wavelength and the fact that its very capable for wavelength modulation, are some of the benefits [10]. The applications for diode lasers are constantly increasing. New lasers with better properties, like output power, expand the possibilities even more. The most well known application of diode lasers is the reading and writing of CDs and DVDs (in players and burners). The laser diodes in CD players have a wavelength of 780 nm and a power of a few mW. For CD writers more power is needed to do the burning so these have about a power of 40 - 50 mW. For DVD players/writers a shorter wavelength is used (635 nm or 650 nm) due to denser storage distribution on the disc. In general it is said that the resolving power of the light is half it is wavelength. Printers and optical fibre communication are other well know applications. Lasers in fibre communication have a wavelength of 1.33 μm or 1.5 μm .

2.4.1 Diode laser principles

The above mentioned properties can be explained by solid state physics. A semiconductor is a material with a band structure in its energy diagram where

the highest filled band is called the valence band and the band above that is called the conductive band. The energy difference between these two bands is called the bandgap.

To achieve lasing one must create population inversion in a medium. A population inversion is acquired when the population of a higher energy state is greater than that of a lower energy state. If then light with an energy that fits the energy difference between the two states is shone through the medium the light will be amplified. Stimulated emission and absorption (see Fig. 2.7) have the same probability to occur. With a higher population in the higher state, stimulated emission will dominate.

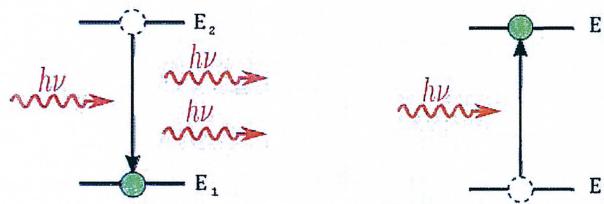


Figure 2.7: Stimulated emission amplifies the incoming light while stimulated absorption attenuates it.

In a diode laser the lasing medium is usually a p-n junction, i.e. the part where the amplification of the light is done is in the junction between a p-doped and a n-doped semiconductor made from the same host material. A p-doped material has an excess of holes (vacancies of electrons) in the valence band while the n-doped has an excess of electrons in the conductive band. A potential difference is created in the junction between the different materials. If no outer factors disturbs the junction, the Fermi energy will be the same on both the p-doped and the n-doped side; see Fig. 2.8. The Fermi energy is the energy for the electron with the highest energy.

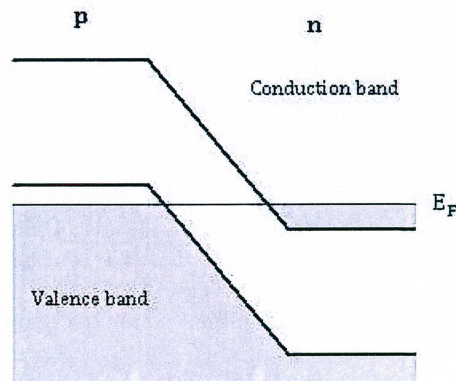


Figure 2.8: A potential difference is created in the junction between the p-doped and the n-doped material due to created charge differences.

By applying a voltage over the junction, with the positive charge on the n-doped side and the negative on the p-doped side, the potential difference can be altered. If the potential difference becomes so small that the electrons in the conductive band of the n-doped material and the holes in the valence band of the p-doped can meander over the junction, transitions between them can occur. In other words, a population inversion in the junction area has been created and light amplification can be preformed. When the voltage over the junction is applied, the Fermi energy for both materials is displaced. The distance between the two Fermi energies is a product of the voltage over the junction and the elemental charge. It is at this energy the lasing will occur when the energy is about the size of the bandgap, see Fig. 2.9. The bandgap energy depends on

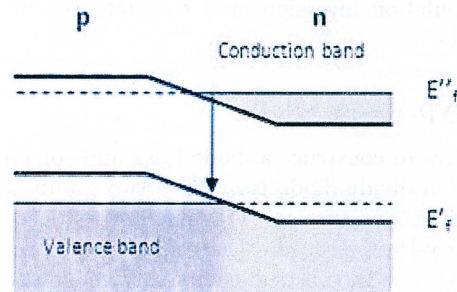


Figure 2.9: *By applying a voltage over the junction the potential difference changes and electrons and holes can occupy states further in of the junction. When the voltage has changed the potential so that the differences between of the Fermi energies on the p-doped and the n-doped side is approximately the size of the bandgap population inversion is created in the junction.*

which host crystal is used in the laser. Therefore diode lasers can have a wide spectrum of wavelengths down from the infrared region to the violet.

To achieve lasing one must have constructive interference in the cavity where light oscillates back and forth. Many different wavelengths may fit to achieve constructive interference and these are called cavity modes. The amplification of the light can only happen on a gain specified wavelength interval so lasing can only happen for a certain number of cavity modes. When lasing occurs on only one mode (one wavelength), the laser is called a single-mode laser; otherwise it is called a multi-mode laser. The wavelength difference between two modes is inversely dependant on the length of the cavity and is described by Eq. 2.3.

$$\Delta\lambda = \frac{\lambda^2}{2d} \quad (2.3)$$

Here $\Delta\lambda$ is the wavelength separation between the modes, λ is the wavelength and d is the cavity length. In a diode laser the cavity is constructed by polishing the sides of the semiconductor crystal. Due to the small size of the crystal, few micrometers, the distance between two modes is relatively long. Hence, diode lasers often are single-mode lasers.

The tuning of a diode lasers is done by altering the temperature and the current through the pn-junction. When temperature is altered, the Fermi energy is changed; hence the probability for electrons being at higher energies is dependant of the temperature. Only the electrons in the conductive band and holes in the valence band will be effected due to the thermal energy being small in comparison to the bandgap. The thermal energy at room temperature (300 °K) is about one to two magnitudes smaller than a typical bandgap. For diode lasers with longer wavelengths in the IR-region this may be a problem to take into consideration due to the small bandgap. The temperature also alters the volume of the crystal and therefore the cavity length, which effects the cavity's mode structure. The temperature can also be altered by changing the current through the junction. The current also effects the intensity of the laser because when the current is tuned the amount of electrons and holes are altered in the junction. The population inversion, and therefore the intensity, is increased with higher currents.

2.4.2 Laser types

There are many ways to construct a diode laser and some of them will be discussed here. One can divide diode lasers into two groups with different lasing orientations, horizontal and vertical [11]. The horizontal ones that will be discussed are the Fabry-Prot structure (FP) and distributed feedback structure (DFB) and the vertical is the vertical-cavity surface-emitting laser (VCSEL).

FP

In the Fabry-Prot structure the optical reflection (feedback) is done by the borders of the crystal; see Fig. 2.10. The difference in refractive index between air and the crystal is sufficient to get enough reflectance off the end surfaces of the crystal to create a resonator. The reflection coefficient is approximately 30 %. By adding an additional coating on end surfaces the reflection can be tailored to anything between antireflection and perfect reflection.

DFB

The DFB diode laser is similar to the FP but with the difference that the reflection of the light is extended over the hole resonator instead of only the end surfaces. By altering material with different refractive index in the layer in contact with the amplification layer an alteration of refractive index is created in the amplification layer; see Fig. 2.10. Light is reflected in the junctions between areas with different reflective index in the amplifications layer. For a specific wavelength the reflected light waves will interfere constructively and a high reflection coefficient is obtained. The specific wavelength is called the Bragg wavelength. This kind of altering reflection structure is called distributed Bragg reflector (DBR).

VCSEL

The structure of a VCSEL is more or less similar to that of a DFB but the lasing occurs perpendicular to the amplification layer. The cavity is built of two DBR structures above and below the amplification layer. Here the DBR:s

are constructed with many layers of altering material; see Fig. 2.10. Since the amplification occurs in a very thin part of the cavity the DBR:s must have a very high reflection coefficient to reach the lasing threshold.

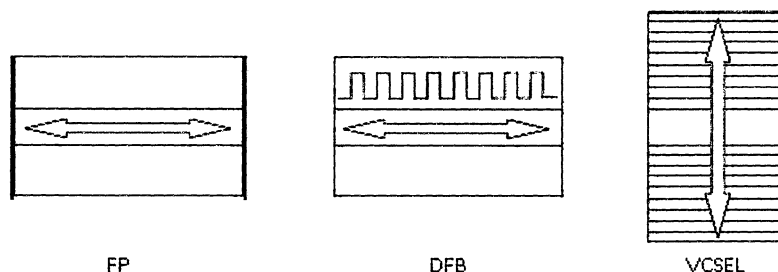


Figure 2.10: *Three different ways to construct the laser cavity in a diode laser. The Farby-Prot structure to the left, the distributed feedback structure in the middle and the vertical-cavity surface-emitting structure to the right. The arrows represent the lasing orientation.*

The advantages of the DFB compared with the VCSEL is that the output power from the DFB is much higher due to the larger amplification area. The VCSEL is easier to build and thereby becomes cheaper to buy. The tunability of the VCSEL is also wider. The DBR structure in the VCSEL is more sensitive to temperature changes than the one in the DFB.

There are many more specifications of a diode laser which are not treated here. For example the amplification layer can be constructed in many ways such as a homostructures, single- and double-sided hetrostructure. It can also be of quantum well or multiple quantum well structure. The laser beam in the diode can either be gain guided or index guided. In some cases an external cavity can be used and there are a couple of different varieties of these. As mentioned in Sect. 2.4.1 the diode can also be of many different semiconductor materials. For the interested reader reference [11] is recommended.

2.5 GASMAS

GAs in Scattering Media Absorption Spectroscopy, or in short GASMAS, is a method to study the absorption from gas within scattering media. The foundation of the method is that free gas exhibits a sharp and distinct absorption spectrum while solid media have a slower and duller absorption spectra. The spectral structures for gases are about ten thousands times sharper than those from solids. The latter are frequently also more prominent which results in that the absorption from gases within scattering solids is only a small dip on the more pronounced absorption from the solid.

One might say that GASMAS is a submethod of TDLAS because it uses diode lasers which are scanned over absorption lines for the target gases. Because of the weak absorption signal, a method called Wavelength Modulation Spectroscopy (WMS) is used to extract the signal. By implementing the WMS technique to absorption spectroscopy methods the impact of the $1/f$ noise is

reduced and the sensitivity is increased.

GASMAS differs from ordinary absorption spectroscopy by the fact that diffuse light is studied and thus the path length and the path are unknown. To know if the absorption comes from either a high concentration of the gas or a long path length one must know either one. The path length within a turbid medium is not possible to determine by only doing GASMAS measurements with one interrogation gas. The concentration of a gas can in some cases be assumed or known. The concentration of water vapour within tissue can be considered to be known by the fact that the relative humidity is 100 percent. The concentration of water vapour is directly dependent on the temperature and the relative humidity. A parameter that represents the absorption is proportional to the product of the concentration of the gas and the path length. The parameter is called equivalent length and it refers to the absorption from the gas within the turbid media to a path length in ambient air that yields the same absorption. If only the presence of gas is of interest the value of the equivalent length is sufficient but if the concentration of the gas is of interest further efforts must be made.

The GASMAS method is a relatively new technique and it was developed at the Atomic Physics Division with the first paper [1] published in 2001. Here absorption from oxygen within a couple of different media e.g. apples, wood and polystyrene foam was studied. In Sjöholm et al. [1] the laser light was guided by a multi-mode fibre and the signal was detected by a PMT (PhotoMultiplier Tube). The signal was extracted by usage of the standard addition method.

To be able to determine the concentration of the trapped gas the GASMAS measurements can be combined with TOF, time of flight, measurements with the purpose to identify the path length. This approach was presented by Somesfalean et al. [12] in 2002.

The approach from Sjöholm et al. was used to do further and deeper studies on fruits [13] and wood [14]. So far the measurements had been done in transmission geometry but in 2005 the first measurements in reflection geometry was performed by Persson et al. [15].

Dynamic processes have also been studied with the GASMAS technique. In some previously mentioned work nitrogen gas has been used to pre-load the sample to study the subsequent diffusion of the gases through the sample, and in 2006 the drying process of wood was studied by Andersson et al. [16].

The first clinical application of GASMAS was to study the oxygen within the frontal sinuses and it was done by Persson et al. [2] in 2006. In combination with the prospect of measuring gas *in vivo* a new approach was developed in order to solve the problem with the unknown path length [17]. The approach was based on simultaneous measurements of two gases and it is still used in today's instrument. Different gases absorb at different wavelengths and thus two lasers must be used. Assuming that the path length of the light is the same or separated by a "magic ratio" the problem with the unknown pathlength can be solved and the concentration can be calculated if the concentration of the reference gas is known. Additional work has been done with measurements on human sinuses, both *in vivo* [18, 19] and with Monte Carlo simulations [20].

Parallel to the work on the sinuses work has been done on pharmaceutical tablets by Svensson et al. [21, 22] with the main purpose to determine the porosity. A fibre-based system and a system with a direct output of a VCSEL diode laser were used to study the porosity. Not only the applications for GASMAS

have developed over the years but also the equipment used. In 2007, the analog lock-in amplifier, used before was replaced with a DAQ, data acquisition card and thus increasing the mobility and reducing the size of the system [23]. This also made the signal processing more flexible because all the acquisition data is digital. Work has also been done to decrease the influence of interferences [24].

Today the GASMAS technique is used in a variety of applications. These can be divided into five groups; medical, pharmaceutical, packaging, optical porosimetry and effects on confined molecules within nanoporous materials. In the medical field a clinical study has been made by Lewander et al. [25] on the human sinuses with 40 patients participating. The study and characterization of pharmaceutical tablets continue. Applications in the packaging area have been both on packages containing liquids in order to verify the quality of the liquid, e.g. juice [26] and on apples to monitor how a sugar solution penetrates within the apple in order to extend the apples lifetime. Porosimetry today is usually done by studying the penetration of mercury at different pressures which is a time consuming and complicated process. Hence, the development of an optical technique is of interest in order to simplify the measurement. The absorption profile from gas within a cavity is usually broadened by the Doppler effects and also by collisions with other molecules and with the walls of the cavities. The effect from wall collisions is very small in comparison when the cavity is large. However, when the cavity is in the size of nanometers the interaction between the wall and the gas molecule increases and might be observed on the line profile of the absorption.

Chapter 3

Light propagation in human tissue

In this chapter the propagation of light within tissue will be discussed together with two methods to study the propagation. Initially, issues concerning the propagation of light are discussed followed by optical properties of selected tissue types. At the end the two methods, time of flight measurements and Monte Carlo simulations, will be presented.

3.1 Light propagation

Human tissue is a very good example of a scattering material. It can easily be observed by placing a white light source behind a finger. The finger will shine in a reddish color but the shadow of the bone will not be present. A strongly scattering material may be identified by the fact that it scatters at least two magnitudes more than it absorbs. The scattering is dependant on the wavelength of the propagating light. The scattering process within tissue is seemingly random but it is due to spatially varying tissue density, refractive index and dielectric constants. The biological tissue particles are usually larger than or the same size as the wavelength of the visible and the near infrared, NIR, and thus the governing scattering type is Mie scattering [8]. The scattering particles in tissue are the structures within the cells, such as the nucleus and other organelles.

The other type of scattering is Rayleigh scattering and describes the scattering phenomenon when the scattering particles are considerably smaller than the wavelength of the light. Rayleigh scattering is important in the atmosphere and explains why the sky is blue. On the other hand, the white appearance of the clouds is due to Mie scattering.

An effect from the fact that it is Mie scattering that governs the scattering phenomena in tissue is that the scattering profile is not isotropic but elongated in the direction in which the incoming photon is propagating. The anisotropic scattering profile is described by the anisotropy factor g , defined as the expectation value of cosine θ ; see Eq. 3.1.

$$g = \langle \cos(\theta) \rangle, \quad (3.1)$$

where θ is the scattering angle. The scattering in human tissue is very anisotropic and the g factor is about 0.8 - 0.9; see Fig. 3.1. Another reason to the introduction of the g factor is to simplify the otherwise seemingly random scattering. The simplification is done by saying that all scattering events occur with the angle θ . The average scattering occurs with the angle that correspond to a certain g value and because there are many scattering events occurring the total scattering effect corresponds to a set scattering angle.

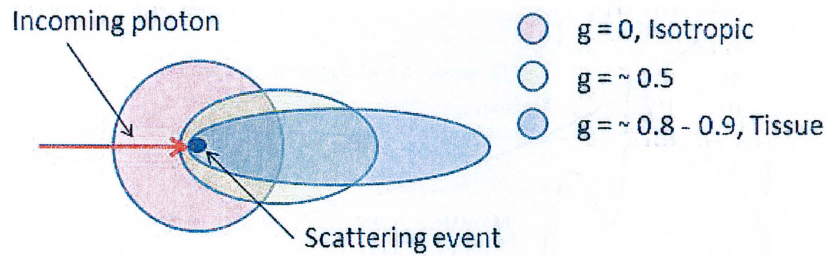


Figure 3.1: The scattering distribution for different values of the anisotropy factor g . g for human tissue is about 0.8 - 0.9.

The scattering coefficient, μ_s , has the dimension of m^{-1} and describes the probability of a scattering event to occur during a certain propagation distance. However, due to the highly scattering nature of tissue the value is often written in mm^{-1} or cm^{-1} . The probability that a scattering event occurs during a infinitesimal distance ds is $\mu_s ds$. The scattering coefficient can be altered in order to describe the scattering in an isotropic way. This is important for many simulation techniques e.g. in diffusion theory where only isotropic propagation can be described [27]. The altered scattering coefficient is called reduced scattering coefficient and can be calculated using the anisotropic factor; see Eq. 3.2.

$$\mu'_s = \mu_s(1 - g), \quad (3.2)$$

where μ'_s is the reduced scattering coefficient.

If one were to illuminate a finger with, e.g. a green light source then the finger would not shine at all. This is due to the absorption by the tissue within the finger. Tissue components that absorb light are called chromophores. The main chromophores for visible light are hemoglobin and melanin. The latter is present in the eye and the skin. The absorption from melanin decreases with increasing wavelength. Hemoglobin absorbs differently depending on if it carries oxygen or not. When measuring the oxygenation of blood *in vivo* with a pulse oximeter, two sources with different wavelengths are used. One is chosen where the absorption difference between oxy-hemoglobin and hemoglobin is apparent and the other one where it is the same. The absorption from hemoglobin is of the same magnitude as melanin for wavelengths below approximately 600 nm but after that it falls off rapidly. In the near infrared (NIR) water is the main chromophore but it also affects the upper part of the visible region. The vast amount of water bound within the tissue and the blood makes it as important as the other two chromophores. The absorption from water gradually increases with wavelength above 800 nm. Water makes it almost impossible for light in

the IR region to penetrate more than at most a few mm of tissue. The interval between 600 nm and about 1300 nm is a region where the chromophores do not absorb as strongly. This is called the tissue optical window or the therapeutic and diagnostic window; see Fig. 3.2.

The absorption coefficient, μ_a is defined in the same way as the scattering coefficient but describing the probability for absorption, not scattering.

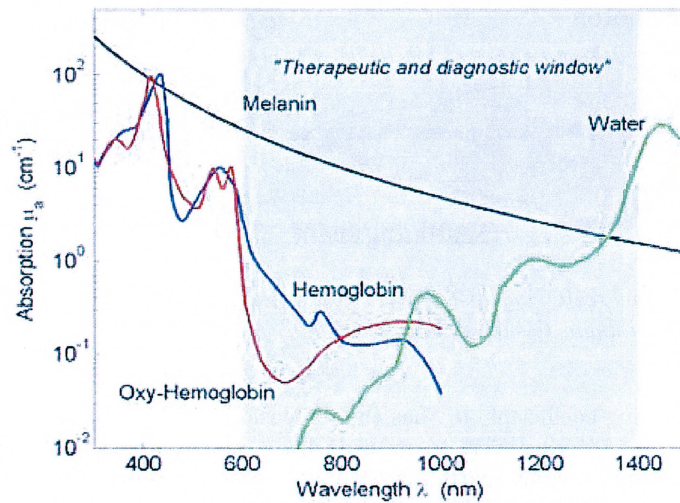


Figure 3.2: The interval between 600 nm and about 1300 nm is a region where the chromophores do not absorb as strongly. This is called the tissue optical window or the therapeutic and diagnostic window. The figure is from [28].

3.2 Optical properties of selected tissue types

Different compositions of the chromophores within different tissue types create different absorption and scattering coefficients. Hence, one cannot say that tissue in general has certain optical properties but must instead identify the optical properties for each of the tissue types that are of interest. For example, muscles are filled with hemoglobin and water while the skin has not that much water but melanin instead. Because of the difference in constituents the optical properties between the tissue types mentioned will be different. The geometry of the tissue also affects the absorption and scattering coefficients, not the tissue in itself but the total absorption and scattering of a piece of tissue. Solid material, such as tissue, is denser than gas and thus the amount of particles the light can be absorbed and scattered by is much fewer in gas. This creates "shortcuts" for the light to propagate through a geometry with many small gas cavities in an undisturbed fashion, which in turn alters the effective absorption and scattering properties; see Fig. 3.3. An organ with many small gas cavities is the lung but there are also air cavities in the skull.

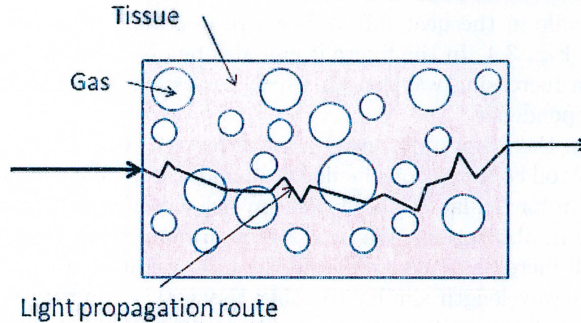


Figure 3.3: The light can take "shortcuts" through the tissue by propagate through gas bubbles. This alters the effective absorption and scattering coefficient.

The diversity of optical properties for different tissue types makes it hard to predict the optical properties of a certain tissue type. In this work a few assumptions and simplifications have been made to be able to use already measured data. Muscles and bones have been assumed to have the same optical properties as the abdominal muscles and the skull respectively. The tissue outside the muscles is simplified to only consist of the skin. The skin consists of many layers of different tissue types like epidermis, dermis, hypodermis and other layers but is simplified in this work to only one layer. The skin type is assumed to be Caucasian.

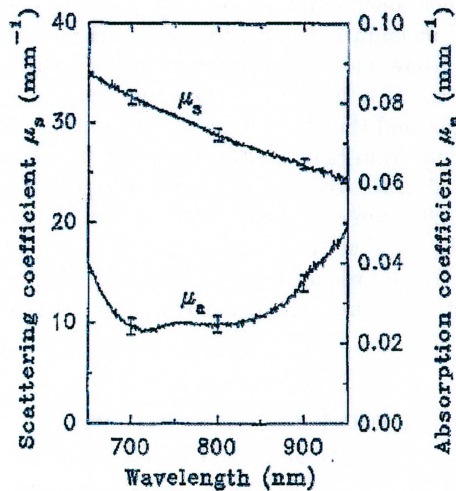


Figure 3.4: The optical properties of bone. The values correspond to data from [29].

A bone consists of bone tissue and water bound within the bone. The absorption profile in the near infrared, where it gradually increases, is due to the water; see Fig. 3.4. In the figure it can also be observed that the scattering decreases with increasing wavelength which corresponds to the Mie scattering wavelength dependence.

Muscles, on the other hand, need a lot of oxygen to work and thus is filled with blood. Blood contains both hemoglobin and water. The hemoglobin affects the spectrum in particular at about 600 nm below which it is responsible for a rapid increase in absorption. Water is not as prominent as hemoglobin but it creates a small increase of absorption in the near infrared area. The scattering decreases with wavelength similar to other tissue types but it is probably not as dense as bone because it scatters only about a fourth of what bone does; see Fig. 3.5.

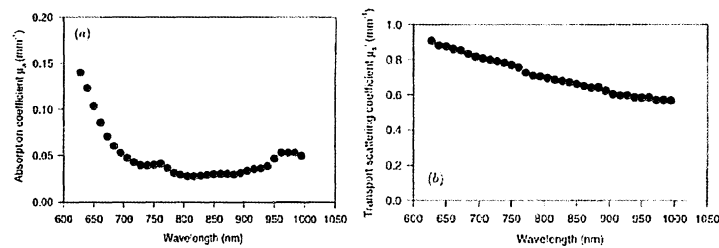


Figure 3.5: *The optical properties of muscles. The absorption coefficient is presented to the left and the scattering coefficient to the right. The values corresponds to data from [30].*

In skin all the mentioned chromophores are present. Because of the smooth absorption curve of melanin it is hard to observe it just by looking at the absorption spectrum. Here one must keep in mind that the concentration of the chromophores have a strong influence. The concentration of melanin is greater in coloured skin types and thus has a more prominent role [30]. The absorption peak at about 600 nm from hemoglobin is present in the absorption spectrum as well as the increasing absorption from water in the near infrared area. In the area between 800 - 2000 nm the scattering coefficient follows the behavior of a Mie scatterer similar to other tissue types. The skin scatters about a fourth of what muscle does. In the region between 400 - 800 nm, scattering similar to that of Rayleigh theory occurs. Smaller particles in the skin begin to scatter as Rayleigh scatterers; see Fig. 3.6.

3.3 Time-resolved measurement

To get additional information about the propagation length of the light within a sample time-resolved techniques can be a powerful aid. It can also be used to determine the scattering and the absorption coefficients of a sample which is very interesting if one would like to simulate the sample in a model. The basic idea of time-resolved measurements is that a short laser pulse is emitted from a source and then propagated through the sample and is detected by a detector

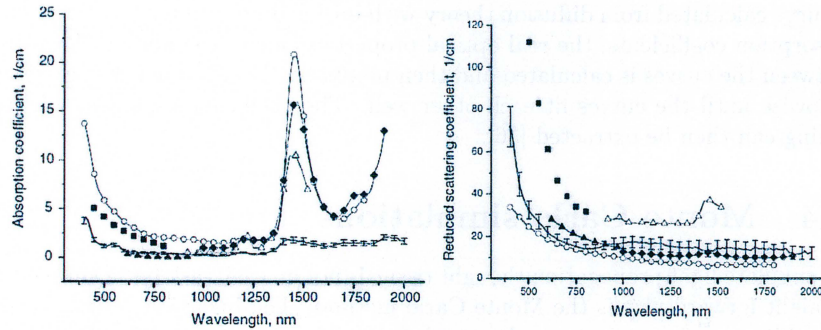


Figure 3.6: *The optical properties of skin. The absorption coefficient is presented to the left and the scattering coefficient to the right. The line correspond to data from [31], the squares correspond to data from [32], the open circles correspond to data from [33], the up triangles correspond to data from [30], the open up triangles correspond to data from [34] and the diamonds correspond to data from [35].*

with a good resolution in time. All light does not propagate through a sample with the same path and especially not in tissue, which is highly scattering. Thus the result from a time-resolved measurement is a distribution in time where the peak is at the mean propagation time; see Fig. 3.7. Because the speed of light is known it is easy to calculate the mean propagation length.

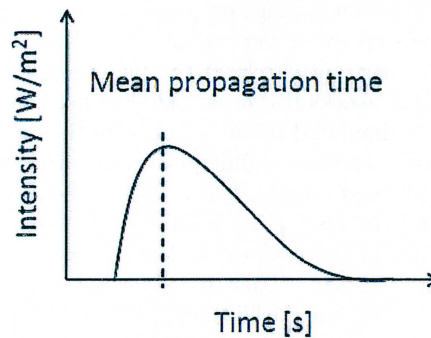


Figure 3.7: *The result from a time-resolved measurement is a distribution with a peak value at the mean propagation time.*

If the absorption coefficient is many times smaller than the scattering coefficient, the mean propagation time can be approximated only to depend on the scattering coefficient. The absorption punishes photons that have traveled a long path and thus the gradient of the slope after the mean propagation time peak is determined by the absorption coefficient. Then if the distance between the emitter and the detector is known, the scattering and absorption coefficient of an unknown sample can be calculated. By comparing the detected curve with

a curve calculated from diffusion theory with initial guesses of the scattering and absorption coefficients, the real optical properties can be calculated. The error between the curves is calculated and then minimized by altering the coefficients stepwise until the curves fit each other well. The coefficients used for the last fitting can then be extracted [36].

3.4 Monte Carlo simulations

To simulate light propagation through tissue is not an easy task but a simple and straight forward way is the Monte Carlo method. The behavior of light within an arbitrary tissue sample can be simulated and be compared with results from, e.g., TOF measurements with the purpose to identify the optical properties.

The process of the method is similar to gambling, take one step forward to a gambling table then an event happens according to statistics, if you "win" you bounce on to a new table and if you "lose", all your money will be absorbed to the bank and you cannot continue. If you are lucky enough you make it all the way out of the casino and you can tell the tale of what happened in there. In the method it is instead a photon that propagates through a simulated tissue slab. Instead of gambling tables the photon has a scattering or absorption processes. If it "wins" the photon is scattered or just passes through and if it "lose" it is absorbed. The probability for the scattering and the absorption processes are determined by the scattering coefficient μ_s and the absorption coefficient μ_a . If the photon propagates through the tissue slab (the casino) it can be detected. The flow chart for a Monte Carlo based simulation program is presented in Fig. 3.8 [37].

Initially, a photon package is created and a step size is calculated. The step size is the distance the photon package propagates before scattering and absorption occur. Hence, the step size is dependent on the scattering and absorption coefficients. Then the program checks if the package is within the simulated tissue and if not, then it checks if the package has been internally reflected or propagated on to a new simulated tissue or out from the model. This happens if the package has moved between two different areas with different optical properties, e.g. between bone and muscle. If it is within the area an absorption will be added dependent on the absorption coefficient to the area where the event occurred and the weight of the package is decreased; i.e., a couple of photons are absorbed from the package. Then it is checked if the weight is below a certain value and if it is not, the package will be scattered. A new angle will be calculated and a new step will be done and the process will start all over again. The scattering angle is dependent on the anisotropy factor g , which determines the scattering distribution; see Sect. 3.1. If the weight is not sufficient then a roulette is started and the photon package has a chance of e.g. one in ten to survive and be scattered again. If it does not survive it is terminated and another package will be created. The cycle continues until all photon packages have been terminated or left the simulated model. For a deeper and more mathematical description of each step the reader is recommended to consult references [37] and [27].

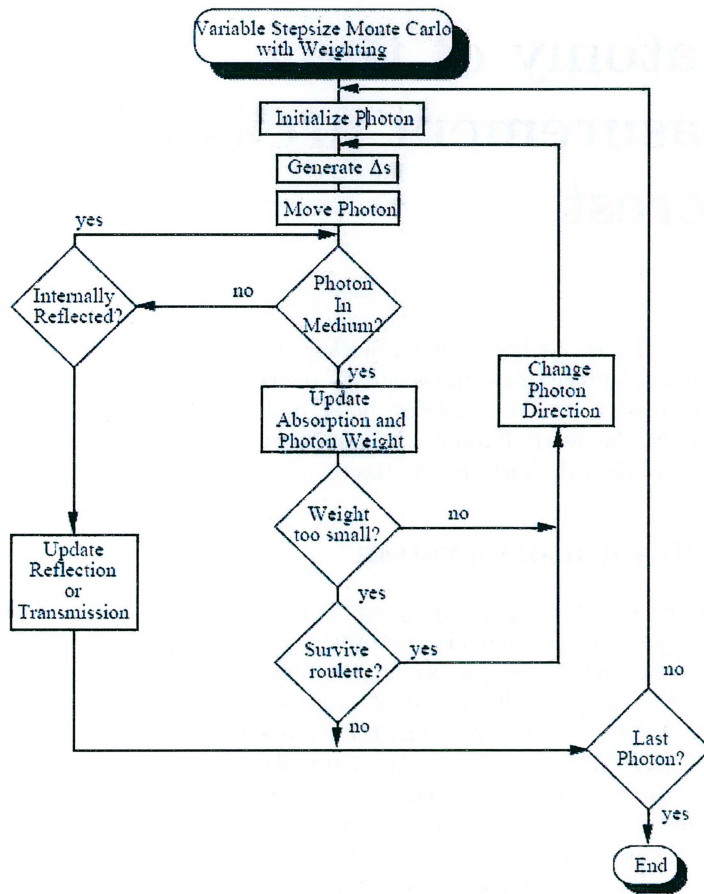


Figure 3.8: Flow chart of a stepwise Monte Carlo method. Taken from [37].

Chapter 4

Anatomy of the measurement areas of interest

In this work focus has been put on measuring gas within the lungs and thus information about the tissue and organs in the thorax area is of interest. Tissue types that matter are skin, muscles, bone, and cartilage while the organs are the lungs and the heart. Initially, the respiratory system and the lungs will be discussed and then the surrounding tissue.

4.1 Respiratory system

The main task of the respiratory system is to transport oxygen into the blood and to transport carbon dioxide and other gaseous metabolic wastes out from blood and the body. The gas exchange is done in the smallest gas filled part of the lung namely the alveoli. An alveolus is a small sack with a volume of about $4.2 \cdot 10^6 \mu\text{m}^3$. In an adult lung there are about 170 alveoli in every cubic millimeter and that sums up to about 480 millions of alveoli [38]. The number varies from person to person. The gas exchange is done through thin walls, alveolar membranes, between the gas chambers and thin capillary beds that surround the alveolus. Pulmonary arteries transport deoxygenated blood from the heart and then the blood stream is divided up into the capillary beds and is oxygenated. The blood is then transported back to the heart by pulmonary veins. The diffusion rate of the gas transport over the thin walls is not fast but because of the vast number of alveoli the total rate is sufficient to oxygenate the entire body. The total area where the gas exchange can be done is about 75 m^2 . An alveolus contains collagen and elastic fibres. The combination of these components allows it to stretch when air is inhaled and spring back when the air is exhaled. On the inside of the alveolus a layer of pulmonary surfactant is situated to prevent it to collapse entirely during an exhale, to keep the air channels dry and to facilitate the gas exchange. The alveoli are gathered into clusters at the end of small air channels called bronchiole - a small bronchi; see Fig. 4.1.

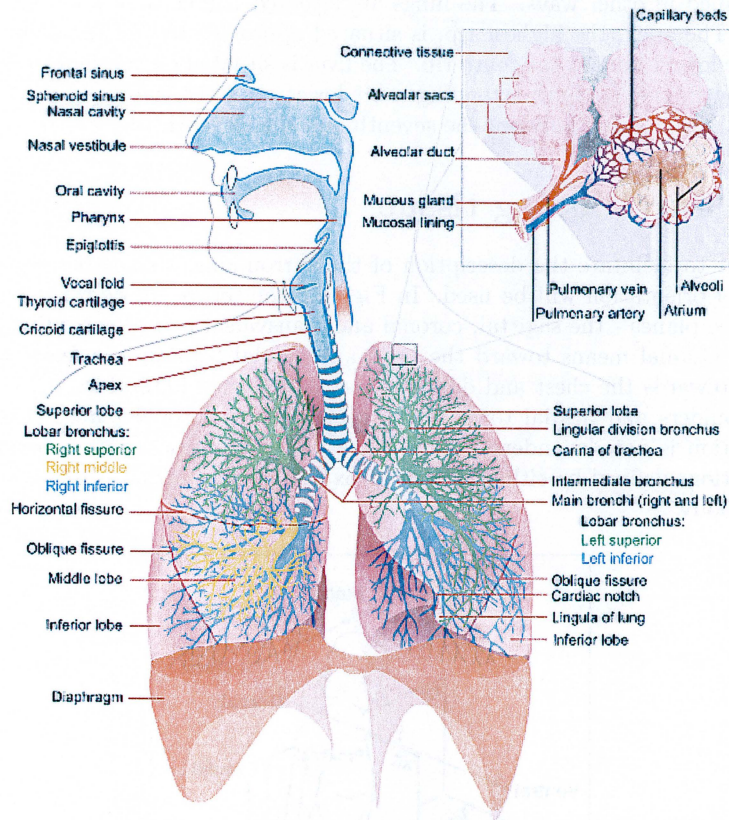


Figure 4.1: *The anatomy of the structures in the respiratory system.*

The bronchi lead into bigger bronchi and create a structure similar to a river delta but in three dimensions instead of two. The main channel into a lung is the main bronchi or primary bronchi which is divided into the secondary bronchi and so on. The primary bronchi is connected to the air pipe or trachea on the other end which is in its turn connected to the oral and nasal cavity; see Fig. 4.1. A lung is divided into smaller sections called lobes. There are primarily three lobes in the right lung and two in the left. The right and the left side refers to the side that would be the right or left if you were looking from the eyes of the studied body. The left lung is smaller because the heart takes space. There are more lobes but they are smaller and unimportant in comparison and thus are not normally referred to as lobe. The lobes closest to the head are called the superior lobes and the ones farthest away are called the inferior lobes. The middle lobe on the right side is just called the middle lobe. The bronchi running through these lobes are called according to the lobe e.g. superior bronchi. In order to exhale, the lungs must be pressed together by mechanical work. The diaphragm muscle is situated below the lungs compresses the lungs. The diaphragm being a muscle is important for example when a person is anesthetized because the muscle relaxants used also relaxes the diaphragm and thus breathing must be

maintained in other ways. The lungs are situated higher than one first might think. The apex, the highest tip, is situated approximately at the collar bone and the lowest part at the tenth rib. The liver is situated on the right hand side resulting in the left lung extending a bit lower than the right. As a reference the heart is situated between the seventh and the eleventh rib.

4.2 Surrounding tissue

In order to facilitate the description of the surrounding tissue the anatomical terms of orientation will be used. In Fig. 4.2 the terms are described. There are three planes - the sagittal, coronal and transversal planes according to the figure. Cranial means toward the head and caudal towards the feet. Ventral means towards the chest and dorsal towards the back. Lateral means towards the shoulders and medial towards the center in the coronal plane. The final orientation is not dependent on the three planes described above, but rather orientations defined by either toward (proximal) or away from (distal) the core of the body.

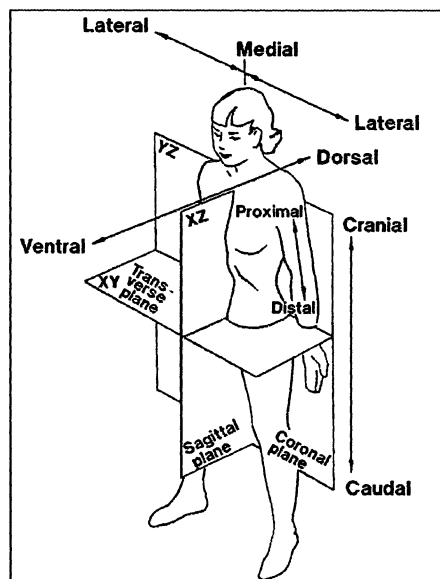


Figure 4.2: *The anatomical terms of orientation* [39].

The most profound bone structure around the lungs is of course the ribcage; see Fig. 4.3. Its purpose is to shield and protect the lungs and the heart but also to create a space where expansion of the lungs can occur unhindered. The ribcage consists of 24 ribs, twelve pairs, and the *sternum*. Each pair is connected with one *vertebrum*. The seven first rib pairs are connected with the sternum directly by costal cartilage and the following three have a common cartilage connection to the sternum. The last two ribs are free floating. It is not uncommon that the number of floating ribs might vary. People can have between zero to three

floating pairs. When a bee waist is wanted in a cosmetic surgery it is these floating ribs may be removed! Another bone structure worth mentioning is the shoulder blades, *Scapula*; see Fig. 4.3. They create an additional shielding on the back and covers cranial and lateral part of the ribcage and lungs.

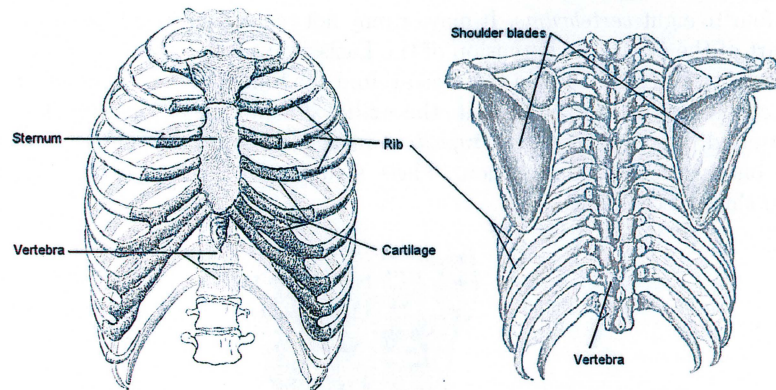


Figure 4.3: Anatomy of the bones surrounding the lungs on the front [40].

The muscles situated around the lungs are primarily the Pectoralis muscles on the front and the *Latissimus dorsi*, *Trapezius* and *Rhomboideus major* on the back.

Pectoralis minor and *major* are the muscles often referred to as the chest muscles. *Pectoralis major* extends between the *sternum* and the *humerus*; see Fig. 4.4. It covers the upper half of the ribcage and the lungs. Dorsal from the *pectoralis major* the *Pectoralis minor* is situated. It extends between the third, fourth and fifth rib and the *coracoid* process of the *scapula*. It covers parts of the lateral and cranial half of the ribcage. Within the ribcage and between the ribs the *Intercostalis muscles* are situated. On the side, the most lateral part of the ribcage, the *Serratus anterior* muscle is situated. It extends over the whole side of the ribcage.

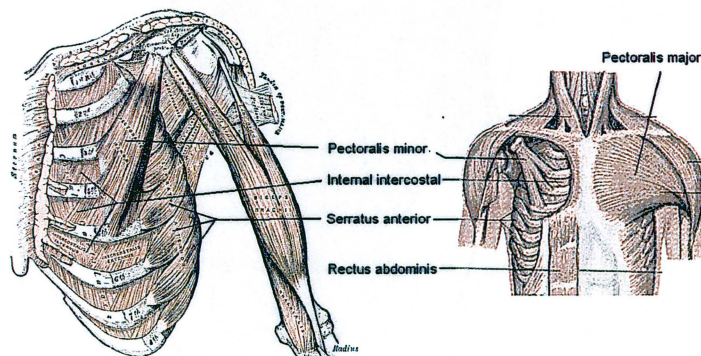


Figure 4.4: Anatomy of the muscles surrounding the lungs on the front [40].

On the back the *Trapezius* muscle covers most of the lungs, at least the medial half; see Fig. 4.5. It is attached on the spine from about the twelfth *vertebrum* to the *cranium* and a part of the *cranium* and extends to the shoulder pad, the *Scapula*. On the caudal part the *Latissimus dorsi* muscle covers the most part. It is also attached to the spine but from the tenth *vertebrum* and down four to eight *vertebrums*. It may or may not reach the Crest of *Ilium* which is a part of the *iliac*. The extension of the *Latissimus dorsi* is very varying from individual to individual but in the area around the lung it is more similar. In the other end it extends to the armpit, the *axilla*. *Rhomboides major* and *minor* are situated dorsally from the *Trapezium* muscle. The minor one is above the major one in the cranial direction. These structures together cover the upper cranial third of the lungs.

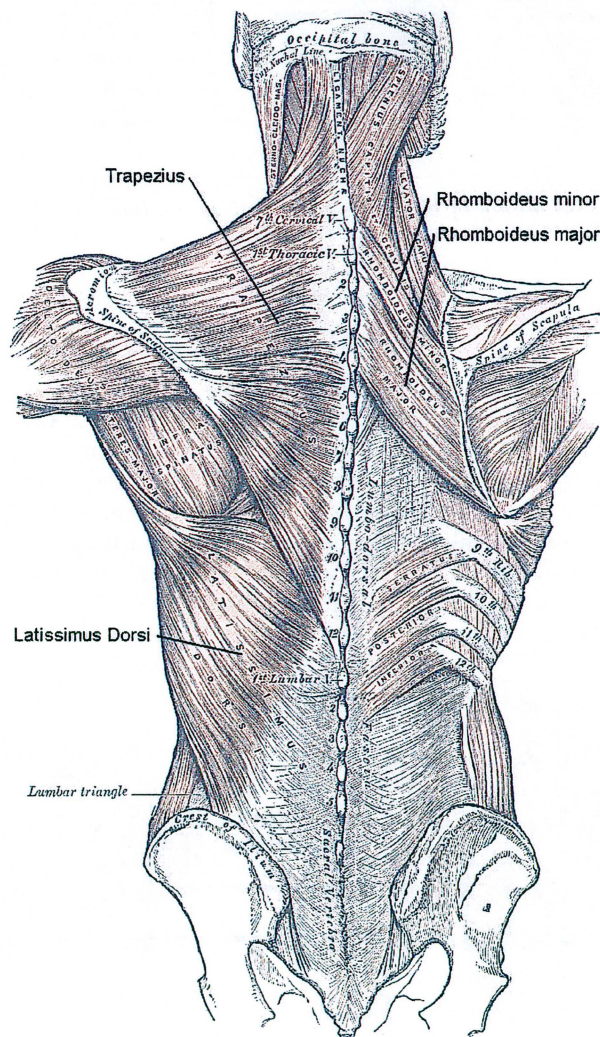


Figure 4.5: Anatomy of the muscles surrounding the lungs on the back [40].

Chapter 5

GASMAS instrumentations

In this part the instrument used for GASMAS measurements will be presented together with a new planned one. The method the instrument uses for detecting the gas absorption will then be described. In Appendix A a MatLab based evaluation program that has been developed with the purpose to facilitate the analysis of the measured data will be presented.

5.1 760/935 nm instrument

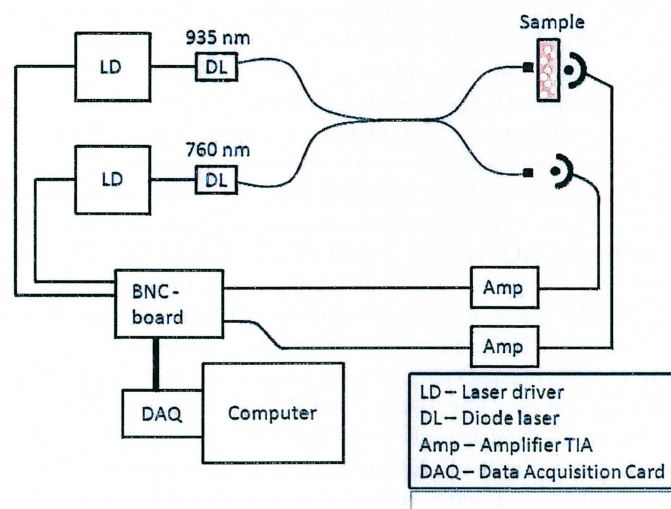


Figure 5.1: *The GASMAS instrument with one 760 nm laser and one 935 nm laser.*

The 760/935 nm instrument detects oxygen at 760 nm and water vapour 935 nm. The instrument was constructed by Lewander et al. [41] for clinical studies of the human sinuses. Two single mode pigtailed DFB type diode lasers from Nanoplus, with wavelengths of 760 nm and 935 nm are used by the instrument.

The diode lasers are called according to the gas they are used to detect. The laser detecting oxygen will from now on be referred to as the "oxygen laser" and similarly for the "water laser". The oxygen laser (emission at 760 nm) is driven by laser driver of model O6DLD103 from Melles Griot, and the water laser (emission at 935 nm), is driven by a driver from Thorlabs; model ITC 502. (The reason for having two different types of drivers is nothing more than that initially both lasers were driven by Melles Griot drivers but then one of them broke and was replaced by the one from Thorlabs).

If the lasers and the drivers are the heart of the instrument the fibres are the arteries. These are manufactured by Laser2000 and are optimized for 760 nm. The laser light from the two different lasers is combined by connecting the fibres with a beamsplitter optimized for 760 nm; see Fig. 5.1. The fibre exiting the beamsplitter is later divided up again into two new fibres with another beamsplitter optimized for 760 nm. The splitting is designed with the goal that 90 percent of the light will be in one fibre and the remaining 10 percent in the other one. The distribution is correct for the 760 nm light but due to the fact that the beamsplitters are not optimized for 935 nm, the distribution will be slightly different for this light. The fibre containing the smallest part of the light is then measured with a silicon based photodiode of model S3590 from Hamamatsu (10 × 10 mm). The fibre with the major part of the light is guided to a probe where the light is emitted. This probe is positioned next to the sample that is to be investigated. The probe is designed to be positioned by hand in order to be able to do measurement on arbitrary samples, e.g. the human sinuses or the human thorax *in vivo*. A hand held detector is designed in a similar fashion to facilitate detection in desired position. The detector is also a silicon based photodiode from Hamamatsu, but of a model S3204, with a larger active surface (18 × 18 mm).

The current from both the reference and the sample detector are amplified and changed into voltages by amplifiers from Femto lasers, of model DLPCA-200. The gain on these amplifiers can be altered in steps of one magnitude from a thousand (10^3) times to a billion times (10^9). The voltages from the amplifiers are led into a BNC board of model BNC-2110 that is connected with a data acquisition (DAQ) card of model PCI-6120 in a PC. The BNC- board and the DAQ- card are from National Instruments. Both voltages are coupled to two different BNC each, one that is undisturbed and one that is AC- coupled in order to reduce low frequency noise. The voltages are recorded by the DAQ- card and are transferred into digital values that are used in a LabView- based program in a computer. The DAQ- card is also the source for a modulation voltage; see Sect. 5.3, that is sent to the laser drivers through the BNC- board.

In order to get as high resolution in the modulation voltage as possible a down converter of the voltage is placed between the BNC- board and the laser drivers. The result is that one can use the whole output voltage scan from the DAQ- card but still have the wavelength modulation that is desired.

The LabView program is the brain of the instrument and it controls the DAQ-card. It is in the program almost all the parameters are set, with exception of the central current to the laser diode (the current that is modulated with the modulation voltage) and the desired temperature of the thermoelectric cooling (TEC) that is set on the laser drivers. The detected signal and the Fourier transform of the signals are also displayed. A 'save' function is implemented in the program to save the detected signals into a file that can be read by MatLab.

5.2 760/820 nm instrument

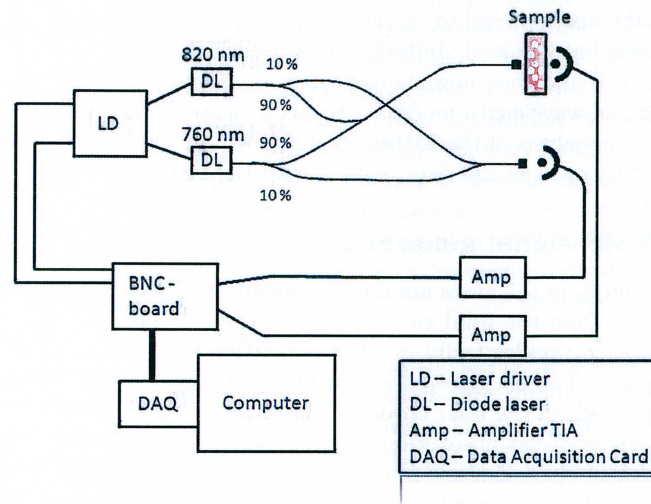


Figure 5.2: The GASMAS instrument with one 760 nm laser and one 820 nm laser.

The planned 760/820 nm instrument is very similar as the 760/935 nm instrument but the main difference is that water is detected at 820 nm and thus a 820 nm laser is used instead; see Fig. 5.2. The laser drivers will also be replaced by a single homemade laser driver. Inside the driver there will be two laser drivers from Thorlabs of model ITC102 will to be built in a box with a common power supply. The fibres will be coupled in a different way as well, the light from each laser will be divided into two fibres one with 90 percent of the light and one with 10 percent. The fibres with minority of the light from both lasers will be coupled together and led to the reference arm and the ones with the majority will also be coupled and led to the sample arm. The fibres that will be used are optimized for 760 nm and thus will have an advantage in comparison with the 760/935 nm because the wavelength difference between the two lasers is smaller and thus the attenuation of the 820 nm light will be smaller than for the 935 nm. The two beamsplitters that will be used in this instrument are optimized for 760 respectively 820 nm, and a WDM (Wavelength-division multiplexer) will be used to couple 760 and 820 nm in the sample arm. Another WDM will be used in the reference arm but it was originally bought to improve the 760/935 nm instrument and thus is optimized for 760 and 935 nm. However, the signal strength in the reference arm is not a problem, even with a mismatched WDM enough signal is obtained.

To single out one of the harmonics a Super Gaussian window is used on the positive peak of the harmonic of interest; see Eq. 5.2 and Fig. 5.5. The multiplication of 2 comes from the removal of the negative frequencies.

$$S_{filt}(\nu) = 2 \cdot S_s(\nu) \cdot \exp\left(-\frac{\nu - n_f \cdot \nu_{mod}}{df}\right)^8, \quad (5.2)$$

where $n_f=1,2,3\dots$ is the number of the harmonic one wishes to filter out, ν_{mod} is the modulation frequency and df is a measure of the width of the window in Hz.

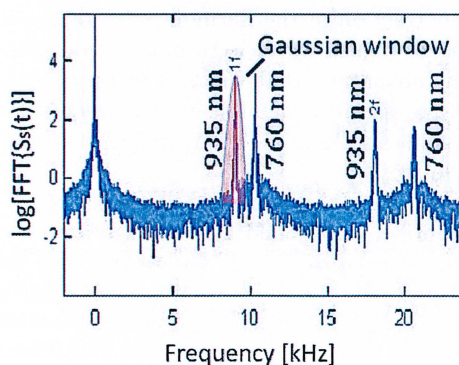


Figure 5.5: A Super Gaussian window is used to single out one harmonic and filter away the rest.

The selected harmonic is then down-converted to zero frequency and transformed back to the time domain in order to study the envelope of the frequency content as the laser is scanned; see Eq. 5.3.

$$s_s^*(t) = F^{-1}(S_{filt}(\nu + n \cdot \nu_{mod})) \quad (5.3)$$

The time dependent signal $s_s^*(t)$ is complex (consisting of a real and imaginary part) and can be studied in a phase-amplitude plot. A phase-amplitude plot is a type of plot where the real part of a the signal is on one axis and the imaginary part is on the other one. The distance to the origin (0,0) is the amplitude of the signal and the angle to the real axis is the phase. A pure sinusoidal signal will only appear as a dot in the plot. In the sweep over the absorption dip the strength of the harmonics changes and thus the amplitude. In the ideal case an absorption will generate a line with 180° phase jumps. It is not only the absorption from the gas that generates modulations of the amplitude but all transmission profiles, i.e. interference effects in the equipment. Thus it cannot be assumed that the signal-to-noise (SNR) ratio is good just because the signal gives rise to a line in the phase-amplitude plot. For harmonics higher than the first, the signal will ideally cross the origin but for the first harmonic there is an offset in amplitude. This originates from the fact that the power of the diode laser also is modulated when the wavelength is modulated; see Sect. 5.3.1. The latter property of the laser is called residual amplitude modulation (RAM). The RAM offset is usually subtracted in order to bring down the signal to the origin. Two examples of phase-amplitude plots are presented in Fig. 5.6, one with 100 cm and one with 9 cm of ambient air between the emitter and the detector.

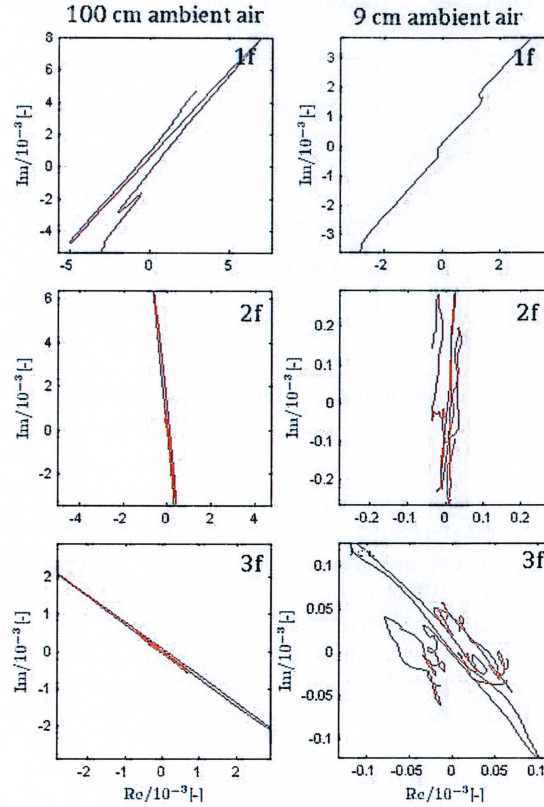


Figure 5.6: Phase-amplitude plots on the three first harmonics of measurements on 100 cm and 9 cm of ambient air.

5.3.3 Intensity normalization

The RAM is very useful when it comes to the normalization of the signal. Normalization of the signal is important in order to derive the absorption; see Eq. 2.1. In setups where only one laser is used the signal can be normalized with the intensity at the absorption. In setups with more lasers the detected intensity is a combination of all the lasers and thus the normalization cannot be done with the detected intensity. In these cases the RAM can be used to extract the intensity of a single laser because the lasers can be separated due to different modulation frequencies. The RAM is proportional to the slope of the intensity. This is a key point because if the transmission of the studied object changes, both the intensity and the slope changes with the same ratio; see Fig. 5.7. Thus the RAM and the intensity will decrease in similar fashion.

Hence, a relation between the intensity and the RAM can be extracted; see Eq. 5.4.

$$I_0 = RAM \cdot c, \quad (5.4)$$

where c is a constant. The constant is independent of the transmission ratio

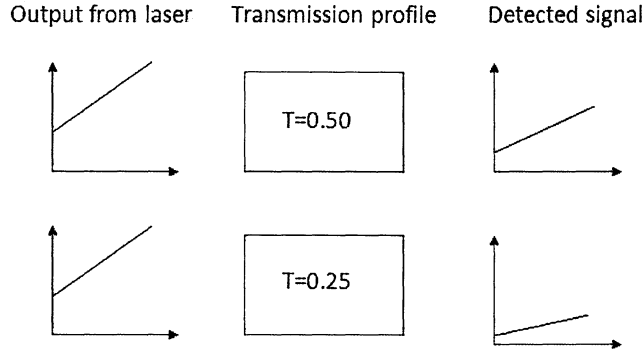


Figure 5.7: Both the slope and the intensity changes with the same ratio.

and can be used in order to calculate the intensity with the RAM. To calculate the value of c a calibration with only the laser at hand is done with known intensity and RAM. RAM normalization is done by dividing the signal with the calculated intensity. When normalizing in the described way it is assumed that the calculated intensity is constant over the whole scan. Higher degree of polynomial can instead be used to follow the slope of the detected intensity. With similar reasoning as for the RAM normalization a similar relation between the intensity and RAM can be assumed but with a higher order polynomial; see Eq. 5.5.

$$I_0 = RAM \cdot (a + b \cdot t + c \cdot t^2 + \dots). \quad (5.5)$$

Here a, b, c, \dots are constants and t is the time. The relation between the intensity and the drive current of a diode laser is usually linear and thus only a polynomial of the first degree is necessary. The 935 nm water vapour laser used in this work is driven with a current close to its limit to get as high output power as possible but in this region the relation is no longer linear and a second degree polynomial is used instead. These calibration values are true for a certain setting of the laser and if this is changed the calibration must be redone.

The mathematical way of describing the normalization is presented in Eq. 5.6 where $\bar{s}_s^*(t)$ is the normalized signal and $s_{1f}^*(t)$ is the signal from the first harmonic. By taking the mean value of the $s_{1f}^*(t)$ one get the RAM value presented in Eq. 5.4 and 5.5. The reason for subtracting the mean value of $s_s^*(t)$ is to remove the amplitude offset. As mentioned in Sect. 5.3.2 the offset mainly exists for the first harmonic.

$$\bar{s}_s^*(t) = \frac{s_s^*(t) - \text{mean}(s_s^*(t))}{(a + b \cdot t + c \cdot t^2 + \dots) \cdot \text{mean}(s_{1f}^*)} \quad (5.6)$$

Which polynomial to be used is dependent on which normalization method is employed.

The normalization of the signal is important to get a quantitatively relevant signal and in order to compare it with ordinary WMS theory.

5.3.4 WMS extraction

Due to the fact that the processed signal is complex (consisting of a real and imaginary part), information is lost in the extraction of the conventional WMS signal. The WMS signal is a projection of the values in a phase-amplitude plot on a straight line. One could say that one dimension of the information is lost. The line is often chosen so that the line goes through the origin and the spot of the signal with the highest amplitude. The phase of the line is then shifted so that the line coincide with the real or the imaginary axel. Then the real or the imaginary part can be extracted and the amplitude variation over time can be plotted and the WMS signal is obtained. It is in the extraction of the real or imaginary part the projection is done. These steps can be expressed in a mathematical way in Eq. 5.7.

$$WMS(t) = Real\{(\bar{s}_s^*(t) - mean(\bar{s}_s^*(t))) \cdot exp(-i\beta t)\}, \quad (5.7)$$

where β is the angle the phase is shifted. The WMS signal is dependent on which harmonic is studied. The first harmonic has one internal node, the second one two and the third one three and so on; see Fig. 5.8.

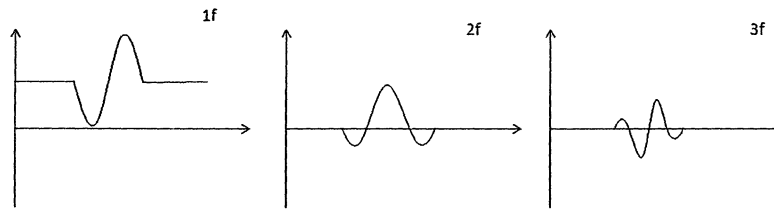


Figure 5.8: *The first harmonic has one internal node, the second one two and the third one three.*

The fact that information is lost in the extraction of the WMS signal can in many cases be accepted because in WMS theory it is the peak value that is used. In WMS theory the amplitude peak value of the first harmonic represents 50 % of the absorption, the second represents 34 % the third 23 % with the assumption that the WMS signal profile is a Lorentzian [42]. If it is a gaussian other values are to be used.

5.3.5 Absorption signal evaluation

The measure of the gas absorption in GASMAS is a length that is equivalent to a distance in ambient air with the same absorption. Thus the equivalent length, L_{eq} , is a product of the length the light has traveled and the ratio of concentration of the gas in the sample and in ambient air; Eq. 5.8.

$$L_{eq} = \frac{c_{samp}}{c_{amb}} \cdot l \quad (5.8)$$

The equivalent path length has in this work been calculated primarily in two different ways. The first one is called Fringe Matching and uses the fact that the peak value of the signal amplitude represents a set percent of the gas absorption.

The second is called Absolute Reference evaluation and compares the absorption signal with an absorption signal from a known distance. To reduce the effect of unwanted phase shifts and amplitude variation from the equipment both techniques uses a background signal. This is produced by splitting the light from the laser with a beam splitter and letting some of the light be detected with only a very small distance of ambient air between a secondary emitter and detector. The primary emitter and the associated detector are called the sample arm and the secondary are called the reference arm; see Sect. 5.1. The way the background signal is implemented in the evaluation of the signal differs for the techniques. In the Fringe Matching technique the fringes (the constant part next to the signal; see Fig. 5.9) of the WMS signal from the sample arm are matched (set at the same level) with the signal from the reference arm.

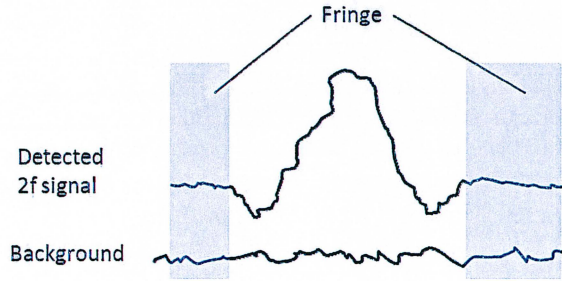


Figure 5.9: In Fringe Matching the fringes on the sample signal are fitted to the background and then the background is subtracted.

Then the background is subtracted and the absorption can be calculated; see Eq. 5.9.

$$Abs = \frac{1}{c_{nf}} \cdot \max(\bar{s}_s^*(t) - \bar{s}_{bgr}^* - d_{match}^*). \quad (5.9)$$

Here c_{nf} is a constant that is dependant on which harmonic is being analyzed and describes how many percent the peak value represents of the absorption. \bar{s}_{bgr}^* is the intensity normalized background signal and d_{match}^* is the matching constant. To calculate the equivalent path length, the absorption coefficient must be extracted from the spectral data of the interrogated line. The information can be found in the database HITRAN which is a acronym of high-resolution transmission molecular absorption database. The information taken from HITRAN must be converted in order to extract the absorption coefficient. The transmission through a gas filled tube with a set length can be simulated with a program called Spectracalc which uses the HITRAN database. Through the simulated transmission factor, T , and the absorption coefficient, α , can be calculated with the relation in Eq. 5.10. Compare with the Beer-Lambert law; see Eq. 2.1.

$$T = \exp(-\alpha l) \quad (5.10)$$

When the absorption coefficient and the absorbance are known the equivalent path length can be calculated; see Eq. 5.11

$$Abs = \exp(\alpha L_{eq}) \quad (5.11)$$

The Fringe Matching method depends on the fact that calculation of the absorption coefficient is correct. This might not be the case if there are any uncertainties in the properties of the environment the measurements is done at or if the HITRAN database is a little faulty. These uncertainties are very hard to validate and thus, in earlier work with this method, the standard addition technique was used instead of employing the absorption coefficient. In this method, a calibration curve is made by step wise increasing the distance of ambient air and measuring the peak value of the absorption signal.

In the Absolute Reference evaluation method, a calibration measurement through a know distance of ambient air is made and the absorption signal from the measurement is called the absolute reference. Depending on what gas concentration is of interest, the reference gas in which the reference measurement is done can be any gas, not only ambient air. The equivalent path length is dependent on the reference gas and thus the concentration of the reference gas is important. In this work water vapour and oxygen are measured and thus ambient air is a easily accessible and a good reference. The concentration of water vapour in ambient air is depending on the relative humidity and the temperature. To correlate the measured gas absorption from the absolute reference measurement with the absorption signal from the gas inside the studied object, the conditions of the gas must be know.

Gas in tissue can be assumed to have a relative humidity of 100 %. The Arden-Buck equation; see Eq. 5.12 is used to calculate how long the equivalent path length of the water absorption signal from the sample would be in ambient air at a certain temperature and relative humidity.

$$p_w = 6.1121 \cdot \exp\left(\frac{(18.678 - \frac{T}{234.5})T}{257.14 + T}\right). \quad (5.12)$$

Here p_w is the saturation water pressure in hPa and T is the temperature in Celsius. The ratio between the water pressures times the ratio between the relative humidity for the two different conditions is proportional to the ratio between the equivalent path length. The concentration of oxygen in air is 21 %. The model that the Absolute Reference method uses is stated in Eq. 5.13.

$$\bar{s}_s^*(t) = p^*(t) + q^*(t) \cdot s_{bgr}^* + c \cdot \bar{s}_{abs.ref}^*(t - t_0). \quad (5.13)$$

Here $p^*(t)$ and $q^*(t)$ are complex polynomials that handle the difference between the sample and reference signals. These differences are phase and amplitude alterations due to the studied sample. The real constant c describes the ratio between the absorption signal from the absolute reference and the sample absorption signal. The time shift constant t_0 is implemented to remove possible drifts of the laser between the sample measurement and the absolute reference measurement. To identify the absorption signal within the sample signal, the model; see Eq. 5.13, is fitted on the sample signal. The best model fit is performed by optimizing the mean square method with the non-linear Levenberg - Marquardt algorithm. The result from the fitting gives the $p^*(t)$ and $q^*(t)$ but also the fraction constant c_{fit} . For an example of a fitted signal see Fig. 5.10. The equivalent path length can be calculated; see Eq. 5.14.

$$L_{eq} = c_{fit} \cdot L_{abs.ref}, \quad (5.14)$$

where $L_{abs.ref}$ is the distance of ambient air measured in the absolute reference measurement. The distance is often chosen to one meter because then the

absorption signal and the SNR ratio is sufficient large while the measurement is easy to do.

The Fringe Matching method using the absorption coefficient is a good way to control if the theory correlates with what is expected from the measurements. Because of the uncertainty in the method this might only give an indication of what is to be expected. To get a reliable result either the Fringe Matching method with the standard addition approach or the Absolute Reference method should be used. The process for the standard addition Fringe Matching method is not as direct as the Absolute Reference method and thus the latter is preferred. The software requirements for the Absolute Reference method is greater than for the Fringe Matching method but the physical work needed for each measurement is greater for the Fringe Matching method which does not use the gathered information as effectively.

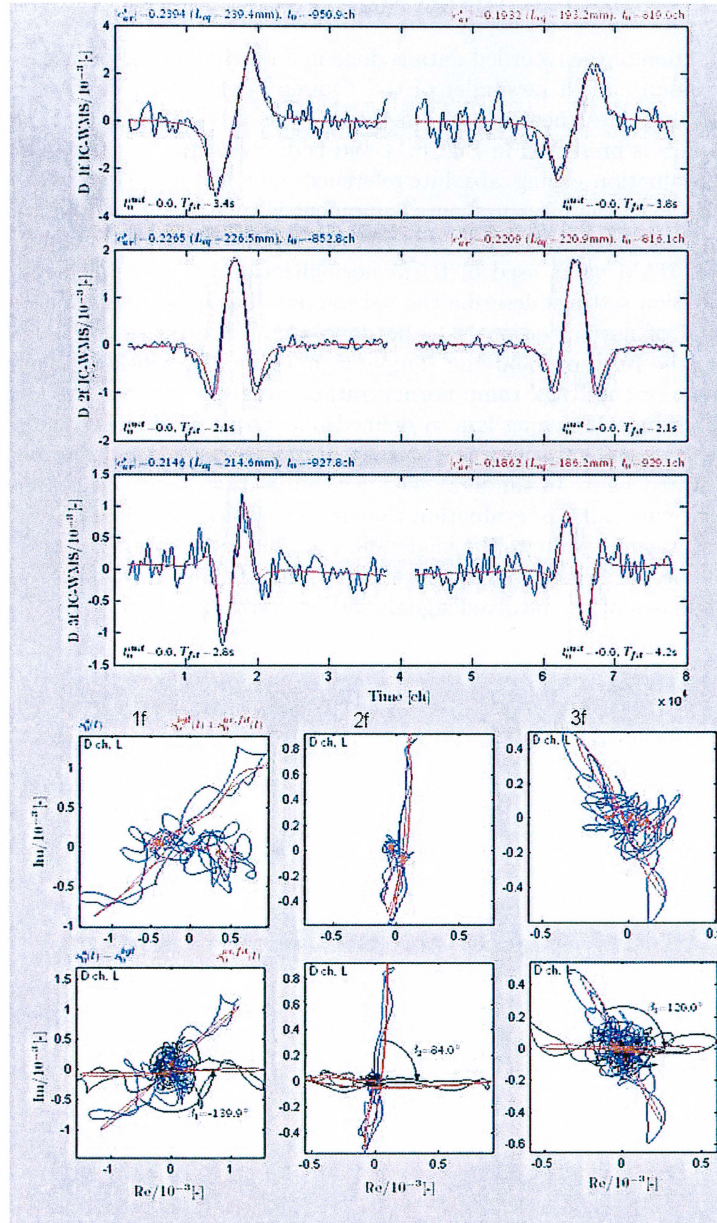


Figure 5.10: Phase-amplitude plot and WMS-signals from a sampled signal from a boar lung with the tree first harmonics evaluated. The upper phase-amplitude plots are from the direct sampled signal and the lower ones are when the background signal has been removed. The red line represents the model fit on the signal and the blue the signal. In the background reduced phase-amplitude plots there are also a black one which represents the signal when the phase has been altered in order to direct the signal parallel with the real axis.

5.4 Evaluation program

The evaluation of the recorded data is done in a MatLab based program written by T Svensson and M Lewander of the Atomic Physics Division in Lund [41]. The program is designed to perform the analysis steps described in Sect. 5.3. The interface is presented in Fig. 5.11 and is divided into four parts, hardware settings, evaluation setting, absolute reference and load file. In hardware setting, parameters from the measurements equipment is treated e.g. sample frequency and signal amplification. The ratio of the average transmitted signal voltage and the 1f RAM value used in RAM normalization is also implemented here. The evaluation settings describe the parameters that effect the evaluation, e.g. which kind of normalization is to be done and if the phases of the absolute reference, the reference and the sample signal should be locked in some way. Parameters for the RAM ramp normalization are also set here. The evaluation region for Fringe Matching is also defined under this section. In the absolute reference section the file with the absolute reference is selected. Parameters for this are stated here. In the final section the files that are to be evaluated are loaded and what kind of evaluation that is to be made is selected. There are a number of ways to evaluate the loaded files but in this work either the Absolute Reference or the Fringe Matching is used. One of these methods is used but with the phases of the involved signals set in a certain way.

File format: D & HP channels, 25 lines header (NI-6120) ▾

Hardware settings

Sample freq. [S/s]	400000	Responsivity [A/W]	REFERENCE CH. [0.53,0.64]	SAMPLE CH. [0.53,0.64]
Scan freq. [S/s]	5	TIA gain [V/A]	1e4	1e6
Modulation freq. [Hz]	[10295 9015]	HP gain [-]	1	1

Expected dataset size: 80000

Gas: Oxygen ▾

Frequency coefficient [1/mm] []

Absorption coefficient [1/mm] 2.7e-5

1f calibr. factor [U_avg/1f RAM] [26.263098448176919 29.3436961575492]

Evaluation settings

Filter width [Hz]	500	Non-inprint range [8 element vector]	[1,10000,30000,40000,40001,50000,70000,80000]
Baseline order	1	Evaluation range [4 element vector]	[2000,36000,42000,78000]
Ref. baseline order	1	Phase locking (if applicable)	<input type="checkbox"/> Lock to abs. ref. <input type="checkbox"/> Lock ref. ch. to sample ch.
2f efficiency []	0.3	Intensity correction	<input type="radio"/> Intensity normalisation <input type="radio"/> 1f RAM normalisation <input checked="" type="radio"/> 1f RAM ramp normalisation
Harmonics	[1,2,3]	RAM ramp coeff	[0.85904, 1.14516]

Absolute reference

Absolute reference: no datasets have been imported ▾

Leq [mm] 1000

Shift [ch] 0

Baseline order 0

Ref. baseline order 0

Skip fringe matching of abs. ref.

Import data

Dataset: no datasets have been imported ▾

View: Raw data ▾

Figure 5.11: The interface of the MatLab based analysis program.

Chapter 6

Measurement and simulations

6.1 Simulation on the benefits of a 820 nm laser

6.1.1 Introduction

To verify the gain when measuring water vapour at 820 nm instead of 935 nm simulations and measurements was done. The optical properties of the tissues used in the simulations are taken from the diagrams in Sect. 3.2. To verify the simulation results experimental measurements were also performed. To make the comparison possible a good sample volume must be chosen. It should have similar tissue types as the thorax area and at the same time have a thickness that could be altered. The human finger and hand were the best options that could be thought of.

6.1.2 Simulation of penetration depth

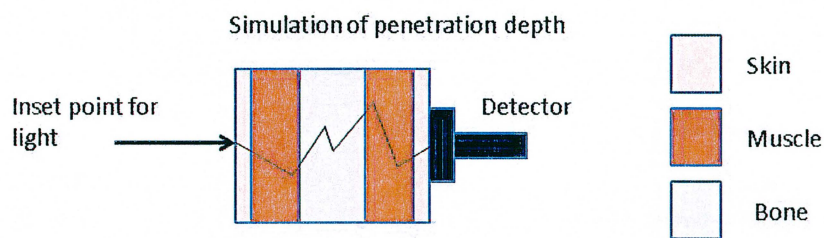


Figure 6.1: *The simulation model of the finger/hand. It consists of five layer, two of skin, two of muscle and one of bone. The skin layers were set to a thickness of 1.5 mm independent on the sample thickness and the rest were 50 percent muscle and 50 percent bone.*

The model of the finger/hand is constructed by five layers, two skin layer on the outer part, two muscle layers within these and between them a layer

of bone; see Fig. 6.1. During the simulation the thickness of the sample was increased until only a thousandth of the emitted power was detected with a circular detector having a radius equal to half the side size of the real detector; see Sect. 5.1. The instrument can handle signal strengths smaller than this but the output from the fibre probe is about 1 mW and a nice signal with a high SNR can be detected with about 1 μ W. The thickness of the skin layers was set to 1.5 mm [43] independent of the sample thickness and the rest of the sample thickness were equally divided between muscle and bone tissue. The simulation is done with a MatLab-based function that creates a multi-layered structure in a Monte Carlo program. The MatLab function works as an interface for the Monte Carlo program. The MatLab functions are described in [44].

The simulated penetration depths before losing 99.9 % of the initial power are presented in the table below.

Wavelength $\lambda[nm]$	Penetration depth $l_{pen}[mm]$
760	25
820	26
935	23

The difference in penetration depth between 935 nm and 820 nm is not that large, the additional penetration depth correspond to a 13 % gain.

6.1.3 Experimental penetration depth

To verify the simulation results and to get a feeling for what the real penetration depth would be, experimental measurements were done. The emitted powers from the different lasers from the fibre probe was measured with a optical power meter. The power of the transmitted light was detected by the sample detector but with a circular mask over it so it would have the same shape as the one in the simulation; see Sect. above, at different finger/hand thicknesses. The position were chosen with increasing thicknesses until the ratio between power of the detected and the emitted light was below 10^{-3} .

The results from the penetration depth measurements are presented in Fig. 6.2. The oxygen laser (760 nm) has the weakest attenuation of the light, then comes the 820 nm laser and finally the water laser (935 nm) with the strongest attenuation. The 820 nm laser has about 10 % deeper penetration than the water laser before losing 99.9 % of the output power from the fibre.

6.1.4 Discussion

In the simulations the 820 nm laser had the deepest penetration while in the measurements it was the oxygen laser. The penetration depth gain by measuring water vapour at 820 nm instead of 935 nm was larger in the simulation than in the measurements (13 % resp. 10 %). The reason can be that in the simulations 50 % of the finger, except the skin, was assumed to be muscle and the rest bone. The distribution of bone and muscle might be different. To take the optical properties from the skull to be applied to the bone might also give differences. The magnitude of the penetration depths are similar between the simulations and the measurements which indicates that the optical properties at least are in the right order for the different tissue types.

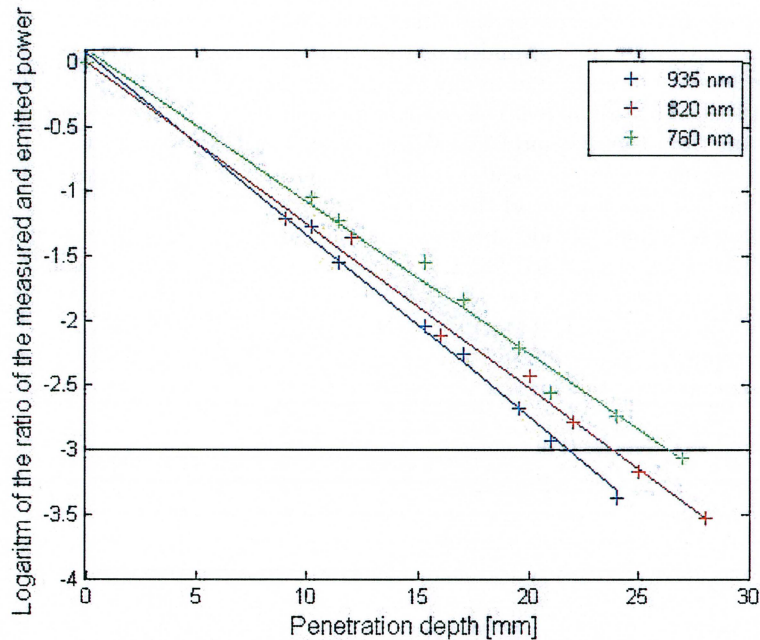


Figure 6.2: The logarithm of the ratio between the emitted and detected power for three different lasers through varying tissue thicknesses. The black line indicates when 99.9 % of the initial power is lost.

The disadvantages with detecting water vapour at 820 nm instead of at 935 nm is that the absorption lines at 820 nm is more than ten times weaker than the lines at 935 nm; see Sect. 2.3. However, the oxygen absorption line has similar strength as the one at 820 nm and it is sufficient. The advantages are as shown in these measurements and simulations with the increase in the penetration depth. In addition the fibres have a bandwidth in which the attenuation of the light is low and 760 nm and 820 nm are closer in wavelength than 760 nm and 935 nm. This simplifies finding equipment that fits both lasers. The optical properties are also more likely to be similar if the wavelength distance is smaller. The ratio between the path length of the light for the oxygen and water laser will then also be smaller.

6.2 Initial measurements on boar lung

6.2.1 Introduction

The purpose of this experiment was to confirm that a gas absorption signal could be obtained through lung tissue for dimensions typical to neonates and also get more information about how the geometry of the lung effects the signal. A lung consists of many small cavities while earlier clinical work with the GASMAS instrument have mostly been done on one unison cavity, a frontal or a maxillary

sinus [2, 25]. However, the mastoideus, the bone behind the ear, which has many small compartments has been studied. Tissue phantoms made of water, gelatine, titanium oxide and ink, and a boar lung, were used to study if measurements on neonates were possible.

The boar lung was provided by the slaughter house Skånska Vilt in Vinslöv, Skåne. The boar was shot the day before, January 17, 2010 and slaughtered on the same day as the measurements were done. The lung was transported to Lund in a plastic bag in a icebox with ice and snow.

In order to inflate the lung a steady flow of compressed air was used; see Fig. 6.3. The air was directed by a tube to a secondary bronchus in the lung and a cut was made in the lung in order to prevent the lung from bursting due to the pressure.

Each measurement series was done with five separate measurements with an averaging over 50 measurements corresponding to 10 seconds.

The temperature of the gas in the lung could not be measured during the measurements but it was estimated by assuming that the oxygen and the water absorption signal should be equal. Through the comparison the temperature was estimated to 14 °C and it was used for all the measurements. The temperature is important to know because the water vapour concentration is dependent on it.



Figure 6.3: *The lung was inflated by a steady flow of compressed air.*

6.2.2 Transmission measurement

To study the possibility to obtain a gas absorption signal and the effects of the geometry of the lung, transmission measurements were done on two positions, A and B; see Fig. 6.4. For position A the thickness of the inflated lung was approximately 3 cm and in B it was 2.5 cm; see Fig. 6.4. Measurements were made both in the mid-morning and the afternoon to study possible changes that may have happened due to the ageing. In the mid-morning three measurements series were made, one with only the oxygen laser turned on in position A and two with both oxygen and water lasers turned on, in position A and B, and in the afternoon two ordinary in position A and B. The first measurements on position A in the morning were done with an averaging over 100 measurements but after evaluating the data from this position it was realized that 50 averages were sufficient due to the large absorption signal.

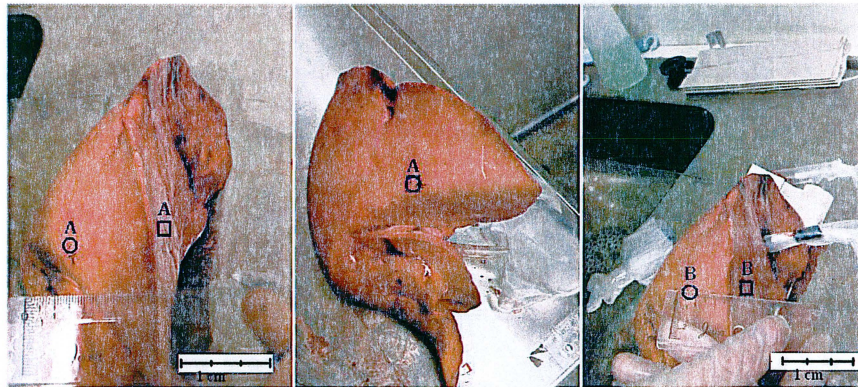


Figure 6.4: Placement of the fibre probe and the detector at the measurements on position A and B. The square represent the position of the fibre probe and the circle the position of the detector.

The measured equivalent path lengths from the measurement series are presented in Fig. 6.6. Some of the measurements in position A did not have sufficient SNR ratio when evaluating the water signal due to too low transmission of light to the detector, and were therefore discarded. The SNR ratio of the oxygen signals were not very good but sufficient to be acceptable; see Fig. 6.5.

When comparing these results with results from measurements on the human sinuses [25] it was observed that the oxygen absorption signals are approximately one magnitude larger. The distance the light has traveled in air is approximately one magnitude longer than in the sinuses. With the assumption that the distance between the fibre probe and the detector is approximately the same, the conclusion is that geometries with many small cavities scatter light to a greater extent than ones with one unison cavity, which is expected. Due to the relatively high scattering of the light in this geometry the possible penetration depth is decreased.

It can be observed that the measurements done in the mid-morning have a larger absorption signal than the ones done in the afternoon. The reason for the

decrease is probably due to the fact that some of the cavities in the lung stuck together while the lung was in a collapsed state during lunch. When flushing the lung again in the afternoon not all cavities were opened and filled with air. Resulting in that there were less gas to probe. An additional factor might be that the lung dried a bit between the measurements in the mid-morning and the afternoon, resulting in a decrease in scattering and absorption. The mean propagation path length in the alveoli would then decrease and with it the absorption.

The power out from the fibre probe was measured with an optical power meter for both lasers one at a time. The transmitted powers and the transmittances of the lasers beams for the different measurements are presented in the table below. Here the output powers are also presented.

Wave-length	Output from fibre	Power Pos. A mid-morning	Power Pos. B mid-morning	Power Pos A afternoon	Power Pos A afternoon
$\lambda[nm]$	$P_0[\mu W]$	$P_T[\mu W]/\frac{P_T}{P_0}[-]$	$P_T[\mu W]/\frac{P_T}{P_0}[-]$	$P_T[\mu W]/\frac{P_T}{P_0}[-]$	$P_T[\mu W]/\frac{P_T}{P_0}[-]$
760	2340	0.260 / 1.11×10^{-4}	0.975 / 4.16×10^{-4}	0.270 / 1.15×10^{-4}	3.000 / 12.8×10^{-4}
935	1270	0.018 / 1.42×10^{-5}	0.094 / 7.40×10^{-5}	0.012 / 0.94×10^{-5}	0.310 / 2.44×10^{-5}

Comparing the transmitted power with the absorptions signal it can be observed that with lower transmitted power the absorption signal increases, which could be expected. It can also be observed that the water laser light is more attenuated than the oxygen laser which also could be expected due to the comparatively large absorption of the 935 nm light by the water in the tissue.

6.2.3 Transmission measurements with tissue phantoms

To simulate tissue surrounding the lung a type of gelatine-based phantoms were made of 250 ml water and 25 g gelatine. Mixed in the phantoms were 275 mg titanium dioxide to modify the scattering coefficient, and 0.75 ml ink (Pelikan Indian ink) to modify the absorption coefficient. The phantoms produced were 1.7 cm and 2 cm thick. They were optimized for a wavelength of 760 nm and the values of the reduced scattering coefficient and absorption coefficient were those of an adult human abdominal muscle, $\mu'_s = 7 \text{ cm}^{-1}$ and $\mu_a = 0.3 \text{ cm}^{-1}$ [30]. The values of the adult abdominal muscle were used because it was assumed that the pectoralis and the abdominal muscles have the same

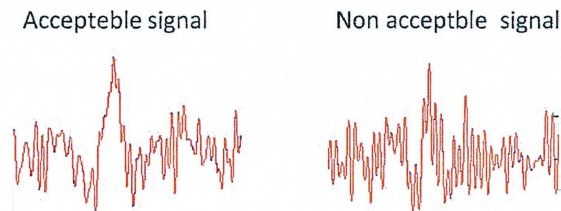


Figure 6.5: Examples of an acceptable and a non acceptable WMS signal.

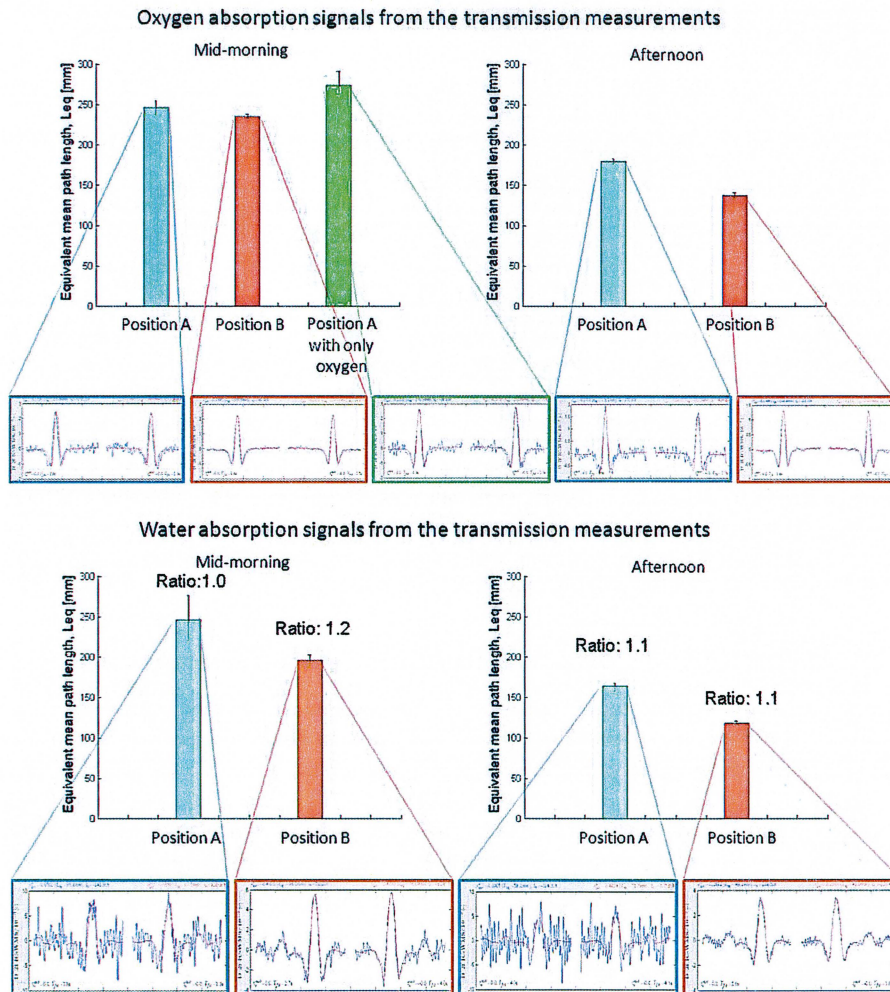


Figure 6.6: Results from the transmission measurements with the assumption that the temperature was $14^{\circ}C$. The ratio between the oxygen and the water absorption signal is presented in the water diagrams.

constituents, and that the difference between a muscle on a adult and on a child is not that large. The titanium dioxide is known to have approximately the same wavelength dependence as human tissue and due to the similar behavior, the scattering coefficient at 935 nm can be assumed to be correct [45]. The absorption coefficient at 935 nm is harder to predict but the ink is assumed to have a quite constant value over a broad spectrum of wavelengths and the abdominal muscle has almost the same value at both 760 nm and 935 nm. Hence, the absorption coefficient is assumed to be correct at 935 nm as well. To confirm the assumptions and that desired properties were obtained time-resolved measurements were preformed; see Sect. 6.2.5.

First the 2 cm thick phantom was placed on one side of the lung and a measurement series was done with the fibre probe in contact with the phantom and the detector on the other side of the lung; see Fig. 6.7A. Between the fibre probe and the detector there were approximately 2 cm of lung tissue.

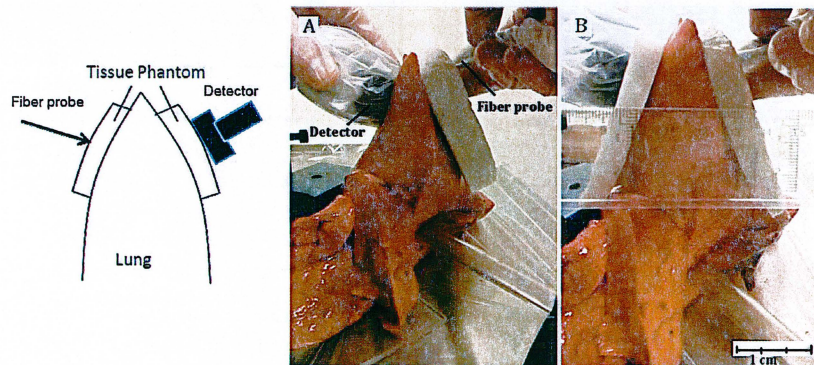


Figure 6.7: *Position of the detector and the fibre probe in measurements with a 2 cm wide tissue phantom placed on one side of the lung, in the center, and in measurements with the two halves of the split 2 cm tissue phantom on either side of the lung, to the right. The principal model is presented to the left.*

The second tissue phantom (1.7 cm thick) was placed on the other side of the lung and a measurement series was done with approximately 2 cm of lung tissue between the fibre probe and the detector. In these measurements very little light reached the detector. To get a geometry more similar to the neonates, the 1.7 cm phantom was removed and the 2 cm split in two pieces and placed on each side of the lung; see Fig. 6.7B. A measurement series with approximately 2 cm lung tissue was done.

The results of the measurements are presented in Fig. 6.8. From these results it is observed that it is possible to get a transmission signal in geometries that could be similar to small neonates but not in the larger ones. The transmitted powers and the transmittances for the measurements with the different phantoms are presented in the table below. The output power from the lasers are also presented.

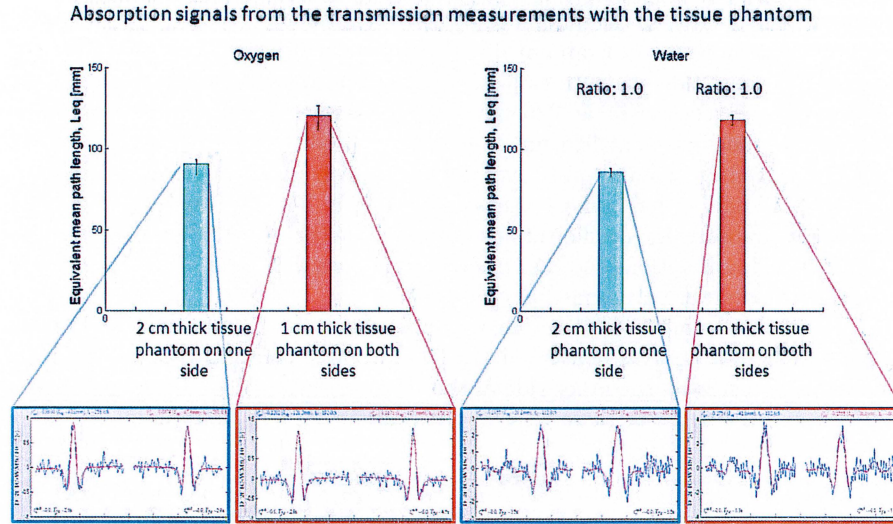


Figure 6.8: Results from the transmission measurements with the tissue phantoms with the assumption that the temperature was 14°C . The ratio between the oxygen and the water absorption signal is presented in the water diagrams.

Wavelength	Output from fibre	Power One 2 cm phantom	Power One 2 cm and one 1.7 cm phantom	Power Two 1 cm phantoms
$\lambda[\text{nm}]$	$P_0[\mu\text{W}]$	$P_T[\mu\text{W}]/\frac{P_T}{P_0}[-]$	$P_T[\mu\text{W}]/\frac{P_T}{P_0}[-]$	$P_T[\mu\text{W}]/\frac{P_T}{P_0}[-]$
760	2340	0.505 / 2.16×10^{-4}	0.062 / 0.65×10^{-4}	0.440 / 1.88×10^{-4}
935	1270	0.105 / 8.27×10^{-5}	0.013 / 1.02×10^{-5}	0.085 / 6.69×10^{-5}

6.2.4 Reflection measurements with tissue phantom

In these reflection measurements the possibility for the light to penetrate into the lung and then be reflected back was studied. One of the 1 cm thick pieces of the split 2 cm tissue phantom was placed against one side of the lung; see Fig. 6.9. To avoid air between the phantom and the lung pressure of fibre and detector was applied. This was important because if there is a void with air, the light might take a shortcut through the void and give rise to an absorption signal without ever penetrate into the lung. Two measurement series was done with different distances between the fibre probe and the detector. First the distance was chosen so that a good amount of light reached the detector and then a larger distance was chosen so only a little light reached the detector. The second distance was chosen because although not much light reaches the detector it often carries a larger and better absorption signal.

Some of the measurements done in the second round were discarded due to the fact that the SNR ratio was too bad and no clear absorption signal could be identified. The rest of the results are presented in Fig. 6.10. The absorption

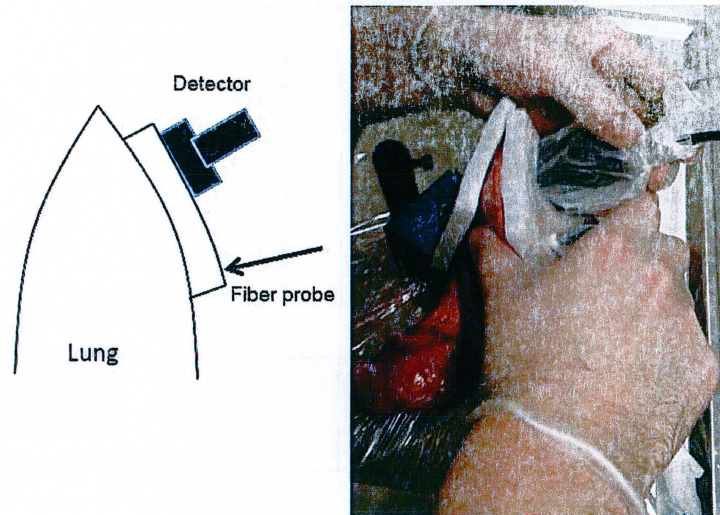


Figure 6.9: In the reflection measurements a 1 cm thick tissue phantom was placed on one side of the lung and the fibre probe and the detector were placed on the same side. The principal model is presented to the right and the real model on the left.

signals in the first measurement series is one order of magnitude smaller than in the transmission case. This indicates that the penetration into the lung is quite shallow for the light that reaches the detector. It is also observed that in these measurements the water and oxygen absorption signals do not match as well as the rest of the measurements and this could be due to the temperature. The outer parts of the lung were in close contact with the snow during storage so eventually the temperature in these parts were lower. A temperature lowered by, 3°C i.e., 11°C would give the correct match. It was also these parts that were the most likely ones to increase in temperature when the lung was removed from the storage. Another more probable explanation are that the geometry will effect the ratio between the oxygen and water absorption signals. The light from the oxygen laser penetrates deeper than the light from the water laser. Hence, the path length will be longer for the light from the oxygen laser and it will probe a larger amount of gas increasing the absorption signal.

The transmitted powers and transmittance for the oxygen and the water lasers are presented in the table below together with the output from the lasers. It can be observed that the ratio between the transmitted power from the oxygen and the water laser is smaller in these measurements than in the rest and the explanation is probably that the light has not traveled through as much tissue and thus has not attenuated to the same extent.

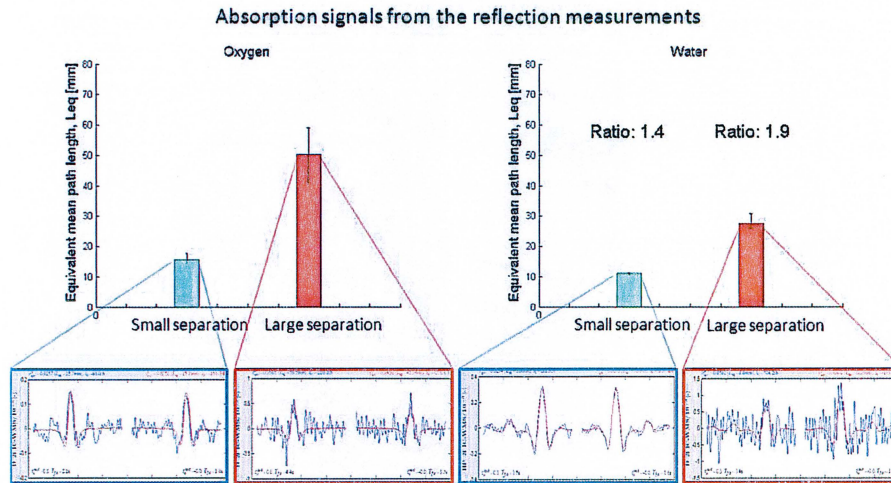


Figure 6.10: Results from the reflection measurements with the assumption that the temperature was 14°C . The ratio between the oxygen and the water absorption signals are presented in the water diagrams.

Wavelength $\lambda[\text{nm}]$	Output from fibre $P_0[\mu\text{W}]$	Power small distance $P_T[\mu\text{W}]/\frac{P_T}{P_0}[-]$	Power big distance $P_T[\mu\text{W}]/\frac{P_T}{P_0}[-]$
760	2340	3.0 / 12.82×10^{-4}	0.115 / 4.91×10^{-5}
935	1270	1.4 / 11.02×10^{-4}	0.048 / 3.78×10^{-5}

6.2.5 Time-resolved measurements

To identify the optical properties of the tissue phantom and to get a verification of the highly scattering properties of the lung, time-resolved measurements were made. In the measurements on the tissue phantom two optical fibres were placed parallel to each other with one emitting light and one working as a detector. Two measurements were made, one with 760 nm and one with 935 nm light. Similar procedures were done on the lung but with the two fibres opposite to each other and with the lung in between. These measurements were made at position A and B; see Sect. 6.2.2. Optical properties of the lung could also be calculated if the distance between the fibres was fixed but in these measurements they were hand held and not particularly accurately.

The measured optical properties of the tissue phantom are presented in the table below (the desired values were $\mu'_s = 7.1 \text{ cm}^{-1}$ and $\mu_a = 0.3 \text{ cm}^{-1}$ for 760 nm and $\mu'_s = 5.5 \text{ cm}^{-1}$ and $\mu_a = 0.3 \text{ cm}^{-1}$ for 935 nm).

Wavelength $\lambda[\text{nm}]$	Transport scattering coefficient $\mu'_s[\text{cm}^{-1}]$	Absorption coefficient $\mu_a[\text{cm}^{-1}]$
760	6.6	0.18
935	4.4	0.21

The mean times for the light to propagate through the lung tissue at position A and B for the two different wavelengths are presented in the table below.

Wavelength $\lambda[nm]$	Mean propagation time at position A $\langle t \rangle [ps]$	Mean propagation time at position B $\langle t \rangle [ps]$
760	590	544
935	616	558

The ratio between the propagation time for the oxygen laser and the water laser light was in position A equal to 0.96 and 0.97 in position B. By comparing the mean propagation times with the ones measured for human maxilaris [25] it is observed that although the light propagates through approximately a third of the distance in the sinuses the mean propagation time is only approximately half. This indicates high scattering of light in the lung. It is also observed that the signal ratio between the two lasers are smaller in the lungs.

The values of the optical properties of the tissue phantom are smaller than predicted and additional measurements will be made to identify where the fault is. It might be something wrong with the measurement, the evaluation of the data or the component concentrations of the phantom.

6.2.6 Discussion

By comparing the penetration depth with earlier measurements and simulations; see Sect. 6.1, it can be observed that they are approximately the same. However, the instrument can handle and detect absorption signals that are smaller than a thousandth of the initial output power. These facts indicate that the gas cavities reduce the penetration depth. Penetration through more than 3 cm of lung tissue with the current instrument is unlikely, so for the bigger neonates transmission measurements probably are not the method of choice but might be for the smaller ones. On the bigger neonates the reflection approach might instead be an option. Due to the elliptical shape of the thorax these measurement may be done at many different angles between the fibre probe and the detector and not only in the same direction. Other angles might increase the amount of light to the detector but still yielding a sufficient absorption signal. However, due to the shallow penetration, valuable information about the deeper parts of the lung is not acquired.

In the measurements we used a phantom that only simulates the muscle tissue while in a human body there are many other tissue types like bones, fat etc. in the thorax region that may effect the measurements. The boar lung may have had an unseen internal damage during the measurements that have effected the properties but during the inflation it could be observed that it expanded continuously which indicates that it was intact. In the measurements on the lung a certain pressure were applied to guarantee good connection for the fibre probe and the detector but on a neonate, that might need to be lowered. There might also be problems to place the detector between two ribs due to the size of the detector.

By studying the ratios between the oxygen and the water absorption signal we observe that the ratio is much larger in the reflection measurements than in the transmission cases. This could be because the light has a higher probability to scatter in an small angle from the initial propagation direction than in a

large. Then the fact that the light from the water laser has a higher probability to scatter than the light from the oxygen laser does not influence transmission measurements that much because it is mostly scattered towards the detector. However, in the reflection measurements the anisotropic scattering has a larger effect due to the fact that the light from the water laser can only penetrate a shallow depth in the lung or else it will be attenuated. The light from the oxygen laser can penetrate deeper because it is not attenuated to the same extent; see Fig. 6.11. The result is that the light from the oxygen laser goes through more gas than the light from the water laser. It could also be because we had a different temperature in these measurements. Even if we calculate with a temperature that makes the oxygen and the water absorption signal fit for the small distance the ratio in the measurements at a large distance still is very large.

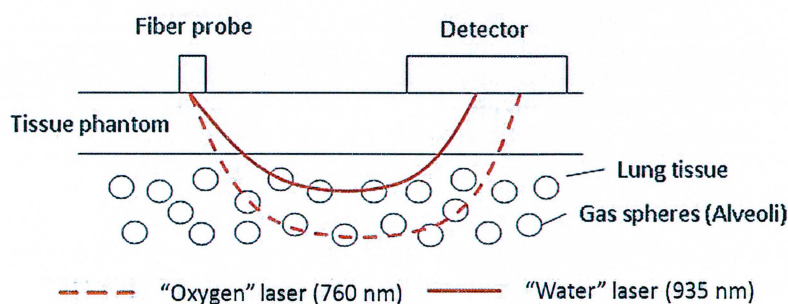


Figure 6.11: Different penetration depths for the oxygen and water laser may generate a higher ratio between the absorption signals in reflection measurements than in transmission measurements.

6.3 Aftermath of initial measurements on boar lung

A few question marks from the initial measurements on a boar lung need to be studied. These are the optical properties of the tissue phantom but also the ratio between the oxygen and water absorption at different separations between fibre probe and detector in reflection geometry.

6.3.1 Tissue phantom

In the initial measurements of the optical properties of the constructed tissue phantom the values of both the scattering and the absorption coefficient were too low. An additional phantom was made with the same recipe and the optical properties were measured with time of flight measurements. The optical properties obtained are presented in the table below (the desired values were $\mu'_s = 7.1 \text{ cm}^{-1}$ and $\mu_a = 0.3 \text{ cm}^{-1}$ for 760 nm and $\mu'_s = 5.5 \text{ cm}^{-1}$ and $\mu_a = 0.3 \text{ cm}^{-1}$ for 935 nm).

Wavelength λ [nm]	Transport scattering coefficient μ'_s [cm^{-1}]	Absorption coefficient μ_a [cm^{-1}]
760	6.42	0.31
935	5.4	0.40

These optical properties are more in line with those that should be obtained. This indicates that it was the time of flight measurements and evaluation that were a little off in the initial measurements. The absorption is very nice but the scattering is a little low but the optical properties are still acceptable.

6.3.2 Ratio difference in path length in reflection geometry

To study the ratio between the path length in a gas in reflection geometry for 760 nm and 935 nm light, measurements on a sponge with a tissue phantom were made. The sponge was an ordinary face scrub sponge that is sold in most stores with skin products. To give it additional properties similar to tissue it was wetted with water. The tissue phantom was done with the same recipe as the ones baked in the initial measurements; see Sect. 6.2.3. The measurements were made in four positions from A to D with increasing separation. The separation increased with a half detector width every new position; see Fig. 6.12. The separation between the probe and the edge of the detector in position A was 10 mm, in position B 20 mm, in position C 30 mm and position D 40 mm.

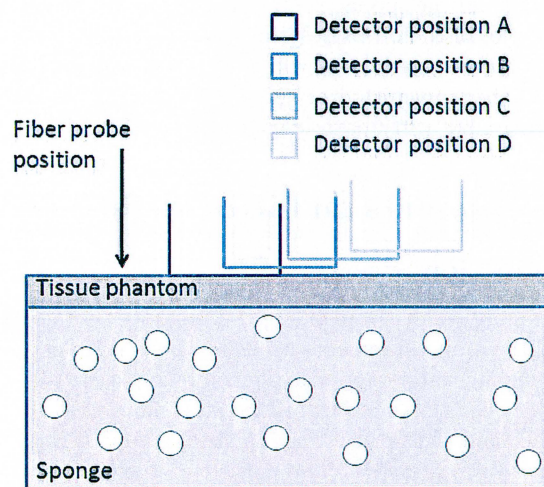


Figure 6.12: The geometry for reflection measurements on a sponge with a layer tissue phantom. Measurements were done with four different detector position labeled A - D with increasing distance from the fibre probe.

The absorption signals from oxygen and water vapour and the ratio between these are presented in Fig. 6.13. In the figure the ratio of the power transmittance between the oxygen and water laser are also presented.

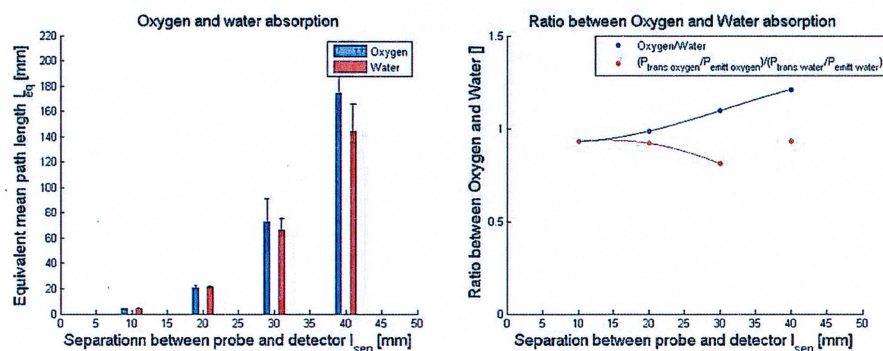


Figure 6.13: The results from the reflection measurements on the sponge with a tissue phantom layer above. The oxygen and water absorption signals for different distances between fibre probe and detector are presented to the left and the ratio between these values together with the ratio of the transmitted power normalized with the emitted between oxygen and water vapour to the right.

It can clearly be observed that the absorption signal increases with the separation distance but also the ratio. However, the ratio is smaller than the one detected in the initial measurements on the boar lung but the differences between the real lung and the sponge is quite large, both in optical properties and in pore size. The plot of the ratios describes that the ratio of the absorption signals increases for higher separations while the ratio in output power decreases. Using the ratio of the transmitted power might be a way to calculate the ratio between the oxygen and water path length in a simple way.

6.4 Measurements on nitrogen flushed boar lung

6.4.1 Introduction

With the encouraging results from the initial measurements on the model with a boar lung, additional measurements needed to be done to get additional verification that oxygen and water vapour really could be measured inside a geometry similar to a child. Additional issues are if one could detect dynamic processes such as breathing and if the best way to measure on a lung *in vivo* was to use a curved or a flat geometry. The curved geometry was along the ribs in a horizontal orientation and the flat geometry was across the ribs in a vertical orientation. Preceding this experiments a visit to Doc. Lars Björklund of the Neonatal Department had been done with the purpose to obtain realistic sizes of the neonates. Two sizes were chosen, one of a premature with weight 1 kg and one of a fully grown child that weighed 3 kg. The ones weighing 1 kg have about 6 mm of tissue outside the lung and the 3 kg has about 12 mm. However, the thickness of the tissue varies from child to child depending on how swollen it is. Most measurements were done on the 1 kg size model because these children are more probable to need the help the GASMAS technique can provide. An additional boar lung simulated the lung and new gelatine based tissue phantoms

with the same optical properties as those in Sect. 6.2 simulated the surrounding tissue. All measurements performed in this experiment are done in a reflection geometry due to the fact that the chosen sizes of the babies are too large to do transmission measurements on. A curved geometry is used in the measurement if nothing else is stated. Two lungs from different boars were used in the measurements.

The breathing was simulated by flushing the lung with compressed air and nitrogen. First, only air then only nitrogen and then air again and so on in several cycles.

The boar lungs used in this experiment were again provided by the slaughterhouse Skånska Vilt in Vinslöv, Skåne and the boars were shot and prepared in the morning the same day when the lungs were collected, February 22, 2010. During the transport of the lungs they were placed in a plastic bag in a icebox with snow inside.

The measurements done on the breathing simulations were performed with 50 averages and thus one every ten seconds while in the stationary measurements 100 averages were used.

The problem with the uncertainty of the temperature of the gas was still a problem but additional efforts were put in and the temperature of lung tissue was measured to 17°C. However, the temperature is still a problem because it may differ from the temperature of the gas but it can be assumed that after flushing the lung for a while the temperature of the gas and the lung is similar.

6.4.2 Breathing simulation

To study the potential to detect dynamic processes and to verify that it is the gas within the lung that we measure, the following measurements were performed. The initial thought was that the absorption signal from oxygen should disappear entirely when flushing with nitrogen and would reappear when flushing with air. The water vapour absorption should be constant over time. The altering between the gases was done by combining flows from a nitrogen tube and a compressed air source to the hose that was inserted into the lung and adding switches to both flows; see Fig. 6.14. By opening one switch and closing the other the desired gas could be obtained.

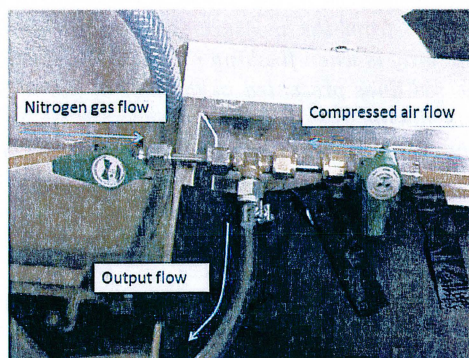


Figure 6.14: *Figure showing the gas mixing controls.*

There was however, a problem with the gas handling and that was that when altering between the gases it was hard to maintain a steady flow that resulted in the lung collapsing a bit before being expanded again. This made it difficult to do the measurements with the fibre probe and the detector placed by hand because they should have a constant separation during the entire measurements series. The solution was a construction that held both the probe and the detector at a fixed position. The separation between the probe and the detector were chosen to 20 mm. This was a proper distance because the light can penetrate into the lung and give rise to an acceptable absorption signal, and at the same time we have sufficient light through to the detector that carries the absorption signal. The measurements were done in reflection geometry on the model of a 1 kg child, with the tissue outside the lung being 6 mm thick. Initially, the lung was filled with compressed air and after 60 seconds the gas was altered to nitrogen for 60 seconds and then back again. The switching back and forth was done four times and at the end the flushing of nitrogen continued during 120 seconds more to study if the 60 seconds were not enough for the nitrogen to disperse and the absorption signal to decay. During every ten seconds a measurement was done.

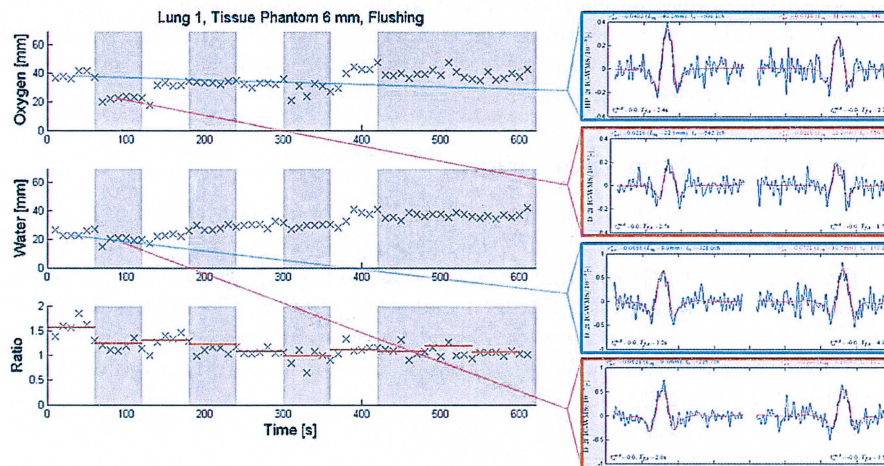


Figure 6.15: *The results from the measurements on the breathing simulation. The area marked with gray is when flushing nitrogen and the white when flushing compressed air. The red lines presented in the plot of the ratio is a mean value of the measurements during the flushing sections. The measurements taken simultaneously as the gas is switched is excluded from this mean value.*

The gas absorption from oxygen and water vapour are presented in Fig. 6.15 together with the ratio between the two gases. As can be observed the actual result did not correspond to the desired outcome. In the first cycle the decrease in absorption can be observed both in the oxygen and water vapour signal when flushing with nitrogen. The decrease for the oxygen is larger and thus the ratio is decreased. The decrease of water vapour absorption is probably not due to the fact that the water vapour are flushed away but rather that when the lung is inflated again the probe and the detector is placed at a different spot on the

lung with less trapped gas. This is a nice feature of the instrument because the ratio is independent of the interrogation area being changed and thus it is only changes in the gas within the tissue that effects the measurement. After the first cycle the variations in the ratio are not sufficient to ascertain if it is air or nitrogen that is being flushed.

6.4.3 Curved or flat geometry?

These measurements had the purpose to study in what way to do future measurements on a thorax in order to have the best results. With the best result we mean a large absorption signal with a sufficient amount of transmitted light. The different geometries were simulated by doing measurements on different directions along the lung; see Fig. 6.16.



Figure 6.16: *The measurements orientations to obtain a curved and a flat geometry.*

Measurements were done with altering distances between the fibre probe and the detector from 5 mm and 30 mm, with 5 mm steps. Three measurements were done at every distance. In these measurements the model of a 1 kg child was used. The lung was flushed by compressed air.

The results from these measurements are presented in Fig. 6.17. With increasing separation between the probe and the detector the integration depth increases and thus more gas is being probed. This is easily observed in the result but something out of the ordinary happens at 25 mm separation for the flat geometry. The high value might be due to large gas cavities at precisely the depth where the majority of the light penetrates. Both the oxygen and the water vapour signal increases, supporting such an explanation. The value of the absorption signals are similar between the two different geometries. The ratios are also similar for the different geometries and has a value of about 2. However, the ratio is dependent on the temperature and its uncertainty transmits an uncertainty to the water absorption values.

of curvatures more similar to children, a smaller animal lung is to be found. When studying the ratio in these measurements and comparing the results with the ratio for the reflection measurements in the previous experiment; see Sect. 6.2, a difference is observed. In the latter measurements the ratio is almost constant while the previous measurements indicate that the ratio should increase in reflection measurements.

The results for the different positions and lungs in the curved geometry are due to the distribution of gas within a lung not being uniform and thus different gas absorption should be detected at different places. However, the absorption from the gases are smaller in the second lung and that might be a coincidence but may also be because the second was more wet during the measurements due to fact that it had not been measured on before. Thus the penetration depth was decreased and with it the amount of penetrated gas.

6.5 The pursuit of zero signal in measurements on boar lung

6.5.1 Introduction

The somewhat discouraging results from the measurements discussed in Sect. 6.4 in aspect of the fact that a zero oxygen signal was not measured when flushing with nitrogen motivated additional measurements. These were focused to get the absorption signal down to zero and if this could not be done to understand where the absorption came from. The measurements also had the purpose to increase the statistics of the measurements. The size of a 1 kg and a 3 kg neonate were used when dimensioning the model. The tissue phantom created to simulate the tissue surrounding the lung had the thickness of 7 mm for the smaller child and 14 mm for the bigger. These thicknesses do not correlate with the ones used in the measurements in Sect. 6.4 but because of the variation of the sizes of real children the difference was acceptable. It is also a geometry that was harder to do measurements on, so if it was successful in this it must work in a thinner model.

The measurements are of the reflection type and are done in a curved geometry. During some of the measurements, nitrogen was used to flush the lung to remove the oxygen, the nitrogen is provided to the lung in a similar way as discussed in Sect. 6.4.

The slaughter house Skånska Vilt in Vinslöv, Skåne provided the lung and the boar was shoot and prepared in the morning the same day that the lung was collected, February 24, 2010. An ice box with snow inside and a plastic bag were used to preserve the lung during the transport.

50 averages were done for the measurements and the lung tissues temperature was measured to 17.5°C. When measuring on the lung filled with compressed air, 15 measurements were done.

6.5.2 Zero signal

The measurements were performed with alteration of separation of the probe and the detector from 15 mm to 30 mm with steps of 5 mm. For every step measurement were done when the lung was filled with compressed air and when

it was filled with nitrogen. The difference from earlier measurements were that before switching gas the lung was mechanically compressed by squeezing it in the hand. Then it was filled again with the desired gas. When measuring on the lung filled with compressed air 15 measurements were done at each step and three when it was filled with nitrogen. These measurements were done with a 7 mm thick tissue phantom. Similar measurements were done when using a 14 mm and no phantom at all but in these measurements only compressed air was used to flush the lung. The planned measurements with a separation of 30 mm and a 14 mm thick tissue phantom did not yield sufficient light throughput and thus were never performed.

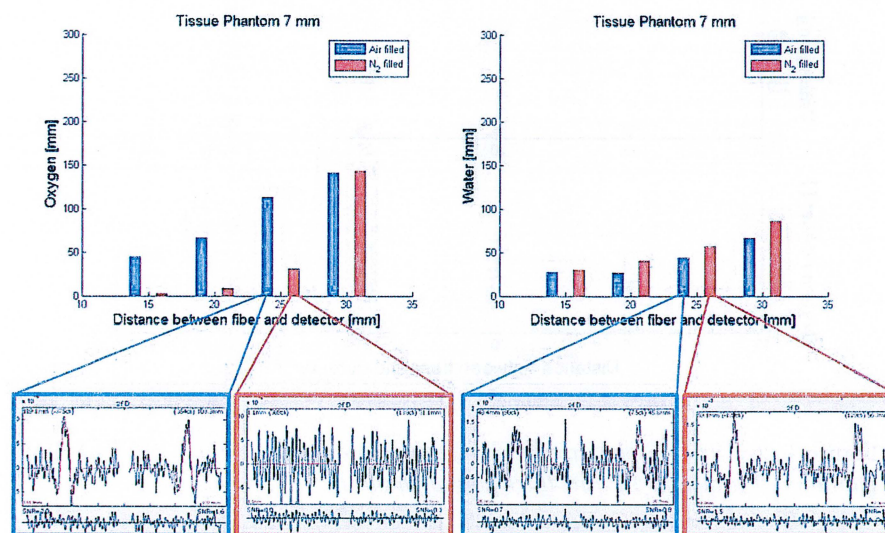


Figure 6.19: The results from the measurements on the lung with a 7 mm thick tissue phantom both when flushing air and when flushing nitrogen. Each stack is a the mean value of 15 measurements when flushing with air and three when flushing with nitrogen. Below the stack diagrams examples of WMS signals for measurements with a 25 mm separation between fibre probe and the detector are presented. One WMS signal from the oxygen absorption when flushing compressed air and one when flushing nitrogen are presented to the left and similar to the right but for water vapour absorption instead.

The very nice results from the measurements on the model with the 7 mm thick tissue phantom are presented in Fig. 6.19. It can be observed that the oxygen absorption signal is reduced to zero when flushing nitrogen and an absorption is measured only due to the fact that the signal fitting is done on the noise. When increasing the separation the detected light is decreased and the noise increased and thus the "detected" absorption when flushing nitrogen is increased. An unexpected observation is that the water vapour absorption signal is larger when flushing nitrogen than when flushing compressed air. The explanation might be that compressed air pushes away water vapour more than nitrogen does. It might also be that the pressure of the flushing is different for

the two flows which results in that the lung is distended differently, i.e. the geometry is different.

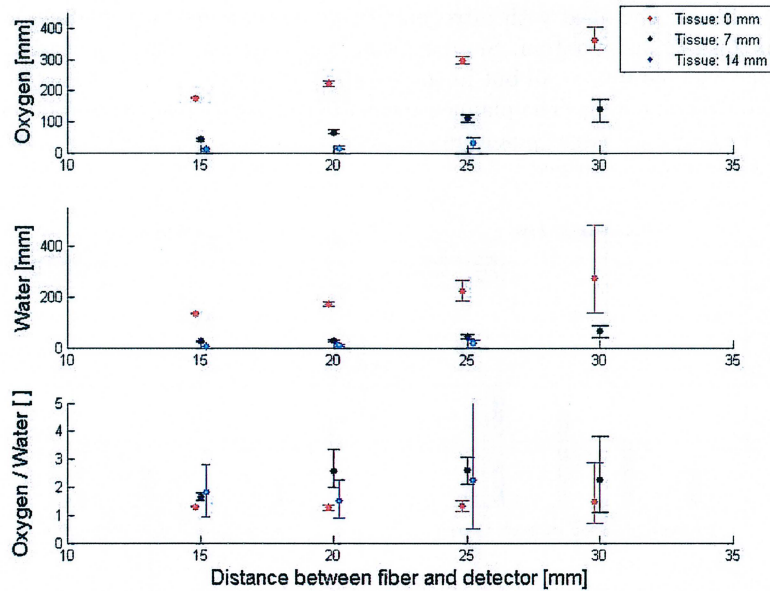


Figure 6.20: The results from the measurements on the lung with no tissue phantom, 7 mm and 14 mm thick tissue phantom.

The results from all the measurements with no phantom, 7 mm phantom and 14 mm phantom are presented in Fig. 6.20 with the oxygen and water vapour absorption and the ratio between these quantities. As could be expected the absorption signals are larger with less tissue phantom and the standard deviation is larger for more difficult measurement geometries. More difficult here means less light through related to larger separation and thicker tissue phantom. This is true for all instances except for the water vapour absorption at a separation of 30 mm.

6.5.3 Discussion

The result that the absorption from oxygen became zero when flushing with nitrogen verifies that what is measured is the gas within the lung and the instrument does not give any offset absorption. The problem with noise is, however, a limitation when it comes to difficult measurement geometries. The fact that the oxygen absorption signal went down to zero when the lung was mechanically compressed shows the importance of the diaphragm muscle that mechanically presses the lung together when we breathe. It also illustrates the importance of giving ventilation help when muscle relaxers during an anesthesia. As observed in Fig. 6.19 the noise is substantial. One might still find the absorption signal within the large noise but it is on the limit on what can be measured. The limit

is decreased if the surrounding tissue is thickened and for a 3 kg child no more than 20 mm separation between the probe and the detector would probably give a recognizable signal. This decreases the penetration depth so the solution for this case is to increase the power of the lasers or move to other wavelengths that penetrate deeper. For a 1 kg child the situation is brighter. Here maybe not 30 mm separation can be used but at least 25 mm.

6.6 Measurement on human lung in vivo

Measurements have been made *in vivo* on several adult lungs and on a 2.5 year old child. The adult lungs belonged to healthy volunteers e.g. colleges, friends and the author. The measurements have been focused to three different areas. These were on top of the chest, between approximately the eighth and the ninth rib down on the side and below the armpit on the right hand side; see Fig. 6.21. The latter were specially interesting due to the lack of muscles here. Pectoralis major and the back muscles creates a v-shape below the armpit and within the v there are no muscles until the ribcage and the serratus anterior muscles. The right side is specially interesting because the lung is closer to the ribcage here than on the left hand side because of the fact that one more lobe need to fit on the right side. In neither of the measurements an absorption signal could be detected. The reason for this is that the tissue outside the lung is too thick even for the 2.5 year old child. The light can not reach the lung and make it back again. All these measurements were done in reflection.

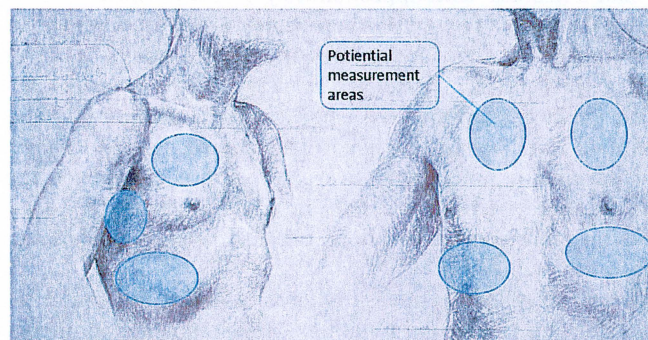


Figure 6.21: Three potential areas where measurements on a human lung can be done. On top of the chest, between approximately the eighth and the ninth rib and below the armpit and above the V-shape created by the pectoralis major and the back muscles.

Chapter 7

Discussion

The initial measurements on the boar lung (Sect. 6.2) shows that absorption signals can be obtained in geometries similar to those relevant for neonates. The produced tissue phantoms for these measurements were thicker than the tissue surrounding the lungs for a 1 kg neonate. The measurements also show that both transmission and reflection measurement could be possible on neonates. The reflection measurements will be possible on all sizes as long as the tissue outside the lung is not too thick while the transmission measurement would only work on the very small children. However, transmission measurements are more difficult than first was thought. From later visit to the Neonatal Department it was learned that a neonate with approximately 6 - 7 mm thick tissue outside the lung has a lung thickness of about 4 - 5 cm which is thicker than the model used in the measurements. In addition, studies of the influence of small gas cavities within a volume, presented in Appendix B, shows that it is harder to penetrate a sample with small gas cavities than one without. Combining these results with the simulated and measured penetration depth one can easily convince oneself that transmission measurements are very limited. However, the fact that the neonates are more transparent than an adult might do wonders but until measurements on real neonates are done one has to assume that transmission measurements are not possible.

The limit for the reflection measurements is not really found yet but the measurements done on the second lung, i.e. "Measurements on nitrogen flushed boar lung", shows that geometries similar to a fully grown neonate can be measured on. The tissue thickness on such babies is about 12 - 14 mm. However, in these measurements it can be observed that the limit is being approached. These results are measured with the current 760/935 nm instrument and it might be that an upgraded 760/935 nm instrument with better fibre solution, where not so much of the power is lost in the fibres, will push the limit further. The 760/820 nm instrument will have very good potential to take the instrument to even thicker geometries as well, both due to the fact that the light will penetrate deeper and that a better fibre solution could give a higher output power.

However, the penetration depth problem has two sides, not only does the light need to penetrate the tissue deeper but also longer. Experience tells that the main part of the detected light penetrates about a third of the distance between source and detector. This means that to penetrate deeper the distance between detector and source must be increased and this results in additional

tissue that needs to be penetrated. The penetration issue can be improved by not measuring on a flat geometry but on a more curved one because then the light will not have as long path to resurface again and to be detected; see Fig. 7.1. The results become something in between transmission and reflection measurements but then the problem with the difficult penetration of geometries with small gas spheres might be a problem.

As indicated before the tools to achieve deeper penetration are higher laser power or "better" wavelength with more favorable optical properties of the tissue. If one were to increase to power, more light will be detected - both light that has penetrated down to the gas and carries absorption signal and light that does not penetrate as deep. This will probably be especially prominent in difficult geometries where one has to decrease the distance between source and detector because then the majority of the light does not reach the gas but only a little light. The increase in intensity might complicate the evaluation of the signal because the intensity normalization must be done with a higher value. Hopefully, this will be handled by the evaluation method but it might increase the noise.

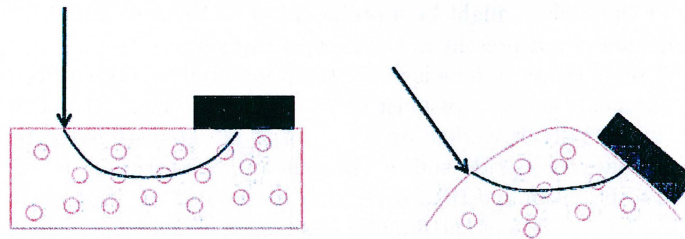


Figure 7.1: *There might be an advantage with measuring in a curved geometry due to the decrease in path length needed by the light to resurface to the detector again. The increased attenuation due to the small gas spheres might overshadow these gains.*

From the different measurements on the three lungs it is observed that the measured absorption strength varies from time to time. The differences might be due to varying quality and freshness of the lung, but it is also dependent on the interrogation volume and how big a fraction of the lung is gas. In the real measurement case on the neonates the situation will be similar. Thus, one cannot look at the absorption signal itself but rather the ratio between oxygen and water vapour absorption. The problem with this is that the ratio is dependent on many things, the concentration of the gases, the difference in path length and the angle between the probe and the detector. The concentration of water is directly dependent on the temperature and the relative humidity. However, these parameters can be assumed to 37 °C and 100 %. The oxygen concentration is dependent on the function of the lung and when in the cycle of inhalation or exhalation one measure. From most measurement it can be shown that the ratio increases when the separation between probe and detector increases and the increase in ratio is due to the difference in path length for the different laser wavelength. The effect will probably be smaller with the 760/820 nm instrument than the 760/935 nm instrument. A way to measure

the ratio between the oxygen and water vapour absorption signal due to path length is to convert it from the ratio of the transmitted power percentage for the different wavelengths. The influence of the angle between probe and detector is based on the path length difference and could probably be included when the ratio of transmitted power is used. The path length is dependent on the optical properties and if something differs from the ordinary in the tissue the path length will change but even this will be accounted for by the ratio in transmitted power.

The problem with the ratio can be simplified by not measuring the absolute value but instead monitoring the changes in absorption signal when measuring on a fixed position. This is especially true when the influence of treatment is of interest (e.g. "before" and "after" a treatment).

The obtained zero absorption signal when flushing with nitrogen in "The pursuit of zeros signal in measurements on boar lung" indicates that the measured gas absorption comes from within the lung. Light can wander along the surface of the sample and yield a false absorption fraction. An advantage with transmission measurements is that the probability for the light to wander all the way around the sample is very low. However, for reflection measurements the wandering at the surface might be a problem but as the zero signal indicates it is a problem that is not present in the present measurements.

A limitation of the technique is in the temporal domain. To reduce the noise many measurements and sweeps must be made and averaged over. The number of averages is naturally dependent on the absorption signal strength. If the SNR ratio is large fewer sweeps do suffice. In difficult geometries about a hundred sweeps need to be taken and this correspond to about 20 s. In this work, when the signal has been sufficient the number of sweeps and averaging time has been decreased to half. It might be reduced even more but for the monitoring of neonates lungs purpose a measurement every tenth second is good enough.

Chapter 8

Summary and outlook

8.1 Summary

It has been shown that GASMAS measurements can be used to detect oxygen and water vapour within a geometry similar to that of a premature neonate of 1 kg as well as that of a fully developed neonate of 3 kg. Both transmission and reflection measurements have been performed and it has been concluded that transmission measurements are very difficult to do. Due to the very small amount of light. However, it might work on the very early neonates of about 0.35 kg, but not guaranteed. Reflection measurements is the method to further develop. There are problems with reflection measurements, such as more prominent differences in path length depending on wavelength that must be solved.

The absorption signals can be guaranteed to come from within the lung sample because a zero signal is obtained when flushing with nitrogen. Otherwise when the lung is flushed with air variations in absorption signal are obtained when measuring at different positions. This is natural but it indicates that only measuring oxygen might not give useful information but water vapour must also be measured for normalization. It will be the ratio between these quantities that will be of interest.

In measurements on older persons, one 2.5 years old and a couple of about ten times as old, no absorption signals have been observed. The tissue outside the lung is too thick for the light to penetrate down to the gas and back out the skin again.

Using a 820 nm laser instead of a 935 nm laser to detect water vapour has many advantages such as smaller difference in path length compared to the oxygen laser at 760 nm. It is also easier to find fibres that fit to both the oxygen and water laser. The penetration depth of the 820 nm laser is also deeper. The one thing speaking against it is that the water vapour absorption lines are weaker but they are still sufficient.

8.2 Outlook

The next step in the pursuit of developing a GASMAS-based monitoring equipment is to build a more compact instrument that can be taken into a clinical

environment and to do measurements on real children and neonates. The current instrument is distributed on a table, but this is no problem when doing measurements on the sinus cavities on adults but on small already fragile neonates the instrument needs to thoroughly be disinfected between patients and transports. The idea is to have a box where all equipment is placed inside with only the fibre, the fibre probe, the detector and a cable to a DAQ- card extending to the outside. The box is only controlled by the DAQ- card and a LabView based program. Due to the potential of the 760/820 nm instrument the box should be based on this. A solution for the placement of the detector and the probe must also be developed, maybe not in the initial measurements on real neonates but in the finished equipment. Due to movement of the children the light emission and detector probes should be placed directly on the thorax. The neonate skin is very fragile so the sticking issue must be carefully solved. Maybe a fibre based instrument is not the best solution but instead having the lasers within a larger type of probe with both the lasers and the detector within it. Larger output power and better detection wavelengths are two things that need to be strived for.

Additional measurements on the ratio between oxygen and water vapour absorption in reflection geometry also need to be done to really understand which parameters are of importance. Later on, measurements with many patients need to be done to verify that the monitoring technique works.

A dream is to develop the instrument and the technique so far that measurements could be done on adults, but new smart solutions need to be developed.

For the GASMAS technique in general there are many applications that can be very interesting for future studies. One interesting possibility is studying effects on the broadening in the absorption line due to interactions between the molecules and the walls in nano-porous materials. Another more application oriented possibility is to measure the pressure and temperature of gases trapped in scattering media.

Chapter 9

Acknowledgments

During this work a collaboration with the Neonatal Department at SUS (Skånes Universitetssjukhus) in Lund has been of outmost importance to provide the medical view of the issues discussed in this thesis. Here Prof. Vineta Fellman and Doc. Lars Björklund are to be acknowledged for being an open contact into the world of medicine.

I would like to acknowledge my supervisor Prof. Sune Svanberg, for being a unyielding source of inspiration and information, and for taking me in under his wings. He is like a storm of inspiration that sweeps you off your feet. But most of all for being a role model in openness and hospitality. I felt seen and important from the very first instance.

I am very grateful to: my close supervisor and colleague Märta Lewander for teaching me about many things both work related and personal. She was the framework that held everything on ground when Sune's winds of inspiration were blowing too hard.

Prof. Katarina Svanberg for has been a source for medical advice when needed. She has also provided much to the hospitality and kindness that have governed the work environment that I have been working in.

Close collaboration has been made with the Medical Optics Group and I want to especially acknowledge two persons in this group: Erik Alerstam for providing the time-resolved measurements and for being a constant source of fruitful discussions, and to Can Xu for teaching me how to make tissue phantoms.

To little Ville Krite and his mother Emilie Krite Svanberg for participating in some exploratory tests.

Further, I am very grateful to: the Applied Spectroscopy and Remote Sensing Group for never hesitating in lending a hand when needed and creating a helpful working environment.

The Atomic Physics Division for providing a good foundation for research and personal development.

My family and girlfriend Emelie Ekblad for always encouraging me to go on and for bearing with me when I have been a bit touchy in times of stress and a lot of work.

This work was supported by the Swedish Research Council through a direct grant and a Linneaus grant to the Lund Laser Centre, and by the Lund University Medical Faculty. The kind collaboration with Skånska Vilt in providing

lung samples is gratefully acknowledged.

Bibliography

- [1] M Sjöholm, G Somesfalean, J Alnis, S Andersson-Engels, and S Svanberg. Analysis of gas dispersed in scattering media. *Optics Letters*, 26:16–18, 2001.
- [2] L Persson, K Svanberg, and S Svanberg. On the potential of human sinus cavity diagnostics using diode laser gas spectroscopy. *Applied physics B: Lasers and Optics*, 82(2):313–317, 2006.
- [3] The Express Group. Incidence of and risk factors for neonatal morbidity after active perinatal care: Extremely preterm infants study in sweden. *Acta Paediatrica*, 2010.
- [4] M Blennow, U Ewald, T Fritz, P-A Holmgren, A Jeppsson, E Lindberg, A Lundqvist, S N Lindeberg, E Olhager, I Ostlund, M Simic, G Sjöers, L Stigson, V Fellman, L Hellstrom-Westas, M Norman, M Westgren, G Holmstrom, R Laurini, K Stjernqvist, K Kallen, H Lagercrantz, K Marsal, F Serenius, M Wennergren, T Nilstun, P O Olausson, B Stromberg, and Express Group. One-year survival of extremely preterm infants after active perinatal care in sweden. *Journal of the American Medical Association*, 301(21):2225–2233, 2009.
- [5] J Ingimarsson, L J Björklund, T Curstedt, S Gudmundsson, A Larsson, B Robertson, and O Werner. Incomplete protection by prophylactic surfactant against the adverse effects of large lung inflations at birth in immature lambs. *Intensive Care Medicine*, 30(7):1446–1453, 2004.
- [6] M B van Veenendaal, M Miedema, F H C de Jongh, J H van der Lee, I Frerichs, and A H van Kaam. Effect of closed endotracheal suction in high-frequency ventilated premature infants measured with electrical impedance tomography. *Intensive Care Medicine*, 35(12):2130–2134, 2009.
- [7] C N Banwell and E M McCash. *Fundamentals of molecular spectroscopy, Fourth edition*. McGraw -Hill Book Company, 1994.
- [8] S Svanberg. *Atomic and Molecular Spectroscopy*. Springer, 2004.
- [9] L S Rothman, A Barbe, D C Benner, L R Brown, C Camy-Peyret, M R Carleer, K Chance, C Clerbaux, V Dana, V M Devi, A Fayt, J M Flaud, R R Gamache, A Goldman, D Jacquemart, K W Jucks, W J Lafferty, J Y Mandin, S T Massie, V Nemtchinov, D A Newnham, A Perrin, C P Rinsland, J Schroeder, K M Smith, M A H Smith, K Tang, R A Toth,

- J Vander Auwera, P Varanasi, and K Yoshino. The hitran molecular spectroscopic database: edition of 2000 including updates through 2001. *Journal of Quantitative Spectroscopy & Radiative Transfer*, 82(1-4):5-44, 2003.
- [10] P C D Hobbes. *Building Electro-Optical Systems*. Wiley Interscience, 2000.
- [11] F Träger. *Springer Handbook of Lasers and Optics*. Springer, 2007.
- [12] G Somesfalean, M Sjöholm, J Alnis, C af Klinteberg, S Andersson-Engels, and S Svanberg. Concentration measurement of gas embedded in scattering media by employing absorption and time-resolved laser spectroscopy. *Applied Optics*, 41(18):3538-3544, 2002.
- [13] L Persson, H Gao, M Sjöholm, and S Svanberg. Diode laser absorption spectroscopy for studies of gas exchange in fruits. *Optics and Lasers in Engineering*, 44(7):687-698, 2006.
- [14] J Alnis, B Anderson, M Sjöholm, G Somesfalean, and S Svanberg. Laser spectroscopy of free molecular oxygen dispersed in wood materials. *Applied physics B: Lasers and Optics*, 77(6 - 7):691-695, 2003.
- [15] L Persson, M Andersson, B Anderson, M Sjöholm, and S Svanberg. *Studies of Gas Exchange in Fruits Using Laser Spectroscopic Techniques*. In *proceedings of FRUTIC 05: Information and technology for sustainable fruit and vegetable production*. 2005.
- [16] M Andersson, L Persson, M Sjöholm, and S Svanberg. Spectroscopic studies of wood-drying processes. *Optics Express*, 14(8):3641-3653, 2006.
- [17] L Persson, F Andersson, M Andersson, and S Svanberg. Approach to optical interference fringes reduction in diode laser absorption spectroscopy. *Applied physics B: Lasers and Optics*, 87(3):523-530, 2007.
- [18] L Persson, M Andersson, M Cassel-Engquist, K Svanberg, and S Svanberg. Gas monitoring in human sinuses using tunable diode laser spectroscopy. *Journal of Biomedical Optics*, 12(5), 2007.
- [19] L Persson, M Andersson, T Svensson, M Cassel-Engquist, K Svanberg, and S Svanberg. Non-intrusive optical study of gas and its exchange in human maxillary sinuses - art. no. 662804. In *Diagnostic Optical Spectroscopy in Biomedicine IV*, 2007.
- [20] L Persson, E Kristensson, L Simonsson, and S Svanberg. Monte carlo simulations related to gas-based optical diagnosis of human sinusitis. *Journal of Biomedical Optics*, 12(5), 2007.
- [21] T Svensson, L Persson, M Andersson, S Svanberg, S Andersson-Engels, J Johansson, and S Folestad. Noninvasive characterization of pharmaceutical solids by diode laser oxygen spectroscopy. *Applied Spectroscopy*, 61(7):784-786, 2007.
- [22] T Svensson, M Andersson, L Rippe, S Svanberg, S Andersson-Engels, J Johansson, and S Folestad. Vcsl-based oxygen spectroscopy for structural analysis of pharmaceutical solids. *Applied Physics B: Lasers and Optics*, 90(2):345-354, 2008.

- [23] M Andersson, L Persson, T Svensson, and S Svanberg. Flexible lock-in detection system based on synchronized computer plug-in boards applied in sensitive gas spectroscopy. *Review of Scientific Instruments*, 78(11), 2007.
- [24] T Svensson, M Andersson, L Rippe, J Johansson, S Folestad, and S Andersson-Engels. High sensitivity gas spectroscopy of porous, highly scattering solids. *Optics Letters*, 33(1):80–82, 2008.
- [25] M Lewander, S Lindberg, T Svensson, R Siemund, K Svanberg, and S Svanberg. Clinical study assessing information of the maxillary and frontal sinuses using diode laser gas spectroscopy and correlating it with ct. *Manuscript in preparation*, 2010.
- [26] M Lewander, Z G Guan, T Svensson, S Svanberg, and A Olsson. Non intrusive measurements of food and packaging quality. In *Submitted*, 2010.
- [27] A J Welch and M J C van Germert. *Optical-Thermal response of Laser-irradiated tissue*. Plenum press, 1995.
- [28] J-L Boulnois. *Photophysical processes in recent medical laser developments: A review*. Springer London, 1986.
- [29] M Firbank, M Hiraoka, M Essenpreis, and D T Delpy. Measurements of the optical properties of the skull in the wavelength range 650-950 nm. *Physics in Medicine and Biology*, 38(4):503–510, 1993.
- [30] C R Simpson, M Kohl, M Essenpreis, and M Cope. Near-infrared optical properties of ex vivo human skin and subcutaneous tissues measured using the monte carlo inversion technique. *Physics in Medicine and Biology*, 43(9):2465–2478, 1998.
- [31] A N Bashkatov, E A Genina, V I Kochubey, and V V Tuchin. Optical properties of human skin, subcutaneous and mucous tissues in the wavelength range from 400 to 2000 nm. *Journal of Physics D: Applied Physics*, 38(15):2543–2555, 2005.
- [32] S A Prahl. *Light transport in tissue*. PhD Thesis University of Texas at Austin, 1988.
- [33] B E K Chan, D Sorg, M Protsenko, M O'Neil, A J Motamedi, and Welch. Effects of compression on soft tissue optical properties. *IEEE Journal of Quantum Electronics*, 2:943–50, 1996.
- [34] H Y Du, X H Cariveau, M Kalmus, and G W Lu. Optical properties of porcine skin dermis between 900 nm and 1500 nm. *Physics in Medicine and Biology*, 46:16781, 2001.
- [35] T L Troy and S N Thennadil. Optical properties of human skin in the near infrared wavelength range of 1000 to 2200 nm. *Journal of Biomedical Optics*, 6:16776, 2001.
- [36] T Svensson and C Abrahamsson. Time resolved spectroscopy - laboratory exercise. <http://www.atomic.physics.lu.se/fileadmin/atomfysik/Bio-photonics/Education/>, 2010.

- [37] K Prah and A J Welch. A monte carlo model of light propagation in tissue. *SPIE Institute Series*, 5:201, 1989.
- [38] G E Angus and W M Thurlbeck. Number of alveoli in the human lung. *Journal of Applied Physiology*, 32(4):483–485, 1993.
- [39] M Singh, R Singh, and D R Singh. Sagittal bands: Are they really sagittal? *The Internet Journal of Hand Surgery*, 2:1, 2008.
- [40] H Grey. *Henry Gray's Anatomy of the Human Body*. Bartleby, 2000.
- [41] M Lewander, Z Guan, K Svanberg, S Svanberg, and T Svensson. Clinical system for non-invasive in situ monitoring of gases in the human paranasal sinuses. *Optics Express*, 17(13):10849–10863, 2009.
- [42] J M Supplee, E A Whittaker, and W Lenth. Theoretical description of frequency-modulation and wavelength modulation spectroscopy. *Applied Optics*, 33(27):6294–6302, 1994.
- [43] M Sauren, R J McKenzie, and R L McIntosh. Determining the influence of adult skin thickness on compliance with radiofrequency exposure limits. In Kim, SI and Suh, TS, editor, *World Congress on Medical Physics and Biomedical Engineering 2006, Vol 14, Pts 1-6*. Springer-Verlag Berlin, 2007.
- [44] E Alerstam and S Andersson-Engels. Monte carlo simulations of light transport in tissue - computer exercise. <http://www.atomic.physics.lu.se/fileadmin/atomfysik/Biophotonics/Education/>, 2010.
- [45] B W Pogue and M S Patterson. Review of tissue simulating phantoms for optical spectroscopy, imaging and dosimetry. *Journal of Biomedical Optics*, 11(4), 2006.

Appendix A

Example of signal extraction code in MatLab

```
%Extraction of the WMS signal

%Reading the measurements
num = %imod1p75(3); filename
fs=400000; %sample speed
fm=9015; %Modulation frequency
N=length(num); %Numbers of sample points

%Time constants
tbegyn=0; %First time value
tsslut=N/fs; %Last time value
tsteg=(tsslut-tbegyn)/(N-1); %Time step size
t=0:tsteg:tsslut; %Creating the time vector

%Plot of the raw signal
figure(1)
plot(t,num)

%Calculation of the Fourier transform
F=-fft(num); %Doing the Fourier transform
f=fs/N*((-N/2):(N/2-1))'; %Making the frequency vector

%Plot of the Fourier transform
figure(2)
plot(f,F)
axis([-200000 -180000 -4000 4000])

%Shifting the signal to simplify the extraction of a harmonic
F=fftshift(F); %Shifts the signal

%Plot of the signal after shift
figure(3)
plot(f,F)
axis([0 20000 -4000 4000])

% Filtering the signal with a Super-gaussian window
df=500; %Width of window in Hz
nf=2; %Which harmonic to be extracted
Ffilt=F.*exp(-((f-nf*fm)/df).^8); %Applying the window

%Plot the filtered signal
figure(4)
plot(f,Ffilt)
axis([0 20000 -4000 4000])
```

Effects on light propagation due to geometric shapes

Gas spheres trapped in tissue

Anders Bruzelius & Jens Ålebring

ABSTRACT

The effects of small gas spheres trapped within a tissue phantom have been studied by three different techniques, GASMAS, TOF and MC-simulations. Three different parameters have been studied with these techniques, the total propagation time, the transmitted power and the path length through the gas spheres. We have shown that the effective scattering coefficient of a gelatin-based tissue phantom increase with the introduction of small air filled spheres with an average diameter of 180 μm while the absorption coefficient decreases. We have also shown that these alterations of the optical properties reduce the transmitted light to a detector proving that it is harder for light to penetrate a porous geometry. Finally we have shown that a gelatin-based tissue phantom has a potential to simulate a real lung but with further work to control the production of the density and size of the gas spheres and exactly how these affect the optical properties.

The measurements have been done on a geometry that resembles a small premature neonatal thorax. The purpose for this project is namely to take one step closer to the development of a GASMAS-based monitoring equipment for premature neonatals.

Introduction

The morbidity for premature neonatal is considerable in Sweden today [1] but have during later years steadily decreased [2]. It is important to keep pressing down these numbers and a prominent source for deaths is due to matters that concerns the lungs. This is because the lungs is the last thing that develops in a child and for premature neonatal these are not fully developed. On the inside of the small lung blisters, alveoli, a substance called surfactant is present and it works as a spring so the alveoli do not collapse during an exhale. If this substance not is entirely developed the alveoli might collapse and when it does the tissue will grow together leading to atelectasis, incomplete expansion of the alveoli, during later breaths. This will never repair and it leaves the child with a chronicle decrease in lung capacity. From this it can easily be understood that the treatment and monitoring of the premature neonatal is of biggest interest. To keep the alveoli opened a overpressure is applied to the lungs and air is continuously distributed. Many of today's monitoring methods are based on measuring the exhaled and inhaled air but these cannot give spatial information. X-rays might have provided this but it is not preferable to expose a child with ionizing radiation during a real time monitoring. There is a method that can give information about the expansion of the lungs and this uses electrodes to monitor impedance changes that correlate to volume changes [3]. However, the electrodes are placed directly on the skin and might damage it. The non-invasive technique GASMAS, Gas in scattering media absorption spectroscopy, can potentially be a powerful tool to both monitor the concentration of oxygen and relative volume changes. It might even have the potential to monitor the pressure of the gas. Initial measurements have been made on "real" models of children thoraxes constructed with a boar lung and a gelatin based tissue phantom [4]. The scattering of the phantom is obtained by mixing in titanium dioxide and the absorption from ink to fit the properties of an abdominal muscle [5,6]. The initial measurements show that GASMAS can measure oxygen and water vapor inside a model similar to a child's thorax. However, it is not really clear how the porous structure of the lung effects the lights propagation and thus studies must be made. It would also be nice to see if the boar lung can be exchanged with a porous gelatin based tissue phantom due to the limited availability of boar lungs.

Lights propagation through tissue is a very complex series of scattering events and eventually absorption. To describe and simulate this is important because to understand a how the light will behave before applying it to real tissue, so that no harm is caused. There are a few methods to this and these are Diffusion Theory [7], Monte Carlo simulations [8,9] and the Finite element method [10]. The diffusion theory requires a homogenous geometry and thus geometries with example many small gas spheres are not possible or hard to solve. There are limitations in the other two simulations methods as well. It is hard to describe a piece of tissue with a seemingly random distribution of small spheres with varying size. Hence, a simplification of the model in the simulations needs to be done. To verify that the simulation is accurate and to complement it one might do different experiments on a "real" model. Some examples of different experimental methods are Time of flight spectroscopy (TOFS) [11] and GASMAS [12].

This project will focus on three different parameters that may alter due to the gas spheres within the tissue phantom. The first parameter is the mean propagation time for light to travel through the sample and with it the effective optical parameters. "Does the effective scattering measured with TOFS

decrease or increase due to the spheres and do the effective absorption increase or decrease?" are questions that need to be answered. The second parameter is the transmitted power through the sample, "how much power is lost due to the spheres?". The third parameter is how much time and distance the light have traveled through the gas spheres. "How much of the lights total propagation time is spent within the spheres and how this correlate with the porosity?" In the initial measurements transmission measurements has been done with geometries similar to the one in this project but based on a boar lung. If the results from this project measurements correlate with the ones obtained from initial measurements it could indicate if the gelatin based lung phantom can replace the boar lung.

Initially the different techniques and methods will briefly be explained and then will the measurements done be presented. After that the results will be discussed separately for each measurement and then all of them together. Finally a summarization will be done.

Techniques and Methods

Baking a tissue phantom

The gelatin based tissue phantom is a good and handy way to simulate tissue. It is even good when modeling for acoustic measurements [13]. The nice features with it are that it is easy to build and the optical properties can be determined only by the concentration of the components. To get the scattering coefficient titanium dioxide, what makes white paint white, is mixed in the phantom. The absorption coefficient is obtained by ordinary black pen ink. The titanium dioxide has approximately the same wavelength dependence as tissue but the ink is black and has an even distribution over many wavelengths. Some tissue types have the same property at selected intervals but far from all. In this project we uses the optical properties of a abdominal muscle which has this property in wavelengths area between 760 nm and 950 nm [6]; see Figure 1.

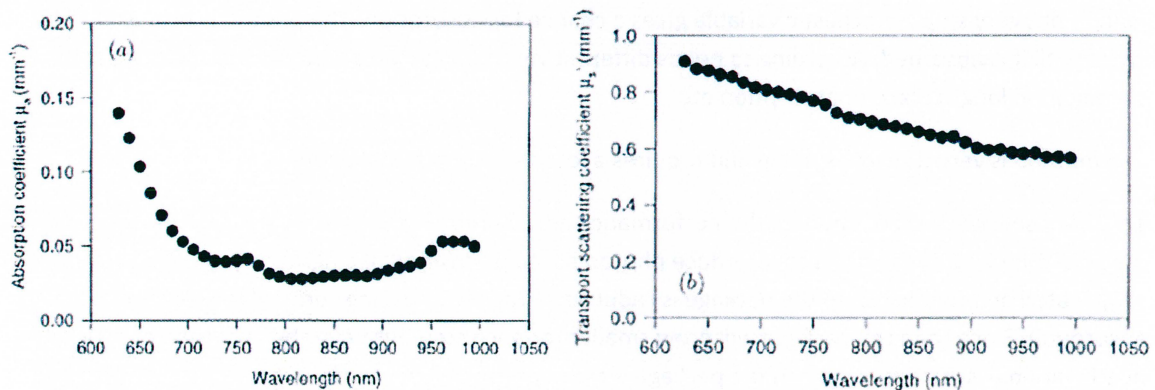


Figure 1 The optical properties of a human abdominal muscle. The absorption coefficient to the left and the scattering to the right depending on wavelength [6].

The way to make or bake whatever one prefers is simple. First 500 ml water and 50 g gelatin is mixed together and heated up in an oven as to dissolve the gelatin in the water. When the mixture is transparent it is removed from the oven and then 550 mg titanium dioxide and 1.5 ml ink is added [5].

The solution is then stirred to facilitate the mixing of the components. After the mixing is done the solution is poured into a container where it can cool down and solidify. In this project three models were to be measured on; Model A were a 24 mm thick lung phantom and two 6 mm solid phantoms on either side; see Figure 2, Model B were only the lung and Model C a 24 mm thick solid phantom. To produce the lung phantom the tissue phantom solution was stirred as to produce foam on the top of the solution. This was gathered with a spoon and collected in a container until sufficient foam were collected to construct the lung phantom.



Figure 2 Model A is constructed by a 24 mm thick lung phantom and two 6 mm thick solid phantoms (left). Model B is only the lung phantom (right).

Monte Carlo simulation (MC)

Monte Carlo simulations are a stochastic way to estimating light transport in tissue. It is based on the idea that single photons are propagated one by one stepwise through the tissue. A photon is introduced and its direction and step length is calculated randomly according to tissue properties in that specific point. For every step a stochastic variable gives a chance for absorption. The photon is propagated in steps until it is absorbed. According to needs different variables can be saved for each photon, i.e. propagation length place of absorption etc.

The method is very time consuming and requires a lot of computational power.

There are several ways to improve the performance and thereby reduce the computational time of the method. One way to do that is to introduce photon packages instead of single photons. These are propagated and for each step the package is reduced in intensity, leaving some of it behind as absorption. Since then the package will grow smaller for each step but never be absorbed completely a death variable is introduced when the package intensity goes below a certain threshold. This variable works as a Russian roulette giving the package a certain chance to survive. If it survives it is up scaled according to the probability for survival in order to achieve energy conservation.

To do Monte Carlo simulations for porous tissue, i.e. a lung, there is need for a way to model this porous tissue. In the version used here the porosity is modeled by introducing a matrix of identical spheres with different optical properties compared to the surrounding tissue so that the spheres have the same

properties as air. This results in a large number of surfaces at which scattering and refraction occurs. In the interior of the spheres the photons are not absorbed or scattered. This gives a possibility to estimate how long each photon propagates through spheres. For each step a check is performed whether the photon package has passed a bubble; if that is the case scattering or transmission is chosen according to random variables with certain probabilities. If the photon passes through a bubble the propagation length in this bubble is calculated. The total length each photon takes through these spheres is recorded.

Time of flight spectroscopy (TOF)

Time of flight spectroscopy is a method for investigating the optical properties of a diffuse material, i.e. tissue. The idea is that light is propagated through the tissue and the time it takes for the photons to pass through this tissue is measured. The system used works by the principle that flight time for one single photon at a time are measured and by doing this repeatedly a distribution of flight times is achieved.

Laser pulses with 40 MHz repetition rate are sent through the material. After passing through the tissue these pulses will be spread out in time. By greatly reducing their intensity with a variable neutral density filter at most one photon per pulse will reach the detector. This is needed because otherwise the first photon of the pulse will always trigger the detector and consequently no information about the time distribution of the pulses is recorded. By detecting one photon at a time a histogram of flight times for the photons are built from numerous pulses.

The flight times for the single photons are measured by charging a capacitor. The photon is detected using a photomultiplier tube.

The photon detection and a trigger pulse from the laser synchronized with the laser pulse is used to start and stop the "clock". The voltage over the capacitor after it has finished charging is measured and converted to the corresponding time of flight for the photon. The reason to use the photon detection as start instead of stop for the clock is due to the fact that for many pulses there will be no photon at all entering the detector, the counter will then not stop until it maxes out and it will take a long time to uncharged the capacitor so it can be used again, this would reduce the detection rate substantially and subsequently increase the needed detection time to get a good signal.

The system uses four lasers at different wavelengths in order to get a rough spectral resolution. These lasers are fired sequentially. The lasers are coupled together and brought to the sample using optical fibers; an optical fiber is also used for collecting the light after it has passed the tissue and bring it to the detector. It takes some time for the pulses to propagate through the fiber and also the electrical trigger signal from the laser has some delay. Therefore a measurement is taken when the illumination fiber and the detection fiber is directly connected to each other. Subtracting this reference from our measured time gives the flight time through the tissue.

The measured time of flight histogram is compared with a from theory calculated histogram using guessed reduced scattering and absorption coefficients. Using a measure for the error between guess

and measurements better guesses are made using an algorithm. This is repeated iteratively until a good fit is achieved. Exact values for the reduced scattering and absorption coefficients are hard to get since an increase in scattering changes the histogram in almost the same way as an increase in absorption; making it difficult to resolve these precisely.

Gas in scattering media absorption spectroscopy (GASMAS)

The GASMAS technique is a method to measure gases trapped within scattering medium e.g. tissue. Since 2001 when GASMAS first was published [12] by Sjöholm et al. it has developed both in technique and application sense. From measuring one gas at a time with big analog lock-in amplifiers to a system where two gases are measured simultaneously and all the signal treatment is done digitally [14]. The first clinical measurements were done by Persson et al. [15] in 2006. In the technique a diode laser is tuned over a absorption line for the interrogated gas.

The propagation in tissue is however hard to describe due to the scattering and the path length through gas is hard to know. Thus one does not know if the gas absorption comes from a long path length through gas or a high concentration of the gas. This is solved by using a second laser and assuming that the path length in gas is similar. The gas absorption can be separated from absorption from the tissue due to the fact that absorption profiles from liquids and solids is approximately ten thousand times wider than the ones from gases. By WMS, wavelength modulation spectroscopy, [16] the small absorption from the gases can be detected and separated by modulating with different wavelengths. The detected absorption from the trapped gases are compared with a absorption from a know distance e.g. one meter and the path length through gases are obtained. Water vapor is detected at 935 nm and Oxygen at 760 nm. The laser responsible for the 935 nm light is called the water laser and the one at 760 nm is called the oxygen laser.

Measurements and Results

Concerning the phantoms

To verify that the produced tissue phantom had the optical properties that were desired evaluation of TOF measurements were preformed. The TOF measurements were the ones done when studying the total propagation time and these will be presented in the following part. Only the properties at 786 nm and 916 nm are presented due to the fact that these wavelengths are similar as the ones that the GASMAS system uses (760 nm and 935 nm). The desired and actual properties for the solid phantom are presented in the Table 1 below.

	Desired μ_a [cm ⁻¹]	Actual μ_a [cm ⁻¹]	Desired μ'_s [cm ⁻¹]	Actual μ'_s [cm ⁻¹]
786 nm	0.3	0.31	7	6.42
916 nm	0.3	0.39	6	5.44

Table 1. Table over the desired and actual optical properties of the tissue phantom.

The optical properties of the lung phantom are presented in table 2.

	Actual μ_a [cm ⁻¹]	Actual μ'_s [cm ⁻¹]
786 nm	0.14	9.92
916 nm	0.14	8.40

Table 2. Table over the actual optical properties of the lung phantom.

These are very interesting results because it can be observed that the scattering increases due to the small spheres while the absorption decreases. The scattering is increased probably because there are many very small sphere that will act as scatterers and that there are many areas where the difference in refractive index is quite big ($n=1$ for air and $n=1.4$ for tissue). The latter increases the probability for total reflection prominently. The absorption is decreased because the light takes “short cuts” through the gas spheres and thus do not have as long path length in solid tissue as it would without the spheres.

In latter measurements Monte Carlo simulations are done and in these the optical properties are extracted from the ones above in Table 1. For these simulations the average pore size is needed and the radius was measured with a microscope to be approximately 180 μm . This is approximately twice as big as the alveolus in an adult human are [17]. The porosity of the lung phantom was measured with help of Archimedes and his principle. The weight and volume were measured for both the lung phantom and the solid phantom. The porosity was measured to 43 %.

Total propagation time

To study the average time for photons to propagate through the three different tissue samples, i.e. lung phantom with solid phantoms, only lung phantom and a 24 mm thick solid phantom, time of flight measurements were performed. The measurements were done for four different wavelengths; 660nm, 786nm, 830nm and 916 nm. Results are presented in Table 3.

Phantom	660nm	786nm	830nm	916 nm
Solid	381	351	338	285
Lung	628	618	616	548
Both	806	776	759	635

Table 3 – Flight times [ps] in the three different tissue phantoms for the different wavelengths.

The purpose was to investigate how long time it takes for the light to pass through the porous tissue sample compared to the solid one. As discussed in the part above primarily two possible effects were likely to influence the transport time. The pores could allow the photons to take shortcuts through them and thereby avoiding being absorbed or scattered for relatively long distances. Also the changes in refractive index allowing the photons to be scattered and thereby prolonging the time it takes for them

to propagate through the tissue.

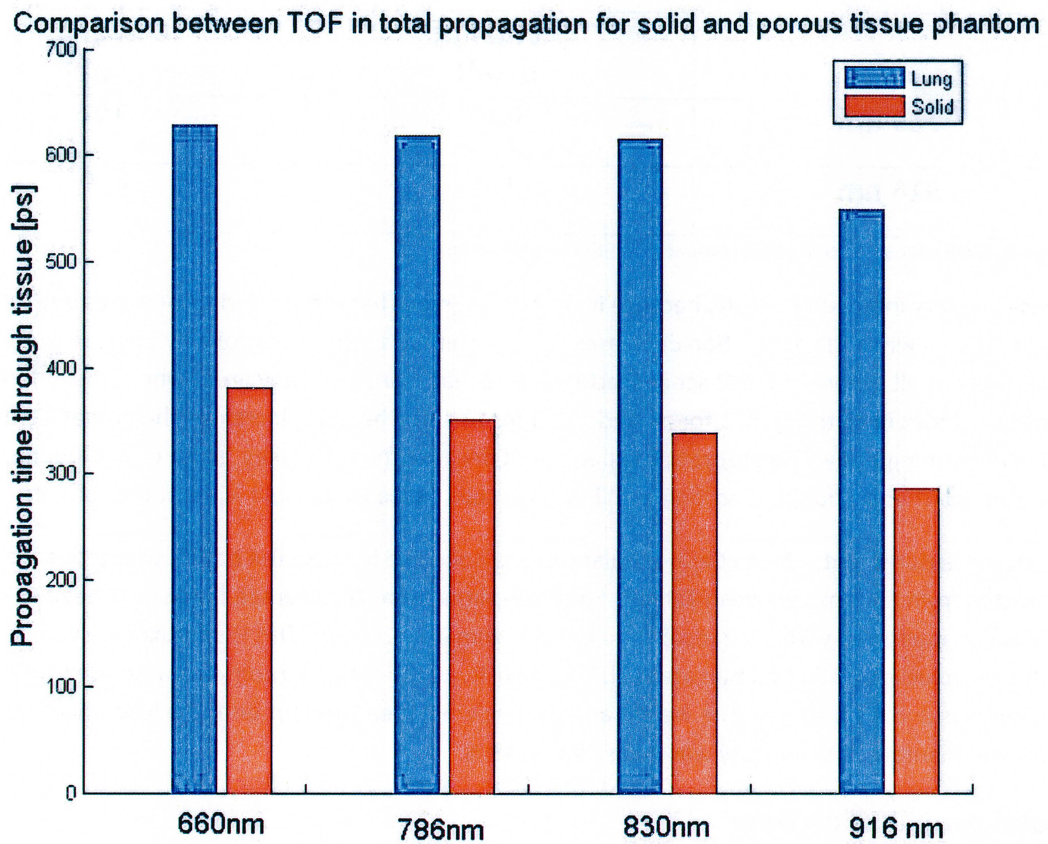


Figure 3 – Flight time in solid and porous phantom for different wavelengths

As seen in Figure 3 the flight time was greatly increased for the porous sample. The photons spent almost double the time in the porous one. This indicates that the effect of pores increasing the scattering is the dominating effect.

Also the flight times of the full sample, porous with solid top and bottom, were of interest when analyzing the GASMAS measurements. These measurements were also simulated using the Monte Carlo model described above. Results from the simulations can be seen in Table 2

Flight time	786 nm	916 nm
Total	801	683
In spheres	129	113

Table 4 -Flight times through the total phantom for 786 nm and 916 nm according to the Monte Carlo Simulations.

As seen in figure 4 the results from the time of flight measurements and the Monte Carlo simulations agree rather well. This indicates that the path the photons take through the porous tissue is simulated

rather well in the Monte Carlo model that was used.

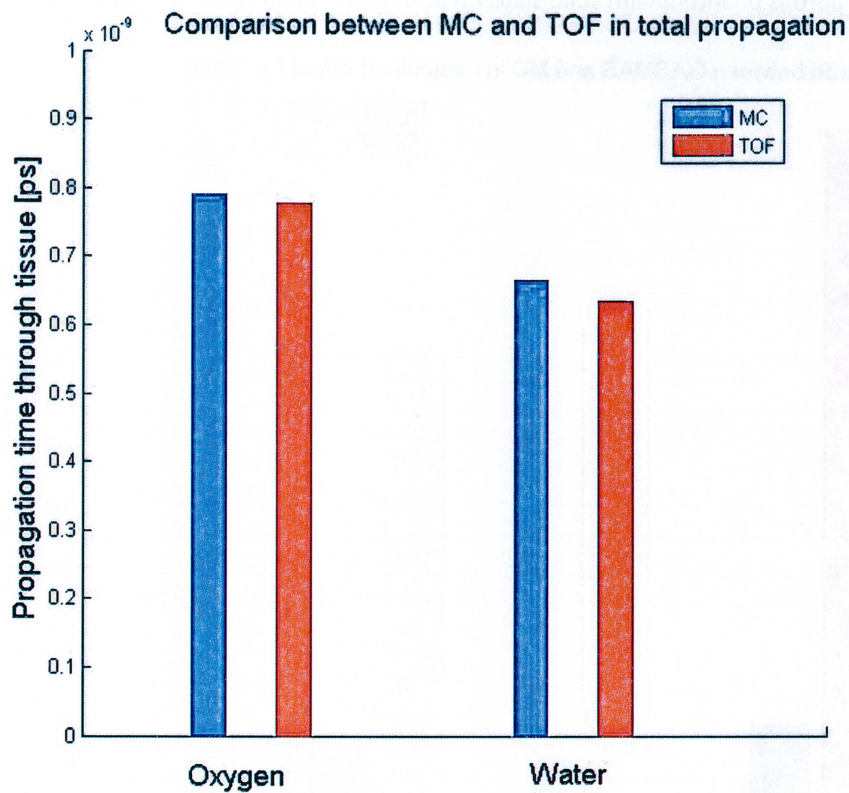


Figure 4 - Comparison of flight times between Monte Carlo simulations and Time of Flight measurements

Transmitted effect

How well light can penetrate a porous tissue compared to a solid one was investigated using the GASMAS system. When measuring with the GASMAS system it is not only possible to measure gas absorption in the media but also the transmitted power was transmitted through the sample. This gives an indication of how hard it is to penetrate the sample and thus give an indication if sufficient light through can be obtained to be able to measure gas concentration. The power was measured at multiple points for all three samples both at 760 nm and at 935 nm.

Also Monte Carlo simulations were made, to see how well the model corresponds with the tissue phantom. Results for the porous phantom with solid slabs on both sides can be seen in Figure 5.

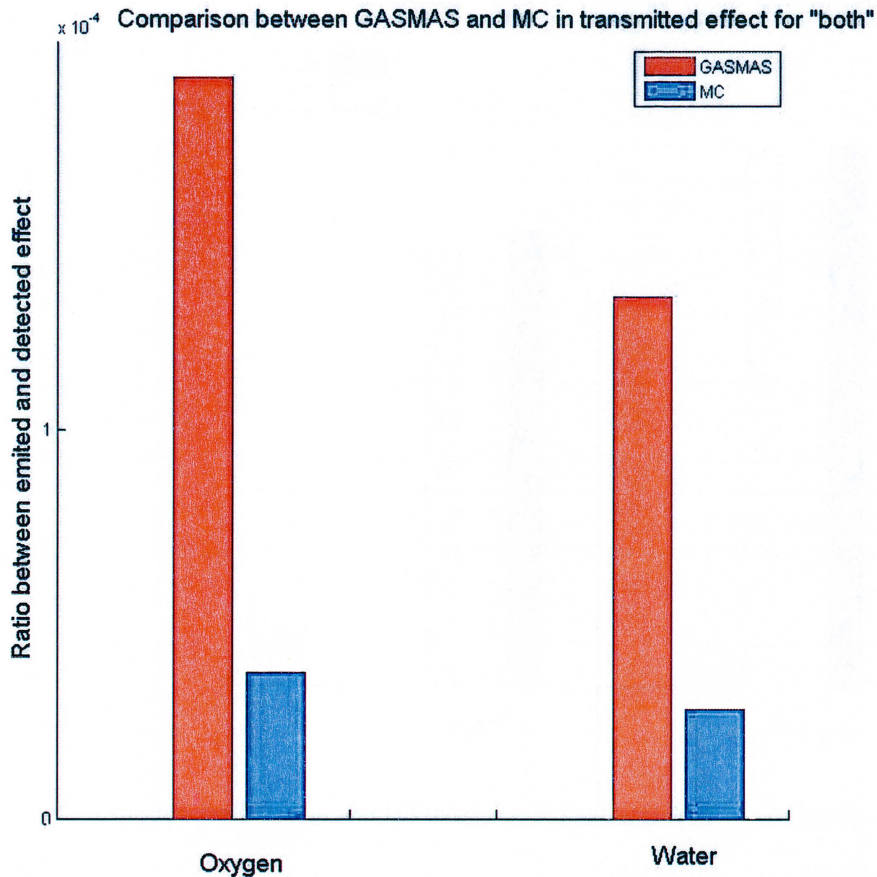


Figure 5 - Ratio of transmitted power - comparison between GASMAS and Monte Carlo

A pore size estimated from the average pore size in the tissue phantom was used. Also the absorption and reduced scattering coefficients used were extracted from the tissue phantom using the Time-of-Flight method described above.

It is quite evident that the Monte Carlo model underestimates the amount of light that is transmitted through the phantom for both the 935 nm and the 760 nm wavelengths. The model however is a rough estimate of the real porous tissue. It has evenly distributed, same size equidistant pores that are perfectly spherical whereas the phantom has a wide variety of pore sizes, also the distribution of the pores are highly irregular.

The transmitted effect through the 24 mm porous slab and the solid slab were measured and the ratio between these two was calculated for both 760 nm and 935 nm. They were found to be 88% and 50% respectively. That means the 935 nm laser is affected more by the porosity compared to the 760 nm

one. This corresponds with the Monte Carlo simulations where the 760 nm laser has only half as much of its intensity penetrating the phantom compared to the 935 nm one. In Figure 6 it can be seen that the oxygen laser is much less affected by the porosity than the water laser. The measurement on the porous phantom also gives this result; even though the water laser is transmitted more than the oxygen laser through solid tissue - in the porous phantom the water laser is transmitted less than the oxygen laser.

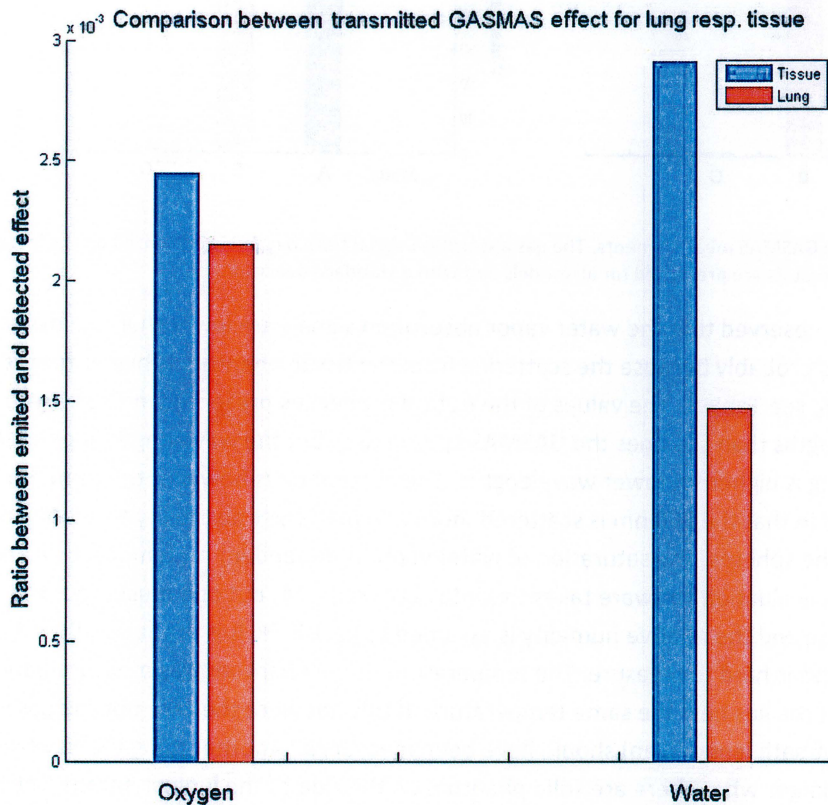


Figure 6 - Comparison between transmitted effect between GASMAS and Monte Carlo simulations for full phantom.

There is no apparent reason for this; as we only found small differences between the two wavelengths regarding absorption and scattering coefficients and flight time. Also no difference in paths taken can be observed, they travel similar fractions of the time in gas.

Propagation through gas spheres

To study how much the propagated light spends within the gas spheres both GASMAS and MC-simulations have been preformed. The GASMAS measurements were done on all three models; i.e. lung phantom with solid phantoms, only lung phantom and a 24 mm thick solid phantom. A gas absorption signal was not to be expected from the solid phantom but it worked as a reference. The MC-simulation is done for model A, two pieces of solid phantom with the lung phantom between. A deeper description of the MC-model is done in the "Monte Carlo simulation" chapter. The results from the GASMAS measurements are presented in Figure 7.

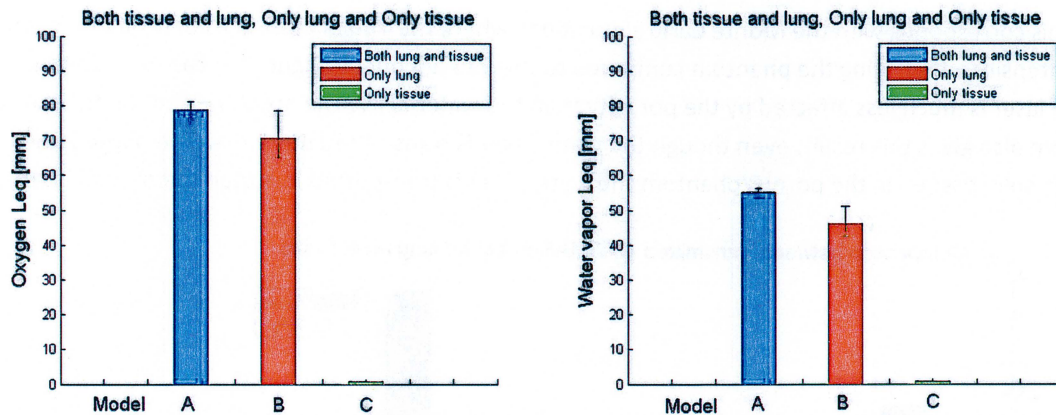


Figure 7. The results from the GASMAS measurements. The gas absorption signal from oxygen is presented on the left and water vapor to the right. The results are presented for all models and with a standard deviation.

From these results it can be observed that the water vapor absorption signals are lower than the oxygen absorption signals. This is probably because the scattering from the tissue phantom is higher for the 760 nm light than the 935 nm; see Table 1. The values of the optical properties presented in Table 1 are for slightly different wavelengths than the ones the GASMAS system uses but the wavelength dependence is the same, the scattering is higher for lower wavelengths. The absorption is however the same for both wavelengths. This results in that the 760 nm is scattered more and has larger possibility to propagate longer total distance in the spheres. The saturation of water vapor is dependent on temperature and relative humidity but the evaluation software takes this into account [4,14] but one must input the temperature in the sphere and the relative humidity is assumed to be 100 %. It is probably 100 % but the temperature of the gas is hard to measure. The temperature of the phantom was measured and then it was assumed that the gas held the same temperature. If this not were the case but the gas were colder a larger equivalent path length (Leq) should have been measured. Another thing that is observed is that the absorption is larger when there are solid phantom on the side of the lung phantom. This is easier to explain because the solid phantom works as a buffer region for the light were it can be scattered back if it leaves the lung phantom. If the light leaves the lung phantom when only measuring on the lung phantom the light is either detected or vanishes away. They results from the comparison between the results from the GASMAS technique and the MC-simulation are presented in Figure 8.

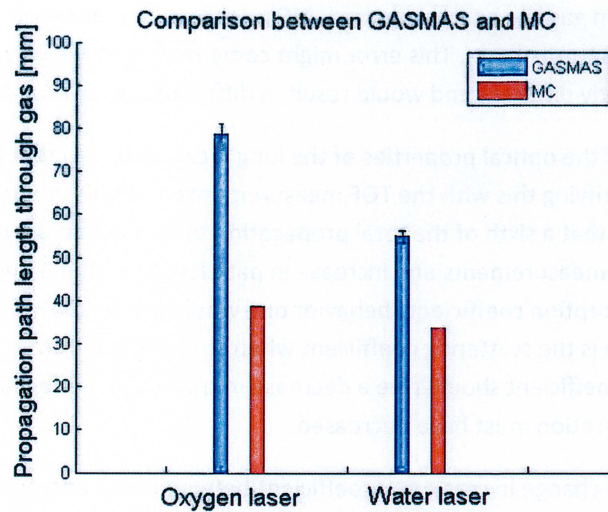


Figure 8. The comparison between the results from the GASMAS measurements and the MC-simulation on model A.

It can be observed that the GASMAS signals are larger than the MC-simulation values but still of the same magnitude. The model in the MC-simulation is a simplification of the lung phantom and do not take into consideration of e.g. small spheres that scatters the light. The porosity measurement were done without take in consideration that some of the water might flow inside the lung phantom when measuring the volume with Archimedes principle. Surface tension in this measurement might also have changed the measured volume. This would have given a larger porosity that would be transferred to the MC-simulation model.

When comparing the GASMAS measurements with the initial GASMAS measurements on a boar lung it is observed that the signals from the boar lung are more than twice as high. However, in these measurements on the lung phantom the properties of it is an abdominal muscle and that might not correlate very well with real lung tissue. The lung might also be filled with many smaller spheres that increases the scattering and decreases the absorption with ultimately results in higher path lengths through gas. But the advantage with the lung phantom is that the absorption and scattering can be altered but naturally it is hard to predict how the introduction of small spheres exactly changes the optical properties when the size and amount of spheres are hard to control. The refractive index of the phantom may not be the same as tissue and that would also affect the scattering.

Discussion

When comparing the different method we observe that MC and TOF correlate very well when calculating the total flight time through model A, tissue plus lung. The optical properties inserted in the MC are from the TOF measurements of the solid phantom. This removed the uncertainties of the optical properties and focuses on the comparison of how well the model geometry simulates the actual phantom concerning the flight time. The results in this comparison are in good agreement with each other. When comparing GASMAS and MC the results are not that well in agreement. The transmitted

effect and the path length in gas has been compared. MC gives lower results than GASMAS both in transmitted effect and path through gas. This error might come from that the wavelengths used in the different methods are slightly different and would result in different optical properties.

From the measurements of the optical properties of the lung it can be observed that the absorption coefficient is halved but verifying this with the TOF measurements and MC-simulations is hard. Because the MC-simulation tells us that a sixth of the total propagation time is within the gas spheres and if this is implemented to the TOF measurements and increase in path length within tissue of two thirds is obtained. To verify the absorption coefficients behavior one would like to know the total absorption but mixed with the attenuation is the scattering coefficient when studying the transmitted effect. However, the increase in scattering coefficient should give a decrease in transmitted effect larger than the one obtained and thus the absorption must have decreased.

We have observed that the change in scattering coefficient between solid and porous phantom is the same for both 935 nm and 760 nm. The absorption however decreases more for the 935 nm laser compared to the 760 nm one. From the time of flight measurements we see that the flight path length increases more for the water laser than the oxygen one. These results should together reduce the water laser a bit more than the oxygen laser but from the transmitted effect measurements where the 935 nm laser is reduced far more than expected in the porous case than the 760 nm laser in the GASMAS measurements.

Summary

From the performed measurements it has been shown that the small gas spheres increase the scattering but at the same time reduce the absorption. The light takes shortcuts through the spheres but it is also scattered by them.

Flight time was measured through porous and solid tissue phantoms. The flight time was found to be approximately double for the porous one. From this it can be concluded that the increased scattering from the pores greatly outweighs the possibility for the photons to take shortcuts through the pores. Also measurements on the full tissue phantom were compared with Monte Carlo simulations of the same and they were found to agree well.

Transmitted effect was measured on three different phantoms. Comparisons between solid and porous ones show that the water laser is more dampened than the oxygen laser in a porous material compared to a solid material. The Monte Carlo model gives substantially lower transmission rates than the actual measured ones and its validity should be investigated further.

GASMAS measurements and MC-simulations show quite similar results but in the MC-simulation the geometry has been simplified and effects as scattering on small gas spheres are not taken into consideration.

The lung phantom might be a good substitute to a real lung but then the optical properties of a lung must be measured and further effort must be made to develop a method to introduce the gas spheres in a controlled so their effects to the optical properties can be determined.

Acknowledgements

Erik Alerstam, Atomic physics division Lund University, for help with the Monte Carlo simulations and the TOF measurements

Can Xu, Atomic physics division Lund University, for providing equipment for construction of the tissue phantoms.

Vattenhallen, for providing a much needed magnet for the stirring of the phantom as to produce the tissue phantom foam.

References

1. The Express Group. Incidence of and risk factors for neonatal morbidity after active prenatal care: Extremely preterm infants study in sweden. *Acta Paediatrica*, 2010.
2. M Blennow, U Ewald, T Fritz, P-A Holmgren, A Jeppsson, E Lindberg, A Lundqvist, S N Lindeberg, E Olhager, I Ostlund, M Simic, G Sjoers, L Stigson, V Fellman, L Hellstrom-Westas, M Norman, M Westgren, G Holmstrom, R Laurini, K Stjernqvist, K Kallen, H Lagercrantz, K Marsal, F Serenius, M Wennergren, T Nilstun, P O Olausson, B Stromberg, and Express Group. One-year survival of extremely preterm infants after active perinatal care in sweden. *Journal of the American Medical Association*, 301(21):2225-33, 2009.
3. M B van Veenendaal, M Miedema, F H C de Jongh, J H van der Lee, I Frerichs, and A H van Kaam. Effect of closed endotracheal suction in highfrequency ventilated premature infants measured with electrical impedance tomography. *Intensive Care Medicine*, 35(12):2130-34, 2009.
4. A Bruzelius. Measurements on free gas in human tissue with diode laser spectroscopy, *Master Thesis Atomic physics division Lund University*. (2010)
5. B W Pogue and M S Patterson. Review of tissue simulating phantoms for optical spectroscopy, imaging and dosimetry. *Journal of Biomedical Optics*, 11(4), 2006.
6. C R Simpson, M Kohl, M Essenpreis, and M Cope. Near-infrared optical properties of ex vivo human skin and subcutaneous tissues measured using the monte carlo inversion technique. *Physics in Medicine and Biology*, 43(9):2465-2478, 1998.
7. A J Welch and M J C van Gemert. Optical-Thermal response of Laser- irradiated tissue. *Plenum press*, 1995.
8. S A Prahl. Light transport in tissue. *PhD Thesis University of Texas at Austin*, 1988.

